

Optical Properties of Two Dimensional Semiconductors and Carbon Hybrid Structures

Vorgelegt von Diplom-Physiker

Gunnar Berghäuser

aus Marburg

von der Fakultät II - Mathematik und Naturwissenschaften
der Technischen Universität Berlin

zur Erlangung des akademischen Grades

Doktor der Naturwissenschaften

– Dr. rer. nat. –

genehmigte Dissertation

Promotionsausschuss

Vorsitzende : Prof. Dr. rer. nat. Janina Maultzsch, TU Berlin

1. Gutachter : Prof. Dr. rer. nat. Andreas Knorr, TU Berlin

2. Gutachter : Prof. Dr. rer. nat. Ermin Malić, Chalmers University of Technology

Tag der wissenschaftlichen Aussprache: 06.03.2015

Berlin 2015

CONTENTS

1	Introduction	11
2	Theoretical Model; From Microscopic Quantities to Macroscopic Observables	13
2.1	Cluster Expansion	14
I	Functionalized Low Dimensional Carbon-Nano Structures	17
3	Introduction	19
4	Theoretical Approach for Molecule-Substrate Coupling (MSC)	23
4.1	Impact of Substrate-Molecule Coupling on Optical Absorption	27
4.2	Impact on One-Dimensional Nanoribbons	29
4.3	From 1-dim Nanoribbon to 2-dim Graphene Substrates	34
4.4	Molecular Distributions: The Impact of Molecule Orientation and Molecular Coverage	37
4.5	Conclusion	38
II	Two Dimensional Semiconductors	39
5	Introduction	41
6	Transition Metal Dichalcogenides Hamiltonian	43
6.1	Tight-Binding Approach	43
6.1.1	Bandstructure and TB-Coefficients of the K-valleys	45
6.1.2	Optical Matrix Element	49
6.1.3	Coulomb Matrix Element	51
6.1.4	System Hamiltonian	54

CONTENTS

6.2	TMD Bloch Equations	55
7	Linear Optics	57
7.1	Analytical Approach to Excitonic properties of TMDs	57
7.1.1	TMD-Bloch Equation in the Linear Regime	58
7.1.2	Absorption Spectrum of MoS ₂	59
7.1.3	Effect of Screening on excitonic binding energies	62
7.1.4	Higher Excitonic Transition	64
7.1.5	Conclusions	65
7.2	Radiative Coupling	66
8	Coulomb-Induced Intervalley Coupling	71
8.1	Absorption Coefficient of Valley Coupled Two Dimensional Semiconductors	75
8.2	Detuned Valleys and the Transition to TMDs including Spin Orbit coupling	76
8.3	Coulomb Induced Intervalley Coupling in non-linear Optics	78
8.4	Microscopic Approach	78
8.4.1	Electron-Hole-Picture	78
8.4.2	Excitonic Basis	80
8.5	Valley coupling in TMDs	85
8.5.1	Differential Transmission Spectroscopy	85
8.5.2	Differential Transmission Spectroscopy in Valley Coupled WS ₂	86
9	Discussion	91
	Appendices	93
A	Lindhard Screening	95
B	TMD Parameters	97
C	Radiative Coupling; homogeneous and inhomogeneous linewidth	99

ABSTRACT

Research on novel materials has long been a driving force behind technological progress. In this thesis the optical properties of transition metal dichalcogenides (TMDs) and carbon-hybrid nano structures are investigated within a microscopic theory based on the density matrix formalism.

Part 1: In the field of hybrid nanostructures researchers aim to design novel materials with desired characteristics. The increasing number of publications in this interdisciplinary area combining physics, chemistry, material science, and biology manifests the relevance and the general interest in a better understanding of these structures. To exploit the full potential of this field, a thorough microscopic understanding of the molecule-substrate coupling is of key importance. I present a microscopic approach focusing on optical properties of carbon-based hybrid materials. Consisting of a single layer of atoms, carbon nanostructures are very sensitive to changes in their environment. Therefore, the functionalization with external molecules enables the control and optimization of their properties. In particular, photoactive molecules are promising for engineering optical switches on the molecular level that can be incorporated in solid-state technologies. I have investigated the fundamental coupling mechanism between electrons in graphene-based substrate and an external molecular dipole field. My calculations reveal considerable changes in the absorption spectrum of the substrate. It will be shown that the predicted peak splitting and spectral shifts strongly depend on the electronic bandstructure of the substrate. Furthermore, I shed light on the crucial role of the substrate dimension by investigating one-dimensional nanoribbons with increasing width up to two-dimensional graphene. The investigated coupling mechanism, which is driven by molecular dipole fields, presents a general situation and appears in a large class of hybrid nanostructures. Therefore, my conclusions and the presented many-particle Bloch equations reach further than the presented exemplary case and can be used in order to understand a broad class of hybrid materials.

Part 2: Transition metal dichalcogenides (TMDs) represent a new class of atomically thin two-dimensional materials that exhibit (similarly to graphene) extraordinary electronic, optical, mechanical, and chemical properties. In addition, the inversion symmetry is broken giving rise to a band gap opening at the K and K' points making them promising materials for optoelectronic devices. Another fundamentally interesting and technologically highly relevant feature of TMDs is the possibility to selectively excite the K and K' valley via right or left circularly polarized light, respectively. As a result, the valley can be exploited as a new degree of freedom in addition to charge and spin of electrons suggesting TMD-based valleytronics devices. The underlying microscopic processes governing the valley polarization and intervalley coupling

CONTENTS

are still not well understood. I present a microscopic study on the excitonic and optical properties of TMDs. I will show our tight binding approach for the two dimensional semiconductors which leads to the TMD specific excitonic binding energies and eigenfunctions. Furthermore, it will be shown that the TMD properties lead to a extraordinary strong radiative coupling and calculate the radiative life time of TMDs.

CONTENTS

ACKNOWLEDGEMENT

I humbly thank every one who has supported me (both scientifically and/or personally by making the last years good years) in the years during the creation of this thesis. I thank:

- Ermin Malic for agreeing to evaluate my thesis and even more for his support and advice in life and science.
- Andreas Knorr for agreeing to evaluate and for his great scientific advice and support.
- Janina Maultzsch for being the chair of my thesis committee.
- Rudolph Bratschitsch and his group for successful and very pleasant cooperation.
- The hole group of Andreas Knorr, which has welcomed me from the first moment. Here, I want to mention the “Mensa” group with whom the lunch break was fun, relaxing and full of good discussions from which some broad inspired new ideas also related to my work.

I thank Florian Wendler for being a great room mate. We where both born into the group on the same day and he always had an ear open to discuss physics and other important and relevant topics. I also thank Eike Verdenhalfen, Hannah Funk and Torben Winzer for being great room mates who where also always available for helpful discussions.

Than there is the IT team of the group, most of all Mario and Marten who helped me out in it-related questions and where often patient whit me and my limited knowledge of the queuing system.

- I thank my Family and Friends for their support in all aspects of life.
- I also to thank the team of the cafeteria and “Mensa”. Especially the “Aktionsstand” has often lightened up the lunch brake whit nicely prepared food. I want to mention the zander filet which I always looked forward to on the menu. Clearly, this work would have

CONTENTS

been harder to accomplish without the help of the employees of the cafeteria, who supported me with an infinite supply of sugar and caffeine.

- For financial support I thank the Einstein Foundation of Berlin.

“Nothing is esteemed a miracle, if it ever happen in the common course of nature. It is no miracle that a man, seemingly in good health, should die on a sudden: because such a kind of death, though more unusual than any other, has yet been frequently observed to happen. But it is a miracle, that a dead man should come to life; because that has never been observed in any age or country.”

David Hume

CONTENTS

PUBLICATIONS

This work is partially published or submitted for publication in the following articles or manuscripts:

Publications in Peer-Review Journals

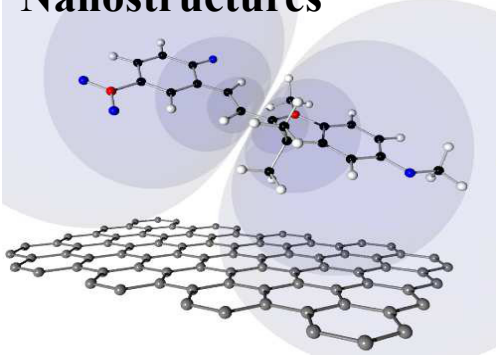
- G. Berghäuser and E. Malic, *Molecule-substrate coupling in functionalized graphene*, Carbon 69, 536 (2014).
- G. Berghäuser and Ermin Malic, *Analytical approach to excitonic properties of MoS₂*, Phys. Rev. B 89, 125309 (2014)
- G. Berghäuser and Ermin Malic, *Optical properties of functionalized graphene*, Phys. Status Solidi (b) 250, 2678 (2013)

Submitted manuscripts

- G. Berghäuser, A. Knorr, E. Malic, *Coulomb induced intervalley coupling in transition metal dichalcogenides*, submitted to Phys. Rev. Lett.
- R. Schmidt, G. Berghäuser, E. Malic, A. Knorr, R. Schneider, P. Tonndorf, S. Michaelis de Vasconcellos and R. Bratschitsch, *Ultrafast Coulomb intervalley coupling in atomically thin WS₂*, submitted to Nature Physics
- Galan Moody, Chandriker Kavir Dass, Kai Hao, Chang-Hsiao Chen, Lain-Jong Li, Akshay Singh, Kha Tran, Genevieve Clark, Xiaodong Xu, Gunnar Berghäuser, Ermin Malic, Andreas Knorr, and Xiaoqin Li, *Intrinsic Homogeneous Linewidth and Broadening Mechanisms of Excitons in Monolayer Transition Metal Dichalcogenides*, Submitted to Nature.

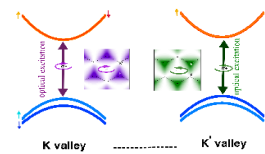
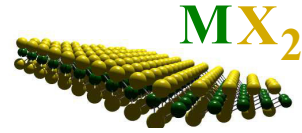
CONTENTS

Carbon-Hybrid Nanostructures



&

Transition Metal Dichalcogenides



CHAPTER 1

INTRODUCTION

From the stone age to nowadays age of silicon, technological progress has often been driven by the exploration of material properties. The aim of this thesis is to understand and describe many-body processes in new classes of materials, transition metal dichalcogenides (TMDs) and carbon-hybrid nanostructures. In recent years the study of carbon nanostructures has become a major field of solid state research [79, 26, 14, 10, 38, 58]. It has gained a tremendous boost since the discovery of graphene in 2004 [70] and it has been growing ever since. Graphene's electronic properties are remarkable, in particular it is quasi-resistant to impurities and has a high carrier mobility [26]. Graphene is considered as one of the most promising future materials with potential applications in spintronic devices, solar cells, batteries, touch screens, sensors and many more [10, 2, 71, 58]. This was underlined by the Nobel Prize Geim and Novoselov received in 2010 for their remarkable discovery.

However, the experimental and theoretical investigation of graphene has made great progress

since its discovery. Although many questions are still to be answered, many concepts have successfully been applied and many properties of the two-dimensional lattice have been understood, also on a microscopic level [98, 100, 99, 66]. Graphene research is now in a state where it has to deal to more complex questions and situations closer to a potential application. In this theses I will show my analyses of two new research fields induced by graphene research.

In current graphene research, one of the major challenges is to alter and modify the electronic bandstructure such that its properties can be exploited. This can be done by modifying the surrounding conditions of graphene. One example is graphene in electric or magnetic fields [97, 67, 95, 96]. Another is to stack graphene with other different layered materials. Here I discuss, the functionalization of graphene with photoactive molecules, which is the topic of the second part of this thesis. I present a theory which shows how optical properties of graphene can be manipulated by functionalization.

Apart from graphene, Gaim and Novoselov discovered a broad class of other van der Waals bounded ultrathin-layered nanomaterials, the biggest group of which are the transition metal dichalcogenides (TMDs). The quasi-two-dimensional semiconductors consist of one (from 16 different) transition metals (M) covalently bound to chalcogenes (MX_2 , $X \in \text{S, Se, Te}$). In contrast to graphene, the inversion symmetry is broken giving rise to a band gap opening at the K point. Furthermore, they are characterized by a strong spin-orbit interaction that in combination with the circular dichroism enables selective valley and spin polarization suggesting a variety of optoelectronic and spin-valleytronic applications. In the second part the excitonic and optical properties of two-dimensional semiconductors are discussed.

CHAPTER 2

THEORETICAL MODEL; FROM MICROSCOPIC QUANTITIES TO MACROSCOPIC OBSERVABLES

The applied theory uses the density matrix approach, which allows a consistent treatment of many-body processes from the microscopic point of view up to macroscopic observables. This theory has often been applied successfully within the field of solidstate physics, from from three-dimensional semiconductors in the 60's covering quantum wells and quantum dots since the 80's up to low dimensional carbon materials like fullerenes and nanotubes since the 90's [23, 24, 33, 58, 43, 64, 63]. Even now, the application of the theory on new situation leads to both fundamental new concepts and the understanding of fundamental many-body physics. Both are important to understand intrinsic electronic and optical properties of a solid. New insights allow the exploration of material properties efficiently in future technology, e.g. electronic devices like the quantum computer or spin- and valleytronics.

The density matrix formalism uses the following connection from macroscopic to microscopic quantities. The absorption $\alpha(\omega)$ is proportional to the systems linear response function $\omega\Im[\chi(\omega)]$ which it self is determined by the microscopic transitions $\rho_{ij} = a_j^\dagger a_i$. Where a_j^\dagger creates and a_i annihilates a particle in state j or i . The important assumptions of this method are shown in this part of the thesis.

The coupling of a solid to a classical electromagnetic field is described by the inhomogeneous solution of Maxwell's wave equation. In this section we will present Maxwell's wave equation in the $\mathbf{A} \cdot \mathbf{p}$ picture, connecting a classical light field with the microscopic quantities. In this work we focus on quasi two dimensional materials, with an effective thickness

in the range of a few . Since a typical wave length is in the order of a few hundred nm, the ultra thin material acts as a δ -function. If we further assume that, the field is polarized in l -direction and that it propagates perpendicular to the nanostructure (in \mathbf{r}_\perp), so that we can write $\langle \mathbf{A}(\mathbf{r}) \rangle = \delta_{r_\perp} \langle |A(r_\perp)| \rangle \mathbf{e}_l$, we can formulate the wave equation as follows [18],

$$\left(\frac{\partial^2}{\partial z^2} - \frac{n^2}{c^2} \frac{\partial^2}{\partial t^2} \right) \langle A(z) \rangle = -\mu_0 \underbrace{\frac{\partial}{\partial t} \mathbf{P} \cdot \mathbf{e}_l}_{J_l}. \quad (2.1)$$

Here n is the refractive index. For the absorption, reflection and transmission of two dimensional materials within in a dielectric environment see appendix C. The optically induced current J_l is the current in direction of the incident light. From a microscopic point of view this quantity can be described via,

$$P_l = \frac{1}{S} \sum_{\mathbf{k}} M_l^{ij} p_{\mathbf{k}}^{ij}. \quad (2.2)$$

This equation in combination with the wave equation connects microscopic quantities and macroscopic observables. In order to evaluate the coupling to of the carriers to an external perturbation the source terms in Eq.2.1 have to be evaluated. The microscopic quantity, hence the density matrix, time evolution can be calculated using the Heisenberg's equation of motion. This will be discussed in the next section.

2.1 CLUSTER EXPANSION

Although computers are a lot faster than in the early days of numerical research it is not possible to consider all correlations between all particles in the computations. The number of interacting particles in a solid is way too large. Including two particle correlations the capacity of modern computers has already reached their limit. Hence, good approximations are needed to find models which are solvable and give a good descriptions of reality. In this section we will present a method which allows to reduce the correlations in a system to the dominant terms.

To evaluate Maxwell's wave equation (2.1), we need to determine the source terms. The source terms are given by single particle expectation values $\langle a_i^\dagger a_j \rangle$. The different density matrix-elements are the carrier distribution

$$f_{\mathbf{k}}^i = \langle a_i^\dagger a_i \rangle, \quad (2.3)$$

and the coherent microscopic transition amplitude between state i and j

$$p_{ij} = \langle a_i^\dagger a_j \rangle. \quad (2.4)$$

The quantum dynamics of the expectation values can be found using the Heisenberg equation of motion which for any operator O states:

$$i\hbar \frac{d\langle O \rangle}{dt} = \langle [O, H]_- \rangle \quad (2.5)$$

Here H is the system Hamiltonian, which has to be chosen such that it captures the most important aspects of the system. If the system Hamiltonian includes many-body interactions, the Heisenberg equation of motion leads, for the single particle expectation values Eq. (2.3) - (2.4), to an unclosed set of equations. N -particle correlations couple over many body interactions to $(N+1)$ -particle correlations, this leads to an infinite hierarchy of equations,

$$i\hbar \frac{d\langle N \rangle}{dt} = T[\langle N \rangle] + V[\langle N + 1 \rangle] \quad (2.6)$$

where T and V are known functionals. This infinite set of equation is commonly known as the hierarchy problem. A good approximation method is the cluster expansion, where one truncates the hierarchy on a chosen level and expresses the N -particle correlations in terms of lower order correlations.

$$\begin{aligned} \langle 1 \rangle &= \langle 1 \rangle_S \\ \langle 2 \rangle &= \langle 2 \rangle_S + \Delta \langle 2 \rangle \\ \langle 3 \rangle &= \langle 3 \rangle_S + \langle 1 \rangle_S \Delta \langle 2 \rangle + \Delta \langle 3 \rangle \\ &\vdots \\ \langle N \rangle &= \langle N \rangle_S + \langle N - 2 \rangle_S \Delta \langle 2 \rangle + \langle N - 4 \rangle_S \Delta \langle 2 \rangle \Delta \langle 2 \rangle \\ &\quad + \dots + \langle N - 3 \rangle \Delta \langle 3 \rangle + \dots + \Delta \langle N \rangle \end{aligned}$$

Here the N -particle correlations in singlet cluster expansion read as

$$\langle N \rangle_S = \sum_{\pi} (-1)^{\pi} \prod_{i=1}^N \langle a_{\mathbf{k}_i}^\dagger a_{\mathbf{p}_{\pi[i]}} \rangle, \quad (2.7)$$

where $\mathbf{k}_i = (\lambda_i, \mathbf{k}_i)$, $\mathbf{p}_i = (\nu_i, \mathbf{p}_i)$, and π is a permutation of the \mathbf{k}_i with sign $(-1)^{\pi}$. To motivate this approach, one can argue that the likeliness of many body interactions decays

with their order. Hence one reduces the problem to the dominant terms. The cluster gives an intuitive solution, and it could and can successfully be applied in quantum chemistry [32], in semiconductors [41] [44, 33, 40, 41] as well as in quantum optics [44, 42, 43].

In this theses we will truncate the hierarchy problem on the singlet level, with the equation of motion as

$$i\hbar \frac{d\langle 1 \rangle}{dt} = T_1 [\langle 1 \rangle] + V_2 [\langle 2 \rangle_S] + V_2 [\Delta \langle 2 \rangle] \quad (2.8)$$

we replace $V_2 [\Delta \langle 2 \rangle]$ by a phenomenological scattering constant as it is discussed in detail in [44]. Additionally we can in the case of the transition metal dichalcogenides assume that the layer is perfect and hence is spatially homogeneous and we find singlets only diagonal in \mathbf{k} ,

$$\langle a_{i,\mathbf{k}}^\dagger a_{j,\mathbf{k}'} \rangle = \delta_{\mathbf{k},\mathbf{k}'} \langle a_{i,\mathbf{k}}^\dagger a_{j',\mathbf{k}} \rangle. \quad (2.9)$$

Note that this is not true for the here also discussed carbon-hybrid systems where the spatial homogeneity is not given due to the molecular coverage which induces a spatial inhomogeneity. For this thesis we truncate the hierarchy problem on the Hartree-Fock level to solve the Heisenberg's equation of motion. In this section we were able to reduce the hierarchy problem to a closed set of equations including all the physical quantities relevant for this theses. The particular Hamiltonians and system quantities are derived in the following sections where than the here showed method is applied in order to evaluate the time evolution of the microscopic quantities, the density matrix.

Part I

Functionalized Low Dimensional Carbon-Nano Structures

CHAPTER 3

INTRODUCTION

The study of carbon-based hybrid nanostructures is an emerging field of current research. In particular, photo-active molecules have been shown to considerably influence optical properties of carbon nanotubes suggesting realization of molecular switches. In this part the focus lies on the nature of the molecule-substrate coupling within a variety of carbon-based hybrid nanostructures including one-dimensional nanoribbons of different widths and the two-dimensional graphene. The microscopic approach based on density-matrix formalism predicts a splitting of the pristine spectral resonances into multiple peaks combined with a considerable spectral shift. Both effects are strongly influenced by the electronic bandstructure of the substrate. Furthermore, I investigate the impact of the dimensionality on the molecule-substrate coupling by increasing the width of nanoribbons from the very narrow up to graphene. The calculations reveal a clear increase of the optical absorption of graphene in the vicinity of the Dirac-point and a peak broadening at the saddle-point due to the appearance of a high-energy shoulder. My results give new insights into the molecule-graphene coupling and can guide future experiments towards the realization of tailored hybrid materials with desired optical properties.

In this part, I present a study on carbon-based hybrid nanostructures, in particular spiropyran (SP)- and merocyanine (MC)-functionalized armchair graphene nanoribbons (AGNRs) and graphene. Nanoribbons are thin slices of graphene and can be considered as graphene's one-dimensional equivalent [22]. Their advantage lies in the variable band gap, which can be controlled by the ribbon's width [31].

Both, AGNR and graphene as mono-layers of carbon atoms, are very sensitive to changes in the surrounding material. This opens the possibility to manipulate their properties by the control of the surrounding media and motivates the functionalization approach [90, 34, 29]. The long-term aim is the design of new materials with desirable characteristics [1, 86, 107, 11]. This idea has drawn researchers' attention in recent years for many different reasons [45, 21, 102, 80]. In

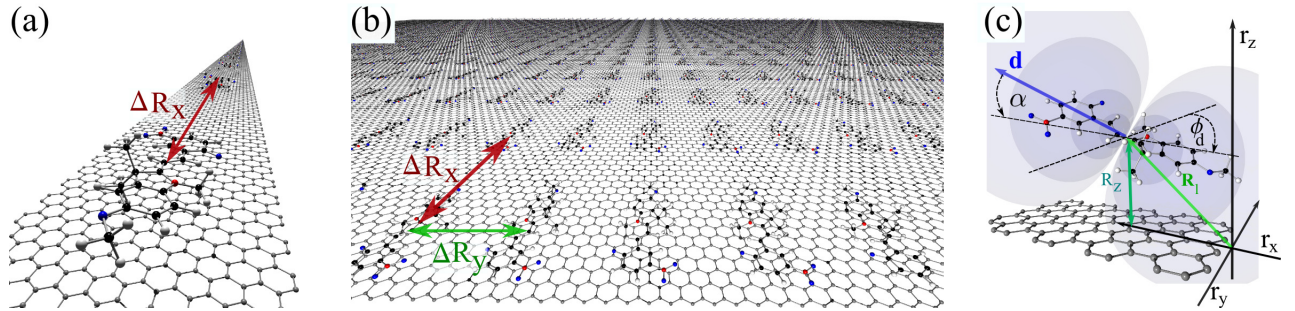


Figure 3.1: Illustration of the mercyanine molecules adsorbed on a) a nanoribbon and b) graphene. The molecules are periodically distributed on the corresponding substrate. In the case of the one-dimensional nanoribbon, there is one row of molecules with the molecule-molecule distance ΔR_x , while in the case of graphene the molecules form a periodic *lattice* with the constants ΔR_x and ΔR_y . In part c), a close up of a randomly orientated mercyanine molecule on a hexagonal carbon surface is shown. The molecule distance to the substrate is given by $|R_z| \approx 0.34\text{nm}$ corresponding to the Van der Waals diameter of carbon. The dipole vector $\mathbf{d} = d(\cos(\phi_d)\cos(\alpha), \sin(\phi_d)\cos(\alpha), \sin(\alpha))$ is determined by the molecular dipole moment d , the angles α and ϕ_d expressing the dipole orientation perpendicular (z -axis) and parallel (xy -plane) to the substrate, respectively.

graphene, the conduction and valence band intersect at the Dirac-points. This makes graphene unsuited for semiconductor devices, where a defined band gap is needed. That is why a band gap opening without losing properties, such as the high carrier mobility, is one of the main goals of the current research. Functionalization with molecules is believed to be a potential strategy to overcome this problem [20, 3]. Furthermore, graphene functionalized with bio-molecules (e.g. proteins, DNA) opens a way for bio-applications of graphene and graphene-based materials [94], e.g. it could be shown that graphene can be used for DNA analysis [25]. Recently, electronic transport and optical properties of carbon nanostructures functionalized with photo-active molecules have been studied experimentally and theoretically [29, 86, 9, 28, 81, 65, 61, 60].

The focus of this work lies on a fundamental understanding of the molecule-substrate coupling in hybrid nanostructures consisting of a carbon-based substrate and an adsorbed photo-active molecule inducing a reversibly switchable dipole field, cf. 3.1. Within a microscopic approach based on the density-matrix formalism [33, 44], I address the question of how an external dipole field influences the carriers of the substrate.

In analogy to the Stark effect on atoms in an electro-magnetic field [33], my calculations reveal that the presence of an molecule-induced dipole field leads to a splitting and a spectral shift of resonances in the absorption spectra of the substrate. However, while the Stark effect is based on the removal of the degeneracy of the angular momentum state, the observed splitting in the investigated hybrid nanostructures is induced by indirect optical transitions. Due to a

dipole-induced momentum transfer, the carriers can reach states energetically below or above the excitation frequency. I will show that the electronic bandstructure of the substrate plays a crucial role. Furthermore, the dimensionality has a significant impact on the nature of the coupling. To investigate this, carbon nanoribbons of increasing width up to a two-dimensional graphene sheet have been studied. The calculations predict that the peak splitting and the spectral shift observed in the absorption spectra of nanoribbons vanish to a large extent within the graphene continuum. However, at high-symmetry points, I find significant changes in the absorption spectrum of graphene including a clearly enhanced absorption in the vicinity of the Dirac point and a peak broadening at the saddle-point.

This part of the thesis is structured as follows: After introducing the applied theoretical approach, I show the influence of the adsorbed molecules on the optical absorption of different substrates. First, we discuss the impact of the molecule-substrate coupling on one-dimensional nanoribbons including the study of the importance of their electronic bandstructure. Second, we investigate the transition from one-dimensional to two-dimensional substrates by increasing the width of the nanoribbons up to a graphene sheet. And third, we investigate different molecular distributions and analyse their impact on the absorption spectrum of graphene.

CHAPTER 4

THEORETICAL APPROACH FOR MOLECULE-SUBSTRATE COUPLING (MSC)

In this work, we investigate carbon nanoribbons and graphene functionalized with spiropyran molecules. The substrate is chosen to lie in the xy -plane and in the case of the nanoribbons; we chose the spatial confinement in y -direction. Due to this confinement nanoribbons can be seen as quantized graphene [31]. They can be constructed by cutting the graphene sheet into thin slices or by unwrapping carbon nanotubes [48, 30]. In terms of wave functions, we start with the well-known case of graphene and apply edge boundary conditions [106]. One distinguishes between armchair and zigzag nanoribbons, which are characterized by the corresponding armchair or zigzag edge. In this work, we exemplarily study armchair graphene nanoribbons (AG-NRs). Their width is given by $W = (N_c + 1)\frac{a_0}{2}$, where N_c denotes the number of carbon atoms along the width of the nanoribbon. This gives the constrain for the transversal wave number $k_{\perp} = k_y \rightarrow k_y^m = 2m\pi/a_0(N_c + 1)$ with $m \in N_c$. The graphene bandstructure is sliced into N_c subbands with different curvatures and bandgaps. Depending on whether a k_y^m includes the Dirac point ($k_y^m = \pm 2\pi/(a_0\sqrt{3})$) or not, the nanoribbon is metallic or semiconducting [106]. For growing N_c , the quantization goes over into a quasi-continuum and the ribbon becomes graphene. This allows us to study the transition from one-dimensional nanoribbon to two-dimensional graphene by increasing the width of investigated nanoribbons.

The chosen spiropyran molecules can be reversibly switched into the merocyanine configuration via infrared light inducing a large change in the dipole moment (16 Debye compared to approximately 6 Debye of the spiropyran configuration) [59, 84]. The induced switchable

dipole moment is expected to have a large influence on the optical and electronic properties of the substrate. The molecules are non-covalently bound to the substrate via Van der Waals interaction. As a result, the electronic wave functions remain unchanged to a large extent [59] and we can consider the substrate as located within a static field of the attached molecules.

In order to obtain the absorption spectra of the hybrid nanostructure, we need to calculate the absorption coefficient

$$\alpha(\omega) \propto \omega \text{Im}[\chi(\omega)], \quad (4.1)$$

which is proportional to the optical susceptibility $\chi(\omega)$ and gives the system's linear answer to an optical perturbation described by the vector potential $A(\omega)$ [33]. The susceptibility $\chi(\omega) \propto P(\omega)/(\omega^2 A(\omega))$ is determined by the macroscopic polarization $P(\omega) = \sum_{\mathbf{k}} p_{\mathbf{k}}^{vc}(\omega) M_{\mathbf{k}}^{vc} + cc$. The latter is a sum over all microscopic polarizations $p_{\mathbf{k}}^{vc}(t) = \langle a_{v\mathbf{k}}^\dagger a_{c\mathbf{k}} \rangle(t)$ weighted by the interband carrier-light coupling element $M_{\mathbf{k}}^{vc}$ [27, 62, 66]. The microscopic polarization is a measure for optical transitions between states \mathbf{k} in the valence (v) and the conduction (c) band. To derive the equation of motion for $p_{\mathbf{k}}^{vc}(t)$ within the density matrix formalism, we start with the Hamilton $H = H_0 + H_{c-l} + H_{c-d}$ including the non-interacting carrier contribution $H_0 = \sum_{\mathbf{k}\lambda} \varepsilon_{\mathbf{k}\lambda}^\lambda a_{\mathbf{k}\lambda}^\dagger a_{\mathbf{k}\lambda}$, the carrier-light interaction $H_{c-l} = \frac{i\hbar e_0}{m_0} \sum_{\mathbf{k}, \lambda \neq \lambda'} \mathbf{M}_{\mathbf{k}}^{\lambda\lambda'} \cdot \mathbf{A}(t) a_{\mathbf{k}\lambda}^\dagger a_{\mathbf{k}\lambda'}$, and the molecule-substrate coupling (here, carrier-dipole interaction) $H_{c-d} = \sum_{\lambda\lambda'} \sum_{\mathbf{k}\mathbf{k}'} g_{\mathbf{k}\mathbf{k}'}^{\lambda\lambda'} a_{\mathbf{k}\lambda}^\dagger a_{\mathbf{k}'\lambda'}$ with the corresponding matrix element $g_{\mathbf{k}\mathbf{k}'}^{\lambda\lambda'}$ defined below. In this first study, we do not consider the effects of the Coulomb interaction, since we are interested in understanding the qualitative nature of the molecule-substrate coupling (MSC) in carbon-based hybrid nanostructures. Though Coulomb interaction is known to considerably influence the spectrum of AGNRs and graphene [75, 103, 66], it was shown to only have a quantitative impact on the molecule-substrate coupling in the investigated structures [59, 65]. The non-interacting carrier contribution and the light-matter interaction are calculated using the nearest-neighbor tight-binding approach allowing us to derive analytic expression for the electronic bandstructure $\varepsilon_{\mathbf{k}}^\lambda$ and the carrier-light coupling element $M_{\mathbf{k}}^{\lambda\lambda'}$ [66]. The MSC element is given by the expectation value of the dipole potentials of all adsorbed molecules [59, 6]

$$g_{\mathbf{k}\mathbf{k}'}^{\lambda,\lambda'} = \langle \psi_{\mathbf{k}}^\lambda(\mathbf{r}) | \sum_l \Phi_l^d(\mathbf{r}) | \psi_{\mathbf{k}'}^{\lambda'}(\mathbf{r}) \rangle \quad (4.2)$$

with the tight-binding wave functions $\psi_{\mathbf{k}}^\lambda(\mathbf{r}) = \sum_{j=A,B} \frac{C_j^\lambda(\mathbf{k})}{\sqrt{N}} \sum_{\mathbf{R}_j} e^{i\mathbf{k}\cdot\mathbf{R}_j} \phi(\mathbf{r} - \mathbf{R}_j)$. Here, the quantity \mathbf{R}_j refers to the carbon atoms' coordinates in the sublattice j ($=A,B$), $C_j^\lambda(\mathbf{k})$ denotes the Bloch function's coefficients, and the upper index λ can be either v or c referring to the conduction or the valence band. As orbital functions $\phi(\mathbf{r})$, we assume effective $2p_z$ hydrogen orbitals [66].

Each molecule has a dipole potential, which reads

$$\Phi_l^d(\mathbf{r}) = \frac{e_0}{4\pi\epsilon_0} \frac{\mathbf{d} \cdot (\mathbf{r} - \mathbf{R}_l)}{|\mathbf{r} - \mathbf{R}_l|^3} = \frac{1}{L^3} \sum_{\mathbf{q}} \frac{i}{4\pi\epsilon_0} \frac{\mathbf{d} \cdot \mathbf{q}}{|\mathbf{q}|^2} e^{-i\mathbf{R}_l \cdot \mathbf{q}}. \quad (4.3)$$

Here, we expressed $\Phi_l^d(\mathbf{r})$ in the Fourier-space, where ϵ_0 is the dielectric constant and \mathbf{R}_l the position of the molecule l . In the case of homogeneously distributed molecules on the substrate, one can use the relation $1/N \sum_l^{N_l} \sum_j^N e^{i(\mathbf{k}_1 - \mathbf{k}_2 + \mathbf{q}) \cdot \mathbf{R}_j} e^{i\mathbf{q} \cdot \mathbf{R}_l} = N_l \sum_n \delta_{|\mathbf{q}|, 2n\pi/\Delta\mathbf{R}} \delta_{\mathbf{k}_1 - \mathbf{k}_2, \mathbf{q}}$ for the occurring sums in 4.2 assuming that the number of considered substrate atoms N and the number of adsorbed molecules N_l are large. Even when the substrate is quasi one- or two-dimensional, it is important to take into account all three spatial dimensions to properly describe influence of the dipole potential (4.3) on the substrate. The sum over all adsorbed molecules in (4.2) can be split into the three spatial coordinates $\sum_l^{N_l} e^{-i\mathbf{R}_l \cdot \mathbf{q}} = (\sum_l^{N_{l,x}} e^{-iR_{x,l}q_x})(\sum_l^{N_{l,y}} e^{-iR_{y,l}q_y})(\sum_l^{N_{l,z}} e^{-iR_{z,l}q_z})$. For quasi one-dimensional hybrid-systems (e.g. AGNRs), this leads to the following MSC element

$$g_{\mathbf{k}, \mathbf{k}'}^{\lambda, \lambda'} = \frac{ie_0}{\epsilon_0} n_x \sum_{n=0} \delta_{|k_x - k'_x|, 2n\pi/\Delta R_x} \xi_{1D}^{\mathbf{d}, \lambda, \lambda'}(\mathbf{k} - \mathbf{k}'). \quad (4.4)$$

For a two-dimensional structure, such as graphene, the MSC element reads

$$g_{\mathbf{k}, \mathbf{k}'}^{\lambda, \lambda'} = \frac{ie_0}{\epsilon_0} n_y \sum_{u=0} \delta_{|k_{1y} - k_{2y}|, 2u\pi/\Delta R_y} n_x \sum_{n=0} \delta_{|k_{1x} - k_{2x}|, 2n\pi/\Delta R_x} \xi_{2D}^{\mathbf{d}, \lambda, \lambda'}(\mathbf{k} - \mathbf{k}'). \quad (4.5)$$

Here, $n_{x(y)} = N_{l,x(y)}/L$ is the molecule density on the substrate and $\Delta R_{x(y)}$ is the molecule-molecule distance in x(y)-direction, cf. 3.1 (a) and (b). The appearing confinement function $\xi_{1D}^{\mathbf{d}, \lambda, \lambda'}(\mathbf{k} - \mathbf{k}')$ for one dimensional hybrid systems is given by

$$\xi_{1D}^{\mathbf{d}, \lambda, \lambda'}(\mathbf{k} - \mathbf{k}') = \frac{1}{4\pi^2 N_c} \sum_{j=A,B} \sum_{R_{y,j}} \sum_{\mathbf{R}_{\perp,l}} [C_j^\lambda(\mathbf{k})]^* C_j^{\lambda'}(\mathbf{k}') e^{i(k_y - k'_y)R_{y,j}} \delta_{k_x - k'_x, q_x} \int d\mathbf{q} |\phi_{pz}(q)|^2 \frac{\mathbf{d} \cdot \mathbf{q}}{|\mathbf{q}|^2} e^{-i\mathbf{q}_{\perp} \cdot \mathbf{R}_{\perp,l}} e^{iq_y R_{y,j}} \quad (4.6)$$

includes the parallel (k_x, q_x) and the orthogonal ($k_y, \mathbf{q}_{\perp} = (0, q_y, q_z)$) confinement contributions. For a two-dimensional system, the function further simplifies to

$$\xi_{2D}^{\mathbf{d}, \lambda, \lambda'}(\mathbf{k} - \mathbf{k}') = \frac{1}{2\pi} \sum_{j=A,B} [C_j^\lambda(\mathbf{k})]^* C_j^{\lambda'}(\mathbf{k}') \delta_{\mathbf{k} - \mathbf{k}', \mathbf{q}} \int d\mathbf{q} |\phi_{pz}(q)|^2 \frac{\mathbf{d} \cdot \mathbf{q}}{|\mathbf{q}|^2} e^{-iq_z R_z} \quad (4.7)$$

with the parallel ($\mathbf{k} = (k_x, k_y)$) and the orthogonal ($q_\perp = q_z$) confinement contribution. The sum over $\mathbf{R}_{\perp,l}$ includes the coordinates of the adsorbed molecules perpendicular to the substrate. The dipole potential decays with the distance from the substrate one can therefor reduce the analysis on one layer of molecules in z-direction, in the 2-dim case the perpendicular sum has only one term $\mathbf{R}_{\perp,l} = \mathbf{R}_\perp = (0, 0, R_z)$ and in the 1-dim case it is the sum over molecules in y-direction $\mathbf{R}_{\perp,l} = (0, R_{y,l}, R_z)$. Furthermore, $\phi_{pz}(q)$ is the Fourier transformed p_z -orbital for carbon atoms. Note that $|\phi_{pz}(q)|^2 = (1 + q^2/P_0^2 - 6q_z^2/P_0^2)/(1 + q^2/P_0^2)^4 \approx 1$ for small momentum q , where $P_0 = Z_{eff}/a_B \gg q$ with the effective charge number of carbon Z_{eff} and the Bohr radius a_B [66].

The molecules form a lattice lying on the substrate, as shown in 3.1 (a) and (b), which allows momentum transfers inversely proportional to its “lattice constant”, namely the molecule-molecule distance $\Delta R_{x(y)}$. For the quasi one-dimensional nanoribbon, the momentum transfer reads $k_x - k'_x = 2n\pi/\Delta R_x$, while for the two-dimensional graphene, it can also occur in y direction, i.e. $k_y - k'_y = 2u\pi/\Delta R_y$.

Since $g_{\mathbf{k}\mathbf{k}'}^{\lambda\lambda'}$ is inversely proportional to $|\mathbf{k} - \mathbf{k}'|$, the MSC strength decreases with the momentum transfer. Furthermore, the molecule-substrate coupling element depends on the molecular coverage, i.e. the density of the adsorbed molecules on the surface of the substrate, and on molecular properties, such as the dipole moment and its orientation [59]. In 4.1(a), the one-dimensional MSC element is shown for different molecular coverages. The momentum constrains lead to a multi-peak structure of the MSC within the Brillouin zone. The closer the molecules to each other, the stronger is the resulting dipole potential. At the same time, the peak separation increases resulting in a reduced number of peaks within the Brillouin zone of the investigated substrate. 4.1(b) shows the MSC for different dipole orientations. If the dipole moment is parallel to the substrate, it vanishes for $\mathbf{k} = \mathbf{k}'$, while for dipoles orientated orthogonally to the substrate, it reaches its maximum at $\mathbf{k} = \mathbf{k}'$. This reflects the dumbbell-like dipole potential in the real space. Now, having calculated the relevant coupling elements, we have all ingredients at hand to derive the equation of motion for the microscopic polarization. Applying the Heisenberg's equation of motion, $i\hbar\dot{p}_{\mathbf{k}}^{vc} = [p_{\mathbf{k}}^{vc}, H]_-$, we find the corresponding Bloch equation in the limit of linear optics

$$\dot{p}_{\mathbf{k}}^{vc} = \varepsilon_{\mathbf{k}\mathbf{k}'} p_{\mathbf{k}}^{vc} + \frac{i}{\hbar} \sum_{\mathbf{k}'} (g_{\mathbf{k}'\mathbf{k}}^{vv} \sigma_{\mathbf{k}'\mathbf{k}}^{vc} - g_{\mathbf{k}\mathbf{k}'}^{cc} \sigma_{\mathbf{k}\mathbf{k}'}^{vc}) + \frac{e_0}{m_0} \mathbf{M}_{cv} \mathbf{A}(t). \quad (4.8)$$

Here, $\varepsilon_{\mathbf{k}\mathbf{k}'} = \varepsilon_{\mathbf{k}}^v - \varepsilon_{\mathbf{k}'}^c + i\gamma$ is the energy difference between the initial state $\varepsilon_{\mathbf{k}}^c$ and the final state $\varepsilon_{\mathbf{k}'}^v$. Furthermore, γ is a phenomenological dephasing rate taking into account scattering terms beyond the Hartree Fock level. It determines the width of the absorption resonances and

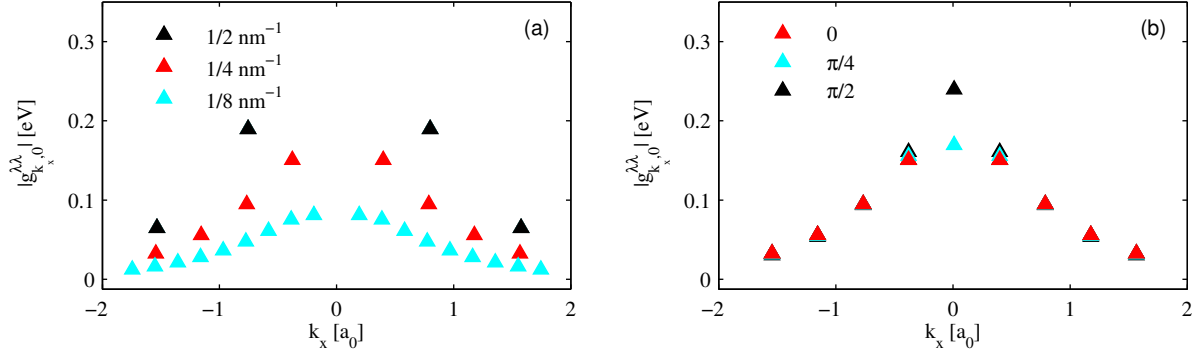


Figure 4.1: Molecule-substrate coupling (MSC) element $g_{\mathbf{k},\mathbf{k}'=0}^{\lambda,\lambda'}$ as a function of momentum k for different a) molecular coverages $n_x = 0.5/nm, 0.25/nm, 0.125/nm$ and b) dipole orientations $\alpha = 0, \pi/2, \alpha = \pi$, cf. 3.1. Note that the appearing peaks are characterized by a momentum transfer, which is inversely proportional to the molecule-molecule distance on the substrate.

has no influence on their position. It has been chosen as $50 \text{ meV}/\hbar$ for all nanoribbons and $125 \text{ meV}/\hbar$ for graphene to account for the experimentally observed larger broadening of graphene [57, 15]. We find that the presence of the molecule-induced dipole field gives rise to indirect optical transitions described by $\sigma_{\mathbf{k}\mathbf{k}'}^{\lambda,\lambda'} = \langle a_{\mathbf{k},\lambda}^\dagger a_{\mathbf{k}',\lambda'} \rangle$. The corresponding equation of motion reads

$$\dot{\sigma}_{\mathbf{k}\mathbf{k}'}^{vc} = \varepsilon_{\mathbf{k}\mathbf{k}'} \sigma_{\mathbf{k}\mathbf{k}'}^{vc} + \frac{i}{\hbar} \sum_{\mathbf{p}} (g_{\mathbf{p}\mathbf{k}}^{vv} \sigma_{\mathbf{p}\mathbf{k}'}^{vc} - g_{\mathbf{k}'\mathbf{p}}^{cc} \sigma_{\mathbf{k}\mathbf{p}}^{vc}) + \frac{e_0}{m_0} \mathbf{M}_{cv} \mathbf{A}(t) \delta_{\mathbf{k}\mathbf{k}'}. \quad (4.9)$$

The dynamics of the diagonal terms ($\mathbf{k} = \mathbf{k}'$) corresponds to the microscopic polarization from 4.8. In the following, we solve the above equations of motion and obtain the microscopic polarization, which is needed to calculate the absorption coefficient in 4.1. We compare the results for pristine, spiropyran (SP)-, and merocyanine (MC)-functionalized nanoribbons and graphene.

4.1 IMPACT OF SUBSTRATE-MOLECULE COUPLING ON OPTICAL ABSORPTION

The optical absorption of a SP- and MC-functionalized AGNR with a width of 2.5 nm ($N_c = 21$) is shown for two exemplary transitions in 4.2 (a) and (b). The observed features for the energetically lowest transition (E_{11} -transition) agree well with our previous work on carbon nanotubes [59, 65]. The molecule-substrate coupling introduces an asymmetric peak splitting leading to a considerable red-shift of the E_{11} absorption peak including the appearance of a side peak en-

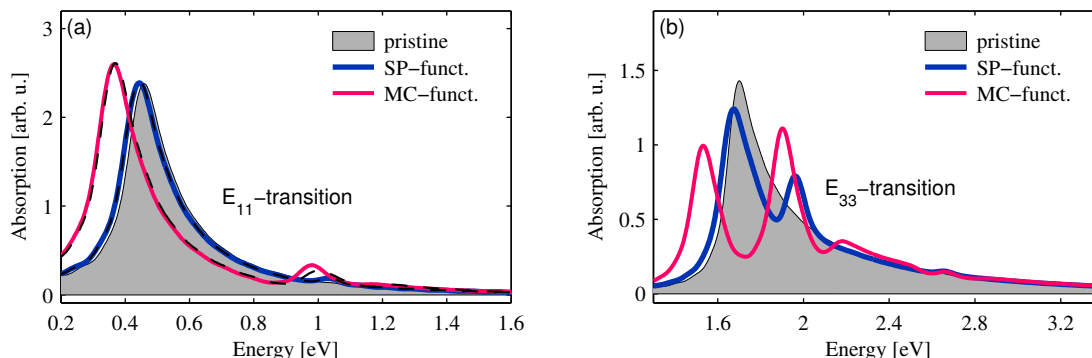


Figure 4.2: Absorption spectrum of pristine (grey area), MC- and SP-functionalized AGNRs with a width of approximately 2.5nm ($N_c = 21$) showing (a) the energetically lowest E_{11} -transition as well as (b) the energetically higher E_{33} -transition. The molecule-substrate coupling (MSC) strongly affects the absorption of nanoribbons: There is an asymmetric splitting of the pristine resonance, in particular in the case of the merocyanine (MC) molecule, which is characterized by a large dipole moment. While for E_{11} the strongest resonance is red-shifted with respect to the pristine peak, in the case of E_{33} the peak located above the pristine resonance is more pronounced. The dashed lines in (a) show the results obtained with the approximation introduced in 4.10.

energetically above the pristine resonance. For the energetically higher E_{33} -transitions, the MSC leads to a qualitatively different picture, cf. 4.2 (b). Here, the asymmetric peak splitting gives rise to the strongest peak energetically above the pristine resonance. Since the MSC element is the same for both transitions, this observation implies the importance of the electronic bandstructure on the substrate-molecule coupling.

Besides the bandstructure, we find that the dimensionality of the hybrid system plays a significant role. 4.3 (a) shows the absorption spectrum of MC- and SP-functionalized graphene. In contrast to AGNRs, the two-dimensional graphene substrate is only affected by the MSC around the high symmetric points at the edges of the Brillouin zone, namely the Dirac (K point) and the saddle-point (M point). While the absorption is clearly enhanced at the Dirac point, it is slightly reduced at the saddle-point, where we also observe a weak peak splitting resulting in a broadening of the absorption resonance.

In the next section, we will first discuss the influence of the electronic bandstructure on the MSC in one-dimensional nanoribbons and then, we will focus on the impact of dimensionality by increasing the width of nanoribbons up to a two-dimensional graphene sheet.

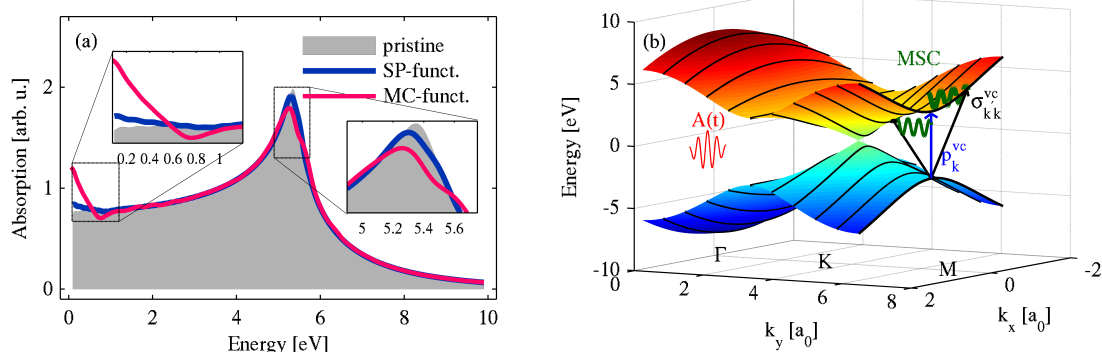


Figure 4.3: (a) Absorption spectrum of pristine (grey area), MC-, and SP-functionalized graphene. The absorption is influenced by the molecule-substrate coupling only at the high-symmetry points. Close to the Dirac-point, the absorption of functionalized graphene is clearly enhanced. Around the saddle-point, we observe a small peak broadening due to the appearance of a high-energy shoulder. b) Schematic illustration of the molecule-induced optical scattering processes within the two-dimensional graphene bandstructure. The black lines show the subbands of an exemplary AGNR. The MSC allows transitions between subbands of different band number as discussed in section 4.

4.2 IMPACT ON ONE-DIMENSIONAL NANORIBBONS

As already shown in the theoretical part, the MSC can give rise to momentum transfers inversely proportional to the molecule-molecule distance, cf. Eq. 4.4. Due to the spatial extension of spiropyran molecules, a reasonable distance is in the range of a few nm and since the lattice constant of graphene is smaller by an order of magnitude, the MSC allows multiple indirect transitions within the Brillouin zone. As can be seen from 4.1 (a) the MSC is large for small momentum transfers. We refer to the largest (second largest) term as the A-term (B-term). For parallel oriented dipoles, this corresponds to the $n=1$ ($n=2$) term in 4.4 allowing a momentum transfer of $\mathbf{k} - \mathbf{k}' = \pm 2\pi/\Delta R_l$ ($\mathbf{k} - \mathbf{k}' = \pm 4\pi/\Delta R_l$). In 4.4 (a), (c) we show the absorption spectrum of the two energetically lowest transition E_{11} and E_{22} taking separately into account the different contributions of the MSC, i.e. A, A+B, and all terms. The A-term dominates the coupling leading to three resonances, in both cases the dominant peak is found energetically below the pristine resonance. Taking into account only the A-term, we are able to describe well the absorption spectrum of functionalized nanoribbons. However, while in 4.4 (a) the side peaks energetically above the pristine resonance are hardly visible and are negligibly small, they are considerably large in 4.4 (c), also the full calculations show a fourth weak resonance in (c) which can not be described by the A-term alone. Adding also the B-term, we find an excellent agreement with the full calculation containing all contributions. Note that the B-term slightly shifts the adsorption spectrum towards lower energies and is responsible for the appearance of

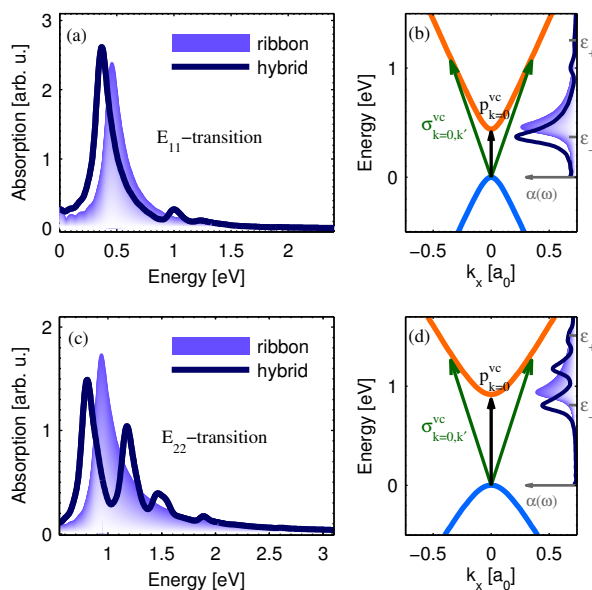


Figure 4.4: Absorption spectra of (a) E_{11} and (b) E_{22} transition in an exemplary AGNR ($N_c = 21$) illustrating the impact of different contributions to the MSC, cf. 4.4 (A-term denoting the $n=1$ and B-term denoting the $n=2$ contribution). (b) and (d) represent schematic illustrations of the corresponding indirect optical transitions, where ω_- and ω_+ indicate the analytically predicted resonances from simplified 4.12.

the weak resonance around 2 eV in the case of the E_{22} transition.

In 4.4 (b) and (d), the underlying optical transitions are schematically shown, where the A(B)-terms give rise to indirect transitions microscopically described by $\sigma_{k_{A(B)},k}^{vc}$. To obtain physical insights into the substrate-molecule coupling, we reduce the complexity of the equations to the dominant terms. Since the momentum of a photon is negligibly small, the light-matter interaction only gives rise to diagonal terms $\mathbf{k} = \mathbf{k}'$, i.e. the microscopic polarization $p_{\mathbf{k}}^{vc}$. Also the off-diagonal terms $\sigma_{\mathbf{k}\mathbf{k}'}^{vc}$ ($\mathbf{k} \neq \mathbf{k}'$) are introduced by the MSC elements coupling to the diagonal terms. This implies that the dynamics are predominantly determined by the diagonal terms of the microscopic polarization $p_{\mathbf{k}}^{vc}$. Therefore, one can assume

$$\sigma_{\mathbf{k}\mathbf{k}'}(t) \propto \sum_{\mathbf{p}} [g_{\mathbf{p}\mathbf{k}}^{cc} \sigma_{\mathbf{p}\mathbf{k}'}^{vc}(t) - g_{\mathbf{k}'\mathbf{p}}^{vv} \sigma_{\mathbf{k}\mathbf{p}}^{vc}(t)] \approx g_{\mathbf{k}'\mathbf{k}} (p_{\mathbf{k}}^{vc}(t) - p_{\mathbf{k}'}^{vc}(t)), \quad (4.10)$$

where we used that $g_{\mathbf{p}\mathbf{k}}^{cc} = g_{\mathbf{p}\mathbf{k}}^{vv}$. With this assumption, one can express 4.8 in the Fourier-space as

$$p_{\mathbf{k}}^{vc}(\omega) = \frac{\Omega(\omega) - \frac{2i}{\hbar} \sum_{\mathbf{k}'} \frac{|g_{\mathbf{k}\mathbf{k}'}|^2 p_{\mathbf{k}'}^{vc}(\omega)}{\varepsilon_{\mathbf{k}\mathbf{k}'} - \hbar\omega}}{i\varepsilon_{\mathbf{k}\mathbf{k}} - i\hbar\omega - \frac{2i}{\hbar} \sum_{\mathbf{k}'} \frac{|g_{\mathbf{k}\mathbf{k}'}|^2}{\varepsilon_{\mathbf{k}\mathbf{k}'} - \hbar\omega}}. \quad (4.11)$$

The dashed black lines in 4.2 (a) demonstrate the validity of the approximation and of 4.11. It shows a very good agreement with the absorption spectrum obtained from the full calculation based on 4.8. Optical resonances appear, where the denominator in 4.11 becomes zero. For optical transitions at $\mathbf{k} = 0$ (schematically shown in 4.4 (b), (d)), the resonant frequencies can be analytically obtained. Since the bandstructure is symmetric around $\mathbf{k} = 0$, i.e. $\varepsilon_{-\mathbf{k}}^\lambda = \varepsilon_{\mathbf{k}}^\lambda$ and the sum $\sum_{\mathbf{k}'}$ can be easily evaluated via $\delta_{|k_x - k'_x|, 2\pi/\Delta R_x}$ focusing on the dominant A-term of the MSC, one can expect that the resonances appear at

$$\hbar\omega_{\pm} = \varepsilon_0 + \frac{\Delta_{\varepsilon_{-2\pi/\Delta R_x}}}{2} \pm \sqrt{\frac{4}{\hbar} |g_{2\pi/\Delta R_x}|^2 + \frac{\Delta_{\varepsilon_{-2\pi/\Delta R_x}}^2}{4}}, \quad (4.12)$$

with $\Delta_{\varepsilon_{-2\pi/\Delta R_x}} = \varepsilon_{0,0} - \varepsilon_{0,-2\pi/\Delta R_x}$. The obtained solutions ω_{\pm} qualitatively describe the peak splitting in the absorption spectra of the hybrid system, cf. 4.4 (b) and (d). However, in order to obtain a quantitative agreement, the reduction to transitions at $\mathbf{k} = 0$ is not sufficient. This simple solution can not e.g. explain the appearance of three resonances, cf. 4.4 (a) and (c). To understand this, we need to investigate the impact of the electronic bandstructure of the substrate.

Since the subbands of an AGNR are described by complex functions (e.g. hyperbolic slices of the Dirac cone) it is of advantage to focus in a first study on simple systems to understand the elementary mechanisms behind the MSC. Therefore, we consider systems with a parabolic bandstructure $\varepsilon_k^{\pm} = \pm(c k^2 + \varepsilon_{gap})$ with the bandgap ε_{gap} and the curvature c . In 4.5 (a), the absorption spectra of such functionalized parabolic trial systems are plotted for different curvatures c . 4.5 (b) shows the peak position and intensity as a function of the band curvature with respect to the pristine resonance. Triangles with tip pointing down and triangles with tip pointing up correspond to peaks located energetically below and above the pristine response, respectively. The larger the triangle, the higher the peak intensity (the size is relative to the pristine peak). The peak intensity increases close to the pristine resonance due to the enhanced density of states. 4.5 (b) illustrates that the simple solution ω_{\pm} is valid for systems with a large curvature c . In our example, for $c > 0.2 \text{ nm}^{-2} \text{ eV}$, two resonances are found as predicted by the analytic solutions. Is the curvature large enough, such that the density of states is decaying fast with growing $|\mathbf{k}|$, we find $p_{\mathbf{k}=0}(\omega)$ as the dominant microscopic polarization. However, for smaller curvatures the contributions of $p_{\mathbf{k}\neq 0}(\omega)$ have to be taken into account to understand the features of the absorption spectrum. Since the bandstructure is not symmetric around $\mathbf{k} \neq 0$, we find more than two resonances for ever contributing $p_{\mathbf{k}\neq 0}^{cv}$. The smaller the curvature, the more $p_{\mathbf{k}\neq 0}^{vc}(\omega)$ contribute, and the more complex is the resulting spectrum. However, note that transitions between dispersion-free valence and conduction bands are not affected by the MSC,

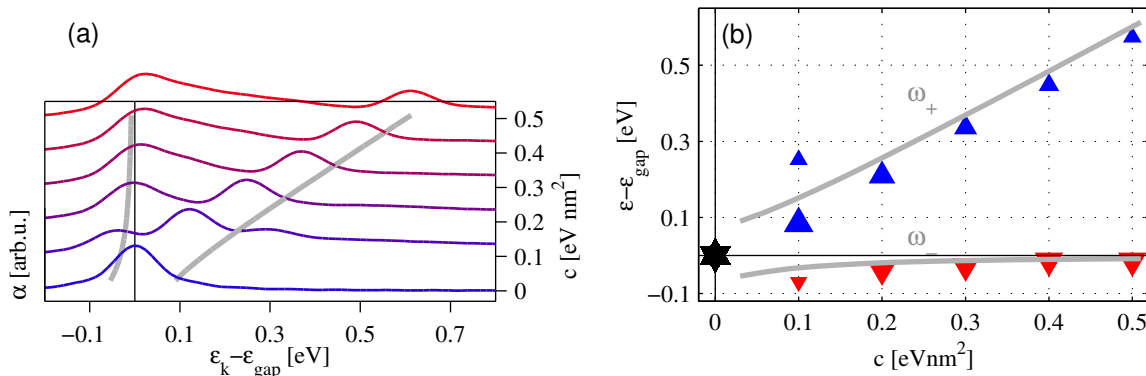


Figure 4.5: (a) Absorption spectra of functionalized nanostructures with a parabolic bandstructure $\varepsilon_k^\pm = \pm(ck^2 + \varepsilon_{gap})$. Note that only the dominant MSC contributions (A-terms) have been included. (b) Spectral peak shift with respect to the pristine resonance as a function of the band curvature c . The triangles with tip pointing up indicate peaks, which are above the pristine resonance, the triangles with tip pointing down indicate those lying below. The black dot shows the resonance for $c = 0$, which is equivalent to the pristine resonance for symmetry reasons. The dot size reflects the peak intensity with respect to the pristine resonance. The closer to the pristine resonance, the more pronounced are the peaks.

cf. black star in 4.5 (b). Between such bands all transitions are equivalent and the MSC terms in 4.9 cancel each other out.

After having discussed the parabolic trial systems, we now investigate the impact of the electronic bandstructure of nanoribbons. In analogy to 4.5 (b), we show the dependence of peak positions and intensity as a function of the corresponding band curvature for characteristic transitions in the nanoribbon with $N_c = 21$, cf. 4.6 (a). The x-axis orders the subbands from the lowest to the highest band curvature (from left to right, respectively). The E_{1212} transition takes place between negatively curved subbands (cf. the magenta line in 4.6 (b)). The corresponding absorption spectrum shows a number of well pronounced red-shifted peaks. The E_{1010} transition involving dispersion-free bands is not affected by the MSC, i.e. there is no peak splitting and no spectral shift, as predicted from the trial system in 4.5. The peak position exactly corresponds to the pristine resonance. Finally, the E_{11} transition is located close to the Dirac point and shows the highest curvature. Here, the red-shifted peak clearly dominates the spectrum. Between the dispersion-free E_{1010} and the E_{11} transition, the band curvature increases. For small curvatures, the peaks located energetically above the pristine resonance are more pronounced in intensity. This changes for transitions in the vicinity of the Dirac point, where the red-shifted peak dominates the spectrum. The change occurs between the E_{33} and the E_{22} transition, cf. also 4.2 (b).

In analogy to the parabolic trial systems, we find that the MSC leads to an asymmetric splitting

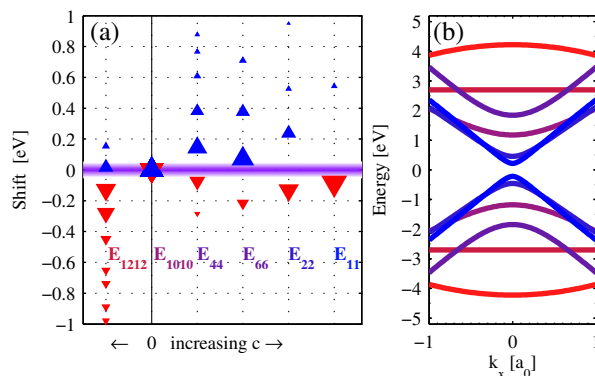


Figure 4.6: a) Spectral peak shift of the MC-functionalized AGNR with a width of 2.5 nm ($N_c = 21$) with respect to the pristine resonance for six characteristic transitions E_{11} , E_{22} , E_{44} , E_{66} , E_{1010} , E_{1212} . Energetically high transitions are weak in intensity due to the vanishing optical matrix element towards the Γ -point. This can be seen in the full spectrum shown in 4.9 (a). The subbands are ordered such that their curvature increases from left to right. The triangle's size indicates the peak intensity with respect to the pristine peak. b) Corresponding conduction and valence bands. The colors match the transitions plotted in a).

of the pristine resonance, which is sensitive to the curvature of the involved subbands: Stronger curvatures lead to a larger energetic difference between the final states of $p_{\mathbf{k}}^{vc}$ and $\sigma_{\mathbf{k}\mathbf{k}'}^{vc}$, cf. 4.4 (b) and (d). The energy difference $\Delta_{\epsilon_{-2\pi/\Delta R_x}} = \epsilon_{0,0} - \epsilon_{0,-2\pi/\Delta R_x}$ shifts the spectrum towards higher energies or in the case of a negatively curved bandstructure towards lower energies, cf. the E_{1212} transition in 4.6.

Furthermore, 4.5 (b) and 4.6 (a) indicate a different bandstructure dependence of the peaks above and below the pristine resonance. While the red-shifted peaks converge to the pristine resonance for large subband curvatures, the shift of the high-energy peaks increases linearly with the curvature. This can be explained as follows: For large energetic differences $\Delta_{\epsilon_{-2\pi/\Delta R_x}}$ with $\Delta_{\epsilon_{-2\pi/\Delta R_x}} \gg |g_{2\pi/\Delta R_x}|$ reflecting the case of large band curvatures, one can use the approximation $\sqrt{4|g_{2\pi/\Delta R_x}|^2/\hbar + \Delta_{\epsilon_{-2\pi/\Delta R_x}}^2}/4 \approx \Delta_{\epsilon_{-2\pi/\Delta R_x}}/2$. In this case, one finds $\omega_+ \approx \epsilon_{\mathbf{k}\mathbf{k}} + \Delta_{\epsilon_{-2\pi/\Delta R_x}}$ and $\omega_- \approx \epsilon_{\mathbf{k}\mathbf{k}}$, cf. 4.12. While ω_- converges towards the pristine resonance at $\epsilon_{0,0}$ for large $\Delta_{\epsilon_{-2\pi/\Delta R_x}}$, ω_+ grows proportionally to $\Delta_{\epsilon_{-2\pi/\Delta R_x}}$, i.e. in particular large $\Delta_{\epsilon_{-2\pi/\Delta R_x}}$ lead to significant spectral shifts towards high energies. However, since the peak intensity strongly decreases with growing spectral shifts, these peaks are very small and will be difficult to detect in experiments.

So far, we have focused on molecule-substrate coupling in one-dimensional nanoribbons. Now, we extend our studies to wider ribbons up to the two-dimensional graphene sheet, where the number of possible indirect optical transitions within the 2-dim Brillouin zone significantly increases.

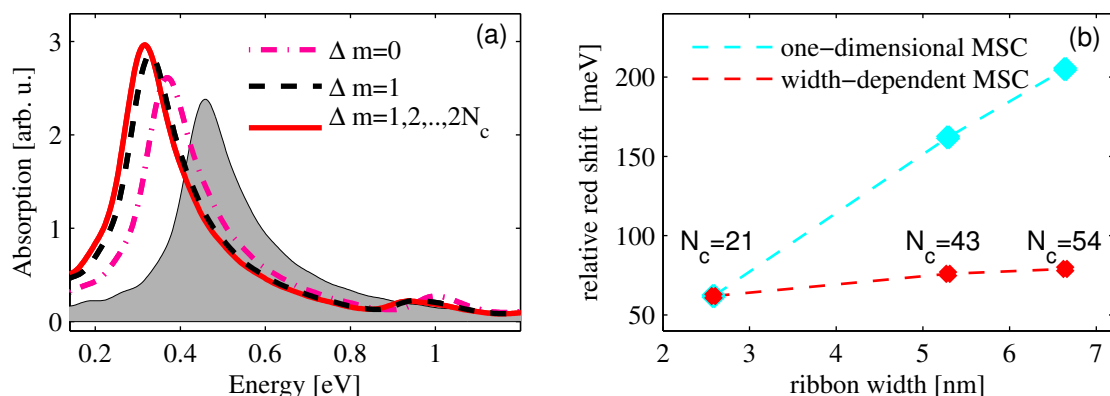


Figure 4.7: a) Absorption spectra of the energetically lowest E_{11} -transition of an AGNR with the width of 2.5nm ($N_c = 21$). Illustration of the importance of optical intersubband transitions taking into account only nearest-neighbors and all subbands, respectively. b) The influence of the intersubband transitions on the spectral red-shift as a function of the nanoribbon width taking into account the 1-dim MSC element from 4.8 and considering the width-dependence from 4.9, respectively. The larger the width, the closer are the subbands and the more efficient is the intersubband scattering (cyan dashed line). At the same time, the larger the width, the more pronounced is the interference of molecular dipole fields resulting in a reduced spectral red-shift (red dashed line).

4.3 FROM 1-DIM NANORIBBON TO 2-DIM GRAPHENE SUBSTRATES

In pristine nanoribbons and graphene, only direct transitions $\mathbf{k} = \mathbf{k}'$ are allowed due to the negligibly small momentum of photons. However, in a structure functionalized with photo-active spiropyran molecules, the molecule-induced dipole fields give rise to a momentum transfer allowing indirect optical transitions. This also includes indirect transition between subbands with different band index, cf. 4.3 (b). As a result, functionalization opens new transition paths in low dimensional systems and can have a considerable impact on their optical properties.

In 4.7 (a), the absorption spectrum of the energetically lowest E_{11} -transition of the functionalized AGNR ($N_c = 21$) is shown with and without including indirect optical intersubband transitions. The additional transition paths enhance the impact of functionalization giving rise to larger spectral shifts. The dominant contribution stems from transitions between the nearest neighbor subbands. The closer the subbands in the reciprocal space, the more important is the intersubband scattering. This is the case for wider ribbons and for graphene, where the states form a quasi-continuum. To identify the intersubband transition-effect, one has to make sure that the bandstructure of the investigated transitions in nanoribbons remains the same. Other-

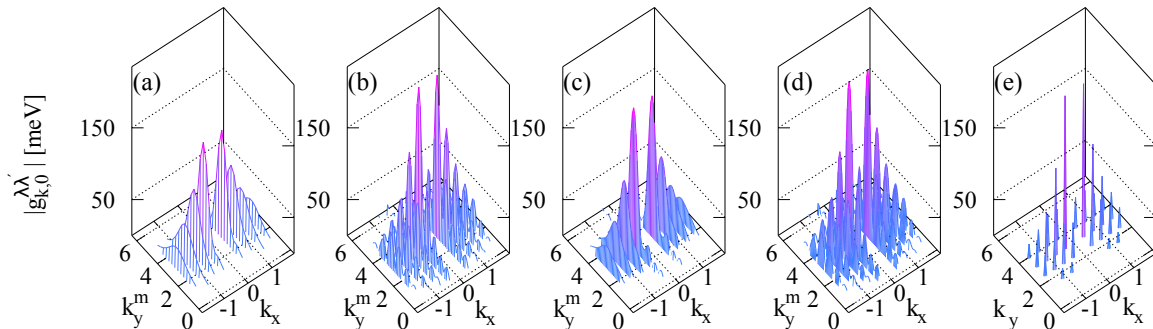


Figure 4.8: The MSC elements of (a)-(d) 1-dim nanoribbons of increasing width up to (e) 2-dim graphene. The number of molecular rows on the substrate surface increases from left to right. The enhanced interference of the corresponding molecular dipole fields leads to a spectrally narrow MSC for substrates with increasing width. Furthermore, we find that for even number of molecular rows, the interference is more pronounced.

wise, these two effects overlap and cannot be distinguished. Therefore, we compare nanoribbons with different widths focusing on transitions with the same band curvature. In 4.7 (b), the E_{22} -transition of a $N_c = 21$ ribbon is compared with the E_{44} -transition of a $N_c = 43$ and a E_{55} -transition of the $N_c = 54$ nanoribbon. For these transition, the curvature of the involved bands is the same and we can focus on the effect of the indirect intersubband transitions. We find that the molecule-induced shift grows with the ribbon width, since more subbands are located within a spectral region, cf. cyan line 4.7 (b). Nevertheless, on the way from a one-dimensional to a two-dimensional structure one also has to consider the interference of the dipole potentials of neighboring molecules, i.e. we have to align multiple rows of molecules along the surface of the increasingly wide nanoribbon, cf. 3.1 (b).

In 4.8 (a-d), the MSC element is plotted as a function of k_x and k_y^m for finite numbers of molecular rows on the surface of the substrate (increasing from (a) one to (d) four rows of molecules). The more dipoles interfere, the spectrally narrower are the peaks of the MSC. In the limiting case of a two-dimensional structure, they become delta-like, cf. 4.8 (e). Note also that an even number of rows leads to maximal interference, cf. (b) and (d), while for an odd number the interference is not complete resulting in spectrally broader MSC peaks, cf. (a) and (c).

In summary, there are two counteracting dimensionality effects on the MSC: On the one hand, the quasi-continuum in two dimensions enhances the possibility of indirect optical transitions. On the other hand, the dipole interference decreases the range of allowed momentum transfer. As a result, we find a moderate increase of the spectral shift towards lower energies with increasing ribbon width, cf. red line 4.7 (b).

4.9 shows the spectrum of (a) a nanoribbon with a width of approx. 2.5 nm ($N_c = 21$), (b) a nanoribbon with a width of approx. 6.5 nm ($N_c = 54$), and (c) graphene in a large energy

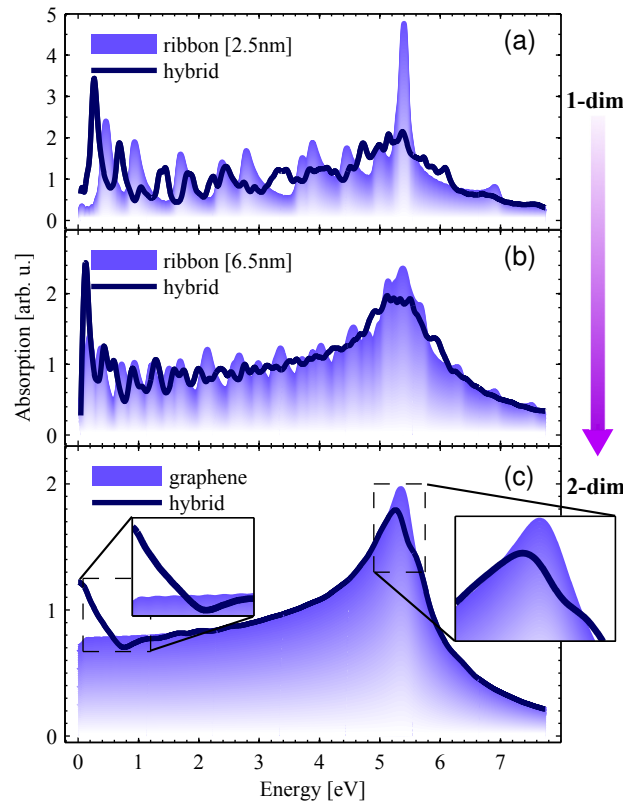


Figure 4.9: The influence of the adsorbed mercocyanine molecule on the absorption spectra of one-dimensional nanoribbons with increasing width up to the two-dimensional graphene. While the spectra of 1-dim nanoribbons are changed along the entire spectral region, the spectrum of graphene shows clear changes only at the high symmetry points of the Brillouin zone, namely the Dirac and the saddle-point.

range. From (a) to (b) the number of peaks increases and the spectrum broadenes. As shown in the previous section, the molecule-carrier coupling induces a significant peak splitting, which even further accelerates the width-dependent broadening towards the graphene spectrum. We also observe that the well pronounced peak at 5.5 eV is strongly suppressed by the MSC. This is surprising since this peak stems from a transition between dispersion-free subbands, where the MSC has been shown to have no influence, cf. 4.5. However, the molecule-substrate coupling considerably increases, when we take into account indirect optical intersubband transitions to neighboring subbands lying energetically above (towards the Γ point) and below (towards the K point) the transition.

In general, we observe that the absorption of nanoribbons is affected by the MSC throughout the entire spectral region (cf. 4.9(a),(b)), while the spectrum of functionalized graphene is only changed at the edges of the Brillouin zone, i.e. in the vicinity of the Dirac and the saddle-point,

cf. 4.9(c). Our calculations predict a clearly enhanced absorption at the Dirac and a slight reduction of the peak at the saddle-point. Close to the Dirac point, the bands are linear and they are characterized by a maximum slope. In analogy to the curvature investigation from 4.5(b) and 4.6 (a), the larger the band slope, the closer are the red-shifted peaks to the pristine resonance and the higher is their intensity. This results in a constructive superposition of these MSC-induced peaks and gives rise to the observed enhanced absorption at the Dirac point, cf. 4.9(c).

The M point is a two-dimensional saddle-point with a positive curvature in k_x -direction and a negative curvature in k_y -direction, cf. 4.3 (b). As discussed in the previous section, positively curved bands with shift the spectrum towards higher energies (cf. 4.6 (a)), whereas negative curvatures account for a shift towards lower energies, cf. 4.6 (b) (E_{1212} -transition). As a result, there is an overlap of these two MSC-induced effects resulting in a slight reduction and broadening of the peak at the saddle-point. The broadening can be ascribed to the appearance of a small high-energy shoulder.

4.4 MOLUCULAR DISTRIBUTIONS: THE IMPACT OF MOLECULE ORIENTATION AND MOLECULAR COVERAGE

Solving Eq.4.9, we have access to the absorption coefficient and can investigate the influence of different functionalization parameters on the optical properties of graphene, cf. Fig. 4.10. Our calculations reveal that the dipole orientation has a small effect on optical properties of functionalized graphene, cf. Fig.4.10 (a). This can be understood from the two-dimensional MSC matrix elements [Fig. 4.1 (a-c)] and its influence on the absorption coefficient [Eq.4.9]. The largest difference in the MSC element with respect to the dipole orientation is observed for $\mathbf{k} = \mathbf{k}'$, cf. the pronounced peak in Fig .4.1 (c). However, this peak does not contribute to the absorption, since the sum in Eq.4.9 cancels for $\mathbf{k} = \mathbf{k}'$. As a result, there is only a minor influence of the dipole orientation on the absorption spectrum. Note that for small molecular coverages, the situation is different. Here, the MSC element shows peaks closer to $\mathbf{k} = \mathbf{k}'$ resulting in a stronger impact of the dipole orientation [59].

The molecular coverage has a significant influence on the absorption of graphene leading to a qualitatively different spectral response, cf. Fig .4.10 (b). At the M point of graphene's Brillouin zone, we observe a complex peak splitting for increasing molecule densities reflecting the multi-peaked structure of the MSC element in Fig. 4.1. The larger the density, the more

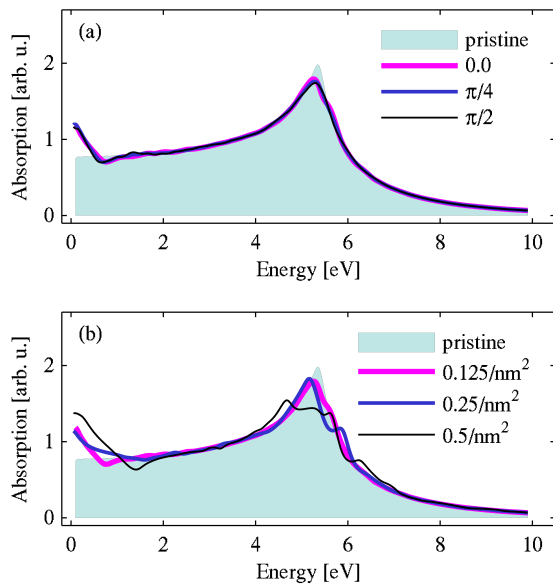


Figure 4.10: Absorption spectrum of merocyanine-functionalized graphene for different (a) dipole orientations and (b) molecule densities illustrating the influence of these functionalization parameters on optical properties of graphene.

efficient is the substrate-molecule coupling. Close to the Dirac point, we find an enhancement of the absorption intensity 4.10. The spectral region of the increased absorption increases with the molecular density.

4.5 CONCLUSION

In summary, our calculations reveal the impact of two important functionalization parameters on the optical properties of functionalized graphene. While the optical response of the system is only slightly affected by the molecular dipole orientation, the experimentally controllable molecular coverage has a significant effect on the absorption spectrum of graphene. This gives new insights into the molecule-substrate coupling and may guide future experiments in terms of optimal functionalization conditions leading to largest changes in optical properties of the substrate.

Part II

Two Dimensional Semiconductors

CHAPTER 5

INTRODUCTION

The study of a new class of materials, here monolayer transition metal dichalcogenides, often leads to the discovery of new physics. The two most important characteristics of the two dimensional semiconductors are,

i) The circular dichroism in combination with strong spin orbit coupling:

This allows the valley and spin selective optical excitation and opens the possibility to generate valley- and spin-polarized non-equilibrium states. As will be shown the circular dichroism can be traced back to the, in contrast to graphene, broken inversion symmetry. As I will show this leads to the opening of a band gap at the K-points and to the unique optical selection rules.

ii) The inherent extraordinary strong Coulomb interaction:

As graphene these two dimensional materials also exhibit a strong intrinsic Coulomb interaction, which leads to highly correlated carrier effects. This leads to strong many-body effects and makes many-particle calculations computationally demanding. But also allows to study high order correlations experimentally, e.g. the formation of tightly bound trions has been observed experimentally [54], and prove and develop theoretical concepts on fundamental questions on many body interactions.

In particular I will show that the strong Coulomb interaction leads to high excitonic binding energies, which are with a few hundred meV one order of magnitude higher than in quantum wells.

CHAPTER 6

TRANSITION METAL DICHALCOGENIDES HAMILTONIAN

We aim for a microscopic theory for the description of the light-matter interaction in transition metal dichalcogenides, here exemplary shown for MoS₂ (the later used parameters for other TMDs are listed in Appendix B). The starting point of our theoretical description is a system Hamiltonian which describes the free motion of non-interacting carriers in the band structure of the material, the Coulomb interaction among the carriers and the interaction of the carriers with a light field Eq. (6.1).

$$H = H_0 + H_C + H_{l-c} \quad (6.1)$$

6.1 TIGHT-BINDING APPROACH

To describe a complex many body system quantitatively, good approximations are needed to find models which are solvable and describe the main aspects of the system.

In finding a microscopic theory for a solid, the most challenging point is the large number of interacting particles. A solid contains by far too many of them to be taken into account entirely. It is therefore important to reduce the number of interactions and correlations to the dominant terms.

In a tight-binding Ansatz, one assumes that the carriers stay close to the atomic sites. Consequently, the dominant interactions are between electrons and cores from the same atom. Under these assumptions one can use the single atom wave functions. The single atom wave functions have little overlap with the nearest neighbours wave function and the overlap reduces to

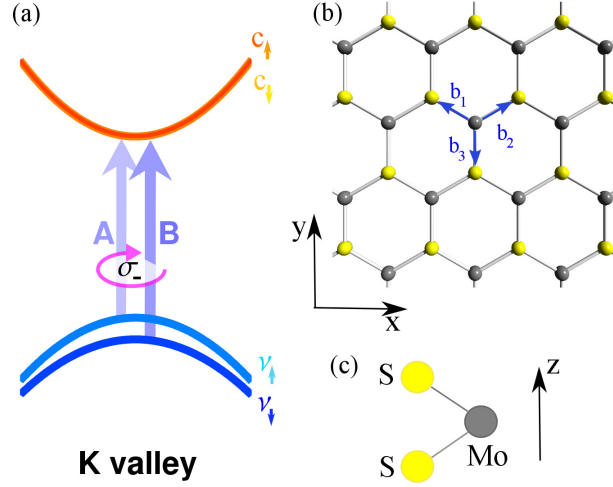


Figure 6.1: (a) Bandstructure of MoS₂ in the vicinity of the K valley. Note that at the K' point, the spin-up and spin-down states are reversed. The arrows schematically indicate the allowed optical transitions leading to A and B excitons in optical spectra. Due to Coulomb-induced electron-hole interaction, the bound excitonic states are located below the conduction band reflecting the corresponding excitonic binding energies. (b) Top view on the hexagonal lattice of MoS₂ lying in the xy-plane. (c) Side view on the MoS₂ structure illustrating the Mo layer sandwiched between the two sulphur atom layers[5].

the next-nearest neighbour and will be even less to the next-to-next-nearest neighbours and so on. Following that argumentation, we can truncate most of the many-particle interactions since their influence will be very small.

Viewed from above MoS_2 is a sheet of S-Mo-S atoms arranged in a honey comb lattice. As pointed out in Fig. 6.1 (b), each honey comb has two base atoms forming sublattices; the sublattice A (Mo) and the sublattice B (S). The sublattices are not identical since one contains all S atoms the other all Mo atoms also the sublattices are shifted by $b = \frac{a}{\sqrt{3}} \approx 1.7\text{\AA}$ in x-direction and the two S-layers are shifted with respect to the Mo-layer by $\approx \pm 1.5\text{\AA}$ in z direction, c.f. Fig.6.1 (c).

PRB: To construct the reciprocal lattice one can use the basis vectors

$$\mathbf{a}_1 = (1, 0) a \quad (6.2)$$

$$\mathbf{a}_2 = \left(\frac{1}{2}, \frac{\sqrt{3}}{2} \right) a \quad (6.3)$$

where $a \approx 3\text{\AA}$ is the lattice constant. With that in hand, the Brillouin zone unit vectors can be

found according to

$$\mathbf{b}_1 = 2\pi \frac{\mathbf{a}_2 \times \mathbf{z}}{A} \quad (6.4)$$

$$\mathbf{b}_2 = 2\pi \frac{\mathbf{z} \times \mathbf{a}_1}{A} \quad (6.5)$$

Here A is the unit cell area ($A = \frac{\sqrt{3}a^2}{2}$) and \mathbf{z} the unit vector orthogonal to \mathbf{a}_1 and \mathbf{a}_2 . We can write the MoS₂ eigenfunction as linear combination of these irreducible basis orbitals of the sublattices A and B.

DFT calculations [101, 104, 73, 46, 13, 51, 72] show that in the vicinity of the optically relevant K points, the valence band is mainly formed by the $1/\sqrt{2}(d_{x^2+y^2} \pm id_{xy})$ orbitals of the transition metal (M) with a minor influence of $1/\sqrt{2}(p_x \pm ip_y)$ orbitals of the chalcogenides (X₂). The conduction band is dominated by d_{z^2} orbitals of the Mo atoms with a minor influence of $1/\sqrt{2}(p_x \pm ip_y)$ orbitals of the S atoms. Here, + and – refer to orbitals forming the K and the K' point, respectively. For a lattice with $2N$ atoms, we use the following tight-binding ansatz for the electronic wave function:

$$\Psi^{\lambda\xi}(\mathbf{k}_s, \mathbf{r}) = \frac{1}{\sqrt{N}} \sum_{j=\text{Mo,S}} C_{j\mathbf{k}_s}^{\lambda\xi} \sum_{\mathbf{R}_j}^N e^{i\mathbf{k}_s \cdot \mathbf{R}_j} \phi_j^{\lambda\xi}(\mathbf{r} - \mathbf{R}_j). \quad (6.6)$$

Here, $\phi_j^{\lambda\xi}(\mathbf{r} - \mathbf{R}_j)$ is the linear combination of the relevant atomic orbitals mentioned above. Furthermore, \mathbf{R}_j denotes the coordinates of the atoms in the sublattice j built by molybdenum and sulphur atoms, and ξ stands for the K and the K' point, respectively. The coefficients $C_{j\mathbf{k}}^{\lambda\xi}$ determine the weight of the single contributions stemming from different orbital functions. They depend on the two-dimensional momentum \mathbf{k} and the index λ_s , denoting either the valence (v_s) or the conduction bands (c_s) with the spin $s = \uparrow$ or \downarrow .

6.1.1 BANDSTRUCTURE AND TB-COEFFICIENTS OF THE K-VALLEYS

Since we use different irreducible basis wave functions at the K and K' point, we solve the Schrödinger equation around both points separately. The two sublattice lead to a set of four linear equations. In our nearest-neighbour approach we assume that $\langle \phi_j^{\lambda\xi}(\mathbf{r} - \mathbf{R}_j) | \phi_i^{\lambda\xi}(\mathbf{r} - \mathbf{R}_i) \rangle = \delta_{j,i}$ is a good approximation, i.e. the overlap of orbital functions of neighbouring sites is neglected. Furthermore, we take into account only the nearest-neighbour hopping integrals $t^\lambda = \langle \phi_j^{\lambda\xi}(\mathbf{r} - \mathbf{R}_j) | H_{\text{kin}} | \phi_i^{\lambda\xi}(\mathbf{r} - \mathbf{R}_i) \rangle$. Then, we obtain an analytical expression for the electronic

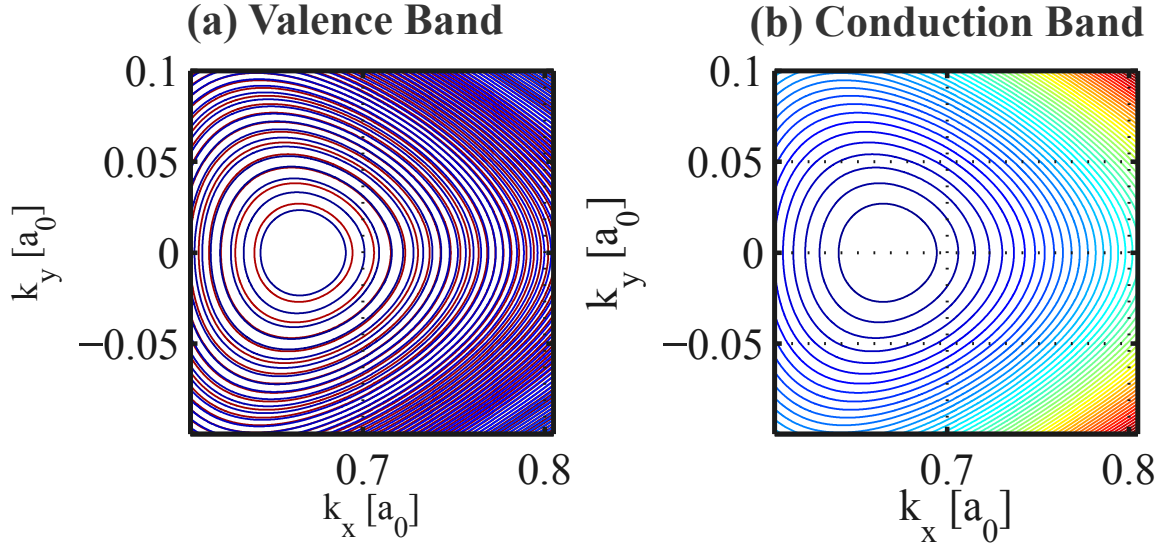


Figure 6.2: TB-Bandstructure of MoS_2 . a) conduction band and b) valence band. The TB bandstructure reproduces the trigonal warping of the bandstructure found in dft calculations. The trigonal warping reflects the three fold symmetry of the neighbouring atom position in real space.

bandstructure in the vicinity of the K and K' points reading

$$\epsilon_{\mathbf{k}_s, \xi}^\lambda = \pm \frac{1}{2} \sqrt{(\Delta \epsilon_\xi^\lambda)^2 + 4|t^\lambda|^2 f(\mathbf{k}_s)}. \quad (6.7)$$

The solution of the above equation is plotted, along the K to K' prime line in Fig.6.3 and as contour plot around the K-point in Fig. 6.2. Note that if next to neighbour contributions are taken into account also the D-points minima in the conduction band positioned between K and Γ -point can be reproduced. This can be understood from the higher distance to next nearest neighbours which leads in the reciprocal space to double the frequency of function $f(\mathbf{k}_s)$. Furthermore, the solution reproduces the trigonal warping effect found in ab initio calculation, which is reflecting the three fold symmetry of the lattice in real space. These details of the bandstructure are however not relevant for this thesis and we use a Taylor expansion for small

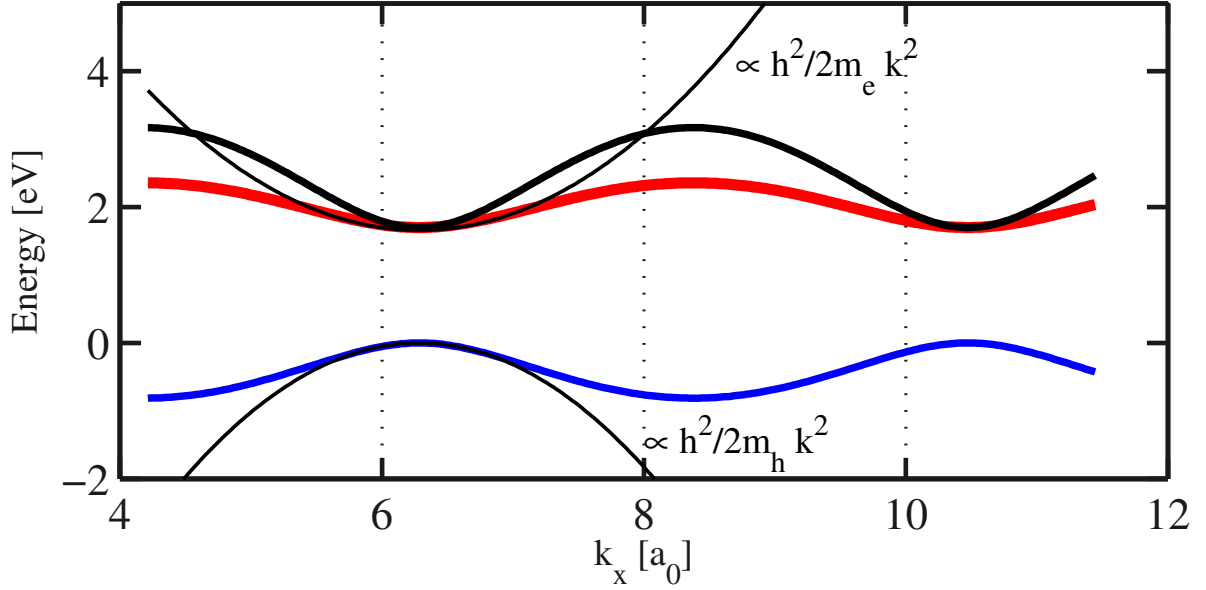


Figure 6.3: Bandstructure along the K-K' line. The black lines show the in this thesis used effective mass approximation.

energies around the $K^{(\prime)}$ point,

$$\epsilon_{\mathbf{k}_s, \xi}^\lambda \approx \pm \left(\frac{|\Delta\epsilon_\xi^\lambda|}{2} + \underbrace{\frac{3|t^\lambda|^2}{2\Delta\epsilon_\xi^\lambda}}_{\equiv t_{s\xi}^\lambda} \mathbf{k}_s^2 \right). \quad (6.8)$$

This parabolic bandstructure has already been shown to be a good approximation in the optically relevant energy region around the K and K' points[101, 72]. The tight-binding hopping integrals t^λ determine the curvature of the electronic bandstructure, cf. Eq. (6.8) where the parabolic fit to the bandstructure is plotted as black line. The values t^{v_s} and t^{c_s} are fixed such that we obtain first-principle values[104, 73, 46, 13] for the effective mass of the valence band $m_{\text{eff}}^v = 0.62m_0$ and of the conduction band $m_{\text{eff}}^c = 0.48m_0$. The spin-dependent band gap $\Delta\epsilon_\xi^\lambda = \epsilon_{\text{gap}} + \xi\epsilon_{\text{soc}}^\lambda$ consists of the band gap energy ϵ_{gap} and the spin-orbit splitting $\epsilon_{\text{soc}}^\lambda$, where $\xi = +, -$ denotes the K and K' point, respectively. As a result, the spin-up (down) electronic state is energetically raised (lowered) by the spin-orbit coupling at the K point and lowered (raised) at the K' point.[56, 77, 77] The broken inversion symmetry in MoS₂ gives rise to the spin-independent band gap $\epsilon_{\text{gap}} = 2.84$ eV that is given by the on-site energy difference of the molybdenum and the sulphur atoms.[78, 16, 76] Both the valence and the conduction band are

split due to the efficient spin-orbit coupling, however, the underlying processes are of different order.[72] Consequently, the valence band splitting of $\varepsilon_{soc}^{vs} = 160$ meV is two orders of magnitude larger than the conduction band splitting of $\varepsilon_{soc}^{cs} = 3$ meV.[56, 88, 55, 46] Figure 6.1 (a) illustrates the obtained electronic bandstructure in the region around the K point. It consists of four parabolic bands stemming from the spin-orbit coupling that splits the valence and conduction band each in two separate spin-up and spin-down bands. We find that the spin-orbit coupling also renormalizes the effective masses of spin-up and spin-down valence bands leading to $m_{\text{eff}}^{v\downarrow} = 0.66$ and $m_{\text{eff}}^{v\uparrow} = 0.575$, cf. Eq.(6.8). This is in good agreement with the results of Kormányos et al.[46]

Solving the Schrödinger equation, we also obtain the eigenfunctions of electrons in MoS₂. Using the normalization conditions, we find for the tight-binding coefficients

$$C_{Mo, \mathbf{k}_s}^{\lambda\xi} = C_{S, \mathbf{k}_s}^{\lambda} g_{\mathbf{k}_s}^{\lambda\xi*}, \quad C_{S, \mathbf{k}_s}^{\lambda\xi} = \frac{\pm 1}{\sqrt{1 + |g_{\mathbf{k}_s}^{\lambda\xi}|^2}},$$

where $g_{\mathbf{k}_s}^{\lambda\xi} = t^\lambda e(\mathbf{k}_s) / (\frac{\Delta\varepsilon_\xi^\lambda}{2} - \varepsilon_{\mathbf{k}_s, \xi}^\lambda)$ and $e(\mathbf{k}_s) = \sum_j^3 e^{i\mathbf{k}_s \cdot \mathbf{b}_j}$ with \mathbf{b}_j connecting the nearest-neighbour atoms.

In the vicinity of the K-points we again perform the Taylor expansion and find the simplified forms,

$$g_{\mathbf{k}_s}^{\lambda\xi} = \frac{i\Delta\varepsilon_\xi^\lambda \exp[\pm i\theta_{\mathbf{k}}]}{|t_s^\lambda| |\mathbf{k}_s|}$$

and with that the coefficients simplify to,

$$C_{Mo, \mathbf{k}_s}^{\lambda\xi} = \pm \frac{i \exp[\pm i\theta_{\mathbf{k}}]}{\sqrt{1 + \frac{2t_{s\xi}^\lambda k_s^2}{3\Delta\varepsilon_\xi^\lambda}}}, \quad C_{S, \mathbf{k}_s}^{\lambda\xi} = \frac{\pm 1}{\sqrt{1 + \frac{3\Delta\varepsilon_\xi^\lambda}{2t_{s\xi}^\lambda k_s^2}}},$$

Here we have solved Schrödingers equation and to derive the tight binding coefficient and our first Hamiltonian,

$$H_0 = \sum_i \epsilon_{\mathbf{k}}^i a_{i, \mathbf{k}}^\dagger a_{i, \mathbf{k}}. \quad (6.9)$$

Where we have introduced the index i which contains the following quantum numbers, the spin s , the band index λ and the valley index ξ . We will keep this more general notation until we have to evaluate the single excitonic contributions in the next chapter. The same notation is

also used for the next chapters, where we first discuss the matrix elements with respect to all quantum numbers and then reduce the index to one index i, j containing all quantum numbers.

6.1.2 OPTICAL MATRIX ELEMENT

While in graphene the band structure is dominated by p_z orbitals exclusively, at least in the vicinities of the K-points, in TMDs a number of different orbital transitions have to be considered in a thorough analysis. The onsite hopping in TMDs can as in graphene be terminated for symmetry reasons. All onsite hoppings are between states of d-like (p-like) symmetry for the transition metal (X the chalcogenides) and together with the nabla operator the integrand is odd and the integral value zero. Therefore, only next-neighbour integrals contribute. For such transitions between p and d like symmetries, which in the present case differ in the azimuthal quantum number $\Delta m = \pm 1$. In contrast to graphene where one can safely reduce the occurring overlap integrals to one dimension, for TMD the change in the azimuthal quantum number leads to a contribution of the Orbitals in two spatial dimensions, e.g. x and y direction. To account for this phase one has to rely on ab initio calculations. To get an idea of the phases present we for now assume that, between valence and conduction band that the overlap integrals would lead to $\mathbf{c}^V \mathbf{c} = c_0 \mathbf{e}_x + i c_0 \mathbf{e}_y$, where c_0 is the value of the overlap integral, which we fit to experimentally measured absorption of $\approx 10\%$. In this approximation the contribution of the first nearest neighbour at $\mathbf{b}_1 = a_0/\sqrt{3} \mathbf{e}_x$ reads,

$$\int d^3r \phi^*(\mathbf{r} + \frac{a}{\sqrt{3}} \mathbf{e}_x) \frac{\partial}{\partial x} \phi(\mathbf{r}) \equiv c_0, \quad (6.10)$$

in x-direction,

$$\int d^3r \phi^*(\mathbf{r} + \frac{a}{\sqrt{3}} \mathbf{e}_x) \frac{\partial}{\partial y} \phi(\mathbf{r}) = i c_0, \quad (6.11)$$

in y-direction and

$$\int d^3r \phi^*(\mathbf{r} + \frac{a}{\sqrt{3}} \mathbf{e}_x) \frac{\partial}{\partial z} \phi(\mathbf{r}) = 0. \quad (6.12)$$

vanishes in z-direction perpendicular to the layer. With this knowledge the other two nearest neighbour contributions can be found via the rotation of \mathbf{b}_1 by $2\pi/3$ and $4\pi/3$. One then finds,

$$\langle \Phi_{\mathbf{k}}^M | \nabla | \Phi_{\mathbf{k}}^{X_2} \rangle = \sum_i e^{i\mathbf{k}\mathbf{b}_i} \frac{\mathbf{c}_{b_i}}{a_{cc}}. \quad (6.13)$$

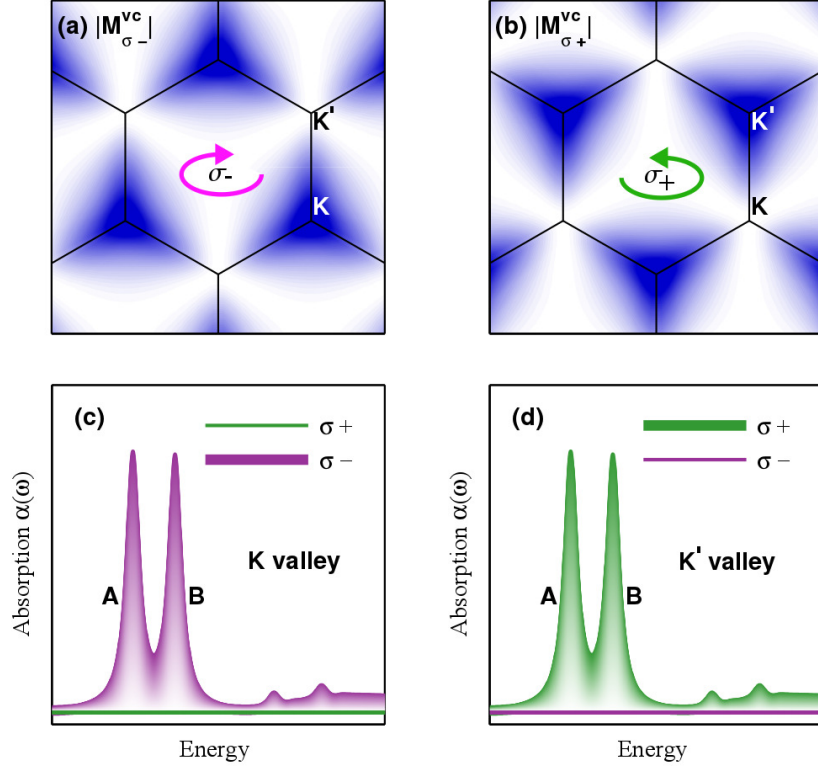


Figure 6.4: The optical matrix element projected in the direction of (a) right- (σ^-) and (b) left-handed (σ^+) circularly polarized light. The corresponding absorption spectra in the spectral region of the (c) K and (d) K' valley after optical excitation with σ^- and σ^+ light, respectively. The figure illustrates a pronounced valley-selective polarization, i.e. the excitation with right-(left-)handed circularly polarized light only leads to an absorption at the K (K') point.

where \mathbf{c}_{b_i} is the rotation vector. Using the Taylor series in the vicinity of K and K' one finds,

$$\sum_i e^{i\mathbf{k}\mathbf{b}_i} \frac{\mathbf{c}_{b_i}}{a_{cc}} = \frac{\mp i\sqrt{3}c_0\mathbf{k} \exp[\mp i\theta_{\mathbf{k}}]}{2a_{M-X}} (\mathbf{e}_x \mp i\mathbf{e}_y). \quad (6.14)$$

However, if one does not include the overlap integral in y-direction one finds the solution for the optical matrix element as,

$$\mathbf{M}^{vc}(\mathbf{k}_s\xi) = \frac{\sqrt{3}c_0|\mathbf{k}|^2 \exp[\mp i\theta_{\mathbf{k}}]}{2N_k^{v_s c_s}} (\mathbf{e}_x \mp i\mathbf{e}_y). \quad (6.15)$$

Here $N_{k_s\xi}^{vc} = \sqrt{1 + \frac{2t_{s\xi}^v k_s^2}{3\Delta\varepsilon_\xi^v}} \sqrt{1 + \frac{3\Delta\varepsilon_\xi^c}{2t_{s\xi}^c k_s^2}} + \sqrt{1 + \frac{3\Delta\varepsilon_\xi^v}{2t_{s\xi}^v k_s^2}} \sqrt{1 + \frac{2t_{s\xi}^c k_s^2}{3\Delta\varepsilon_\xi^c}}$. The coupling to circularly polarized light ($\mathbf{A}^\pm = A_0 \exp[i(\omega t)] (\mathbf{e}_x \pm i\mathbf{e}_y)$) we find that carriers at the K^(') couple

to $\mathbf{A}^{-(+)}$. Both solutions (Eq.6.14 and Eq. 6.15) around the K and K' point are valid for the present analysis. The phase $\exp[\mp i\theta_{\mathbf{k}}]$ in Eq.6.15 cancels for all physical quantities (since physical quantities should not depend on the phase gained by the choice of the coordinates system [4]), e.g. one can without loss of information define $p_{\mathbf{k}} = p_{\mathbf{k}} \exp[\mp i\theta_{\mathbf{k}}]$ or develop the microscopic polarization such that $p_{\mathbf{k}} \rightarrow p_{\mathbf{k}} = \int p_{\mathbf{k}} \exp[\mp i\theta_{\mathbf{k}}] d\theta_{\mathbf{k}}$ the phase is taken into account. However, we have set all occurring overlap integrals to one, to improve the analysis for TMD materials and to account for an exact functional dependence of the matrix element input from ab initio calculations are needed. However, for the aim of the present analysis the solution which captures (in agreement with ab initio calculations) the main aspects of the light matter interaction, the circular dichroism and the coupling to s-like excitonic states, is totally sufficient.

The full solution for the entire Brillouine zone of the optical matrix element projected in the direction of the incident right (left) handed polarized light in Fig.6.4. Here, figure (a) and (b) shows that projected on the left (right) handed component of the circular polarization direction the matrix element M_{\pm} vanishes at the K^(l) point. This effect is called the circular dichroism, which accounts for the fact that carriers at K or K' only couple to the right or left handed component of an incident field, respectively. The components of the absorption coefficient evaluated for right and left handed incident light at K and K' point are plotted in Fig. 6.4 (c) and (d).

Here we could show that the tight binding approach can capture one of the most important properties of the transition metal dichalcogenides. The unique light matter interacting leads to circular dichroism and opens the possibility for optically induced spin-valley polarized states. Furthermore, we can now formulate the light matter Hamiltonian as,

$$H_0 = \sum_{i,j \neq i} \mathbf{M}_{\mathbf{k}}^{ij} \cdot \mathbf{A} a_{i,\mathbf{k}}^{\dagger} a_{j,\mathbf{k}}. \quad (6.16)$$

The Hamiltonian describes the transition possibility, e.g. the possibility that a particle is annihilated in state j and created in state i .

6.1.3 COULOMB MATRIX ELEMENT

Due to the large band gap in TMDs we do only consider coulomb exchange terms in the form $V_{\lambda'\lambda}^{\lambda\lambda'}$ and do not consider Auger like terms. The Hamiltonian for Coulomb interaction reads.

$$H_c = \frac{1}{2} \sum_{\mathbf{k}, \mathbf{k}', \mathbf{q}} \sum_{\lambda_s \lambda'_s} a_{\mathbf{k}, \lambda_s}^{\dagger} a_{\mathbf{k}', \mathbf{q}, \lambda'_s}^{\dagger} a_{\mathbf{k}'+\mathbf{q}, \lambda'_s} a_{\mathbf{k}-\mathbf{q}, \lambda_s} V_{\mathbf{k}, \mathbf{k}', \mathbf{q}}^{\lambda_s \lambda'_s \xi}$$

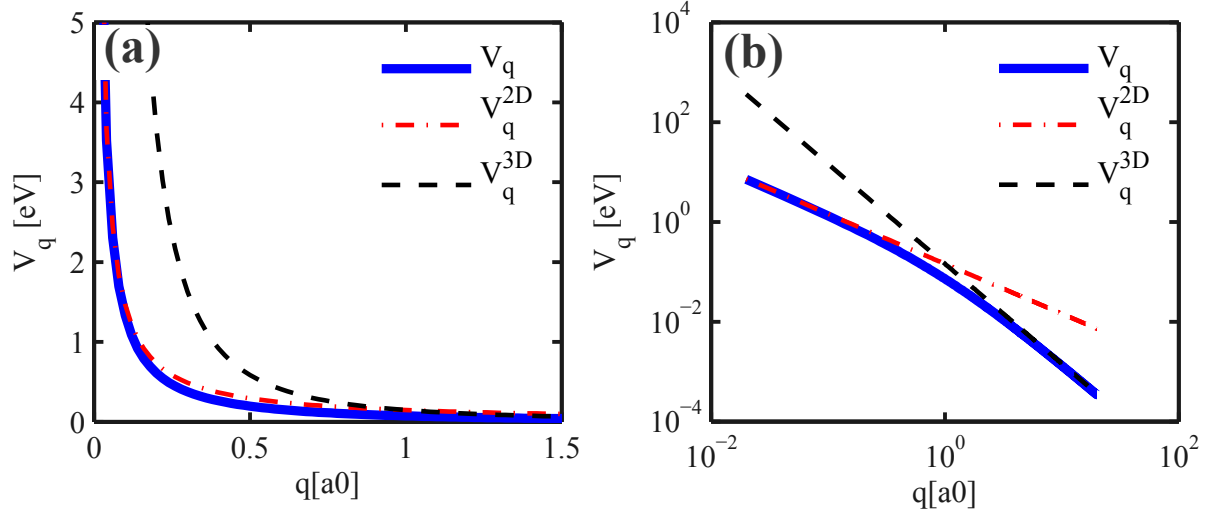


Figure 6.5: Fourier transformed Keldish Coulomb potential. For small q , hence for distant charges, the coulomb potential behaves like a two dimensional potential. The closer the charges are in real space the more dominates the tree dimensional nature of the Potential. The Keldish coulomb potential, describes well the carrier-carrier interaction in a two dimensional lattice within a tree dimensional world.

with the Coulomb matrix element

$$V_{\mathbf{k},\mathbf{k}',\mathbf{q}}^{\lambda_s\lambda'_s\xi} = \Gamma_{\mathbf{k},\mathbf{k}',\mathbf{q}}^{\lambda_s\lambda'_s\xi} V_{\mathbf{q}},$$

the annihilation and creation operators $a_{\mathbf{k},\lambda_s}^\dagger$ and $a_{\mathbf{k},\lambda_s}$, the momenta \mathbf{k}, \mathbf{k}' and the band indices λ_s, λ'_s of the involved electronic states. The Coulomb matrix element is determined by the tight-binding coefficients

$$\Gamma_{\mathbf{k},\mathbf{k}',\mathbf{q}}^{\lambda\lambda'\xi} = \sum_{j,f=S,Mo} C_{f,\mathbf{k}}^{\lambda_s\xi*} C_{j,\mathbf{k}'}^{\lambda'_s\xi*} C_{j,\mathbf{k}'+\mathbf{q}}^{\lambda'\xi} C_{f,\mathbf{k}-\mathbf{q}}^{\lambda_s\xi}$$

In order not to over estimate the coulomb interaction in the two dimensional structure, one has to consider the surrounding of the mono layer. For the situation of a two dimensional semiconductor surrounded by media characterized by different dielectric constants

Keldish [39] derived the coulomb potential,

$$V_{eff}(r) = \frac{e^2}{2r_0} \left[H_0 \left(\frac{r}{r_0} \right) - Y_0 \left(\frac{r}{r_0} \right) \right]. \quad (6.17)$$

Here H_0 and Y_0 are the Struve function and the second kind Besselfunction, respectively. The

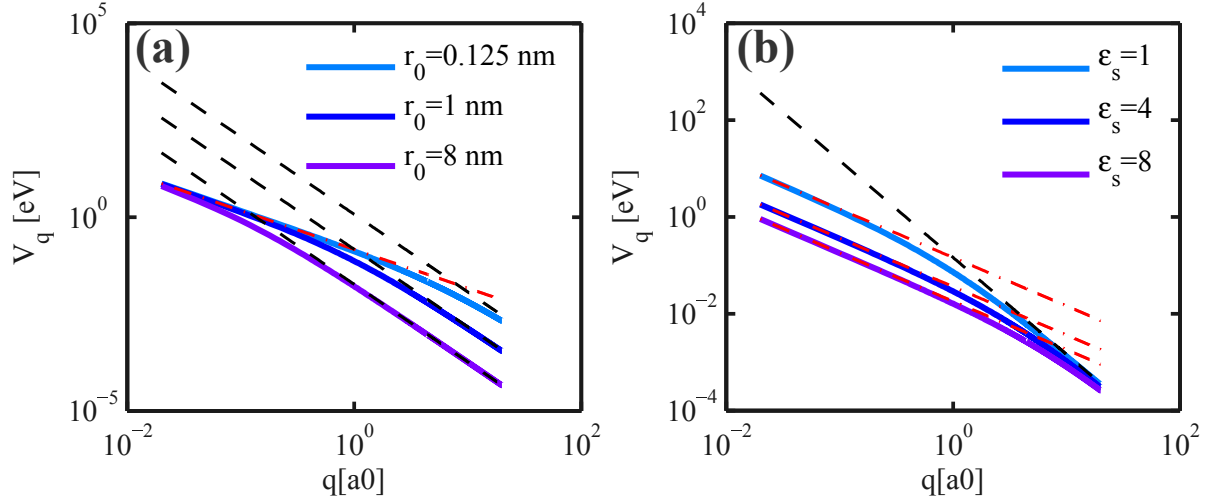


Figure 6.6: Fourier transformed Keldish Coulomb potential, black dashed (red dashed) line show the purely q^{-1} (q^{-2}) part of V_q . (a) the screening length r_0 shifts the crossover from a two dimensional to a three dimensional behaviour. The larger the screening length the earlier is the q^{-2} dependence dominates. (b) Coulomb potential in dependence on the dielectric environment. The higher the refractive index $n = \sqrt{\epsilon_s}$ of the environment the stronger screened is the coulomb potential for small q . The three dimensional part of the coulomb interaction (q^{-1}) is predominantly screened by the dielectric environment whereas the two dimensional part (q^{-2}) is screened by the intrinsic screening length $r_0\epsilon_s$.

Keldish formalism allows a consistent treatment of the screening of the coulomb interaction for point charges confined within a two dimensional structure within a three dimensional world. The Fourier-transformation of Eq.6.17 reads,

$$V_{\mathbf{q}} = \frac{e^2}{\epsilon_0\epsilon_s L^2} \frac{1}{|\mathbf{q}| (1 + r_0|\mathbf{q}|)}, \quad (6.18)$$

including the sample size L^2 , the vacuum permittivity ϵ_0 , and the dielectric constant $\epsilon_s = \epsilon_1 + \epsilon_2$ that accounts for the screening from the surrounding media above (ϵ_1) and below (ϵ_2) the investigated monolayer MoS₂. The form of the Coulomb potential corresponds to the expression derived by L. V. Keldysh and P. Cudazzo.[39, 19] including a consistent description of substrate-induced screening in quasi two-dimensional nanostructures with a thickness d . The latter determines the screening length $r_0 = d\epsilon/\epsilon_s$, where $\epsilon = \epsilon_{\perp}$ is assumed to be the in-plane component of the dielectric tensor of the bulk material.[39, 19, 7, 36].

To account for the thickness d of a TMD monolayer layer, we consider the distance between the two chalcogene atoms in the direction perpendicular to the layer (e.g. for MoS₂ we use $d \approx 0.318$ nm)[85, 7].

In the limiting case of small momentum transfers $|\mathbf{q}|$, Eq. (6.18) corresponds to the regular 2D Coulomb potential for large momentum in goes over into the 3D Coulomb potential, c.f. fig.6.5 (a) + (b). Furthermore, we find that r_0 determines the crossover between two dimensional and tree dimensional dependence of the coulomb potential, c.f. Fig 6.6 (a). Furthermore, we find that the dielectric environment screens the three dimensional component via ϵ_s and the intrinsic screening of the monolayer r_0 screens the two dimensional component, c.f. fig.6.6. Interacting point charges with small momentum q are screened by the surrounding medium, while point charges interacting with large momentum are predominantly screened by r_0 hence the inplane component of the dielectric tensor of the monolayer.

Here we derived the coulomb matrix element for two dimensional semiconductors. Following the Keldish formula we find that the long and short range part are screened by the dielectric environment and inplane dielectric constant of the monolayer, respectively. Furthermore, the momentum dependence of the coulomb potential is does not follow a purely two dimensional q^{-1} -dependence but shows a crossover to a three dimensional q^{-2} -behaviour. We will in section 7.1.4 see that this effects the excitonic series of transition metal dichalcogenides and in particular leads to a Non-Rydberg-series.

coupling.

6.1.4 SYSTEM HAMILTONIAN

In this chapter we derived the tight binding Hamiltonian for TMDs. To describe the electronic properties of TMDs microscopically, we paid major attention to the interaction between charged matter and electromagnetic fields.

We have calculated the band structure of TMDs, derived the Coulomb matrix-element to describe the Coulomb interaction among the carriers and the momentum matrix-element to describe the light-matter interaction.

The full tight-binding Hamiltonian for these thesis reads

$$\begin{aligned}
 H = & \sum_{i,\mathbf{k}} \epsilon_{\mathbf{k}}^i a_{i,\mathbf{k}}^\dagger a_{i,\mathbf{k}} + \sum_{\mathbf{k},i \neq j} \frac{e}{m_0} \mathbf{M}_{\mathbf{k}}^{i,j} \cdot \mathbf{A}(t) a_{\lambda,\mathbf{k}}^\dagger a_{\nu,\mathbf{k}} \\
 & + \sum_{\mathbf{k},\mathbf{k}',\mathbf{q}} \sum_{i,j} V_{\mathbf{k},\mathbf{k}',\mathbf{q}}^{ij} a_{\mathbf{k},i}^\dagger a_{\mathbf{k}',j}^\dagger a_{\mathbf{k}'-\mathbf{q},j} a_{\mathbf{k}+\mathbf{q},i}.
 \end{aligned} \tag{6.19}$$

In the next section we use the system Hamiltonian to calculate the time evolution of the density matrix using Heisenberg's equation of motion.

6.2 TMD BLOCH EQUATIONS

In this section we derive the TMD-Bloch equations, hence the equations of motion for the microscopic polarization $p_{\mathbf{k}}$, the electron $f_{\mathbf{k}}^e$ and hole distribution $f_{\mathbf{k}}^h$. The equations describe the microscopic processes of the optically excited 2-dimensional material and will guide us to understand macroscopic observables, e.g. the absorption spectrum. We will first derive the TMD-Bloch equations in a two band model and which is valid for both spin systems and the entire Brillouin zone. Later in the next chapters we will than restrict our analyses to optically active regions of the system (K and K' valley) and include resonant states of both valley (A or B exciton with opposite spin in the two valleys).

In order to calculate the carrier dynamics on a microscopic footing we solve Heisenberg's equation of motion,

$$i\hbar\dot{O} = [O, H]_- \quad (6.20)$$

for the quantities $\rho_{ij} = a_j^\dagger a_i$. Where a_j^\dagger (a_i) creates (annihilates) a particle in state j (i). Here we use the in the previous section 6.1.4 introduced system Hamiltonian consisting of the quasi free carrier Hamiltonian H_0 the Light-matter interaction H_{l-m} and the carrier-carrier interaction H_C . We use the Cluster expansion scheme, introduced in section 2.1, to truncate the many-particle hierarchy problem on the Hartree Fock level[44]. On this level we find the TMD-Bloch equation in the electron-hole picture, where $f_{\mathbf{k}}^e = f_{\mathbf{k}}^c$ is the electron and $f_{\mathbf{k}}^h = 1 - f_{\mathbf{k}}^v$ the hole distribution, as

$$\dot{p}_{\mathbf{k}} = -i\tilde{\omega}_{\mathbf{k}}p_{\mathbf{k}} - i(1 - f_{\mathbf{k}}^h - f_{\mathbf{k}}^e)\tilde{\Omega}_{\mathbf{k}} \quad (6.21)$$

$$\dot{f}_{\mathbf{k}}^\lambda = 2\text{Im} \left[p_{\mathbf{k}}\tilde{\Omega}_{\mathbf{k}}^* \right]. \quad (6.22)$$

This equation has the well known form of the Semiconductor Bloch Equations (SBE)[33]. The Coulomb interaction leads to the renormalization of the band gap energy $\Delta\varepsilon_{\mathbf{k}} = \varepsilon_{\mathbf{k}}^c - \varepsilon_{\mathbf{k}}^v$ resulting in

$$\hbar\tilde{\omega}_{\mathbf{k}} = \Delta\varepsilon_{\mathbf{k}} - \sum_{\mathbf{k}} \left[f_{\mathbf{k}}^e V_{\mathbf{k},\mathbf{k}}^{cc} + f_{\mathbf{k}}^h V_{\mathbf{k},\mathbf{k}}^{vv} \right] \quad (6.23)$$

Note that the band gap energy has been fixed according to first-principle calculations including the GW approximation, the Coulomb-induced energy renormalization of the undoped ground-state is already taken into account [68, 89]. Further more we introduce the abbreviation $\tilde{\Omega}_{\mathbf{k}}$ for

the renormalization of the Rabi frequency $\Omega_{\mathbf{k}} = \mathbf{M}_{\mathbf{k}}^{vc} \cdot \mathbf{A}$ which reads,

$$\hbar\tilde{\Omega}_{\mathbf{k}} = \Omega_{\mathbf{k}} - \sum_{\mathbf{k}} V_{\mathbf{k},\mathbf{k}}^{cv} p_{\mathbf{k}}. \quad (6.24)$$

These equations include all contributions on the Hartree-Fock level and describe the systems answer to a external perturbation via a vector potential $\mathbf{A}(t)$. In order to understand the optical properties and find the important quantities of the system it is necessary to reduce our investigation to the essential aspects.

In this thesis we investigate the TMD-Bloch equations as follows. We will first restrict our analyses on the optically active regions of the Brillouin zone. In the low energy regime the optical properties of TMDs are characterized by excitonic transitions stemming from the K and K' valleys [17, 47, 74, 92, 37, 105, 54].

We will show an analytic solution of the linear absorption spectrum for circularly polarized light for the uncoupled and the coupled K and K' valleys. The presented analyses will give us the excitonic binding energies and valley coupling constants and there dependence on experimental accessible parameters like the doping and substrates dielectric constant. We will than extend our analyses to non linear optics and calculate the differential transmission signal for seperate spin systems.

CHAPTER 7

LINEAR OPTICS

In this Chapter we will show an analytical solution of the linear Absorption spectrum of TMD monolayers in valley uncoupled regime. Our approach gives insights into the microscopic origin of excitonic transitions, their relative oscillator strength, and binding energies. Furthermore, we will derive the radiative dephasing and discuss the inhomogeneous and homogeneous line width of the excitonic absorption peaks.

7.1 ANALYTICAL APPROACH TO EXCITONIC PROPERTIES OF TMDs

In contrast to the bulk TMDs, the monolayer materials exhibits a direct gap giving rise to a strong photo-luminescence, which is characterized by tightly bound excitons and even trion features have been observed.[54] So far, the experimental data [47, 74, 92, 37, 105, 54, 82] has been complemented by a few calculations that significantly vary in their predictions with respect to the excitonic effects .[78, 16, 87, 68, 7, 91, 76] Exploiting the Bethe-Salpeter equation combined with the G_0W_0 approximation, A. Ramasubramaniam et al.[78] predicted the appearance of strongly bound excitons with a binding energy in the range of 1 eV. This is in agreement with the estimation by T. Cheiwchanchamnangij et al.[16] that relies on the Mott-Wannier effective-mass theory. Recently, A. Molina-Sanchez et al.[68] and D. Y. Qiu et al.[76] provided well converged optical spectra in the framework of Bethe-Salpeter including the spin-orbit coupling. Both studies reproduce well the positions of experimentally observed peaks, however they significantly differ in the predicted excitonic binding energies.

In this section we analyse the excitonic properties of TMDs. We calculate the excitonic

binding energies of TMDs (MoS₂, MoSe₂, WS₂ and WSe₂ characterized by different material parameters given in Appendix B) under the influence of doping and the dielectric environment. Furthermore, we calculate the optical absorption spectrum of monolayer molybdenum-disulphide (MoS₂) for circularly polarized light, showing the optical selection rules which describes well the valley-selective polarization in TMDs. In agreement with experimental results, we find the formation of strongly bound electron-hole pairs due to the efficient Coulomb interaction. In the valley uncoupled regime the absorption spectrum of MoS₂ features two pronounced peaks corresponding to the A and B exciton. For MoS₂ on a SiO₂ substrate, these are characterized by binding energies of 455 meV and 465 meV, respectively [5]. Furthermore, we discuss the spectral position of higher excitonic transitions, which do not follow a Rydberg series.

7.1.1 TMD-BLOCH EQUATION IN THE LINEAR REGIME

In the low energy regime the optical properties of TMDs are characterized by excitonic transitions stemming from the K and K' valleys [17, 47, 74, 92, 37, 105, 54]. We therefore restrict our theoretical analyses to these characteristic points of the Brillouin-zone. As we know from the previous Chapter 6.1.1 the states in K and K' valley are energetically degenerated but differ in valley and spin quantum numbers. Using a pulse resonant to the lowest excitonic transition we can use $\mathbf{k} \rightarrow \mathbf{k}, \xi$, where ξ is the valley index. In this chapter we will further assume that the external perturbation via the vector potential $\mathbf{A}(t)$ is small such that it does not change the carrier occupations in the system. With this notation and in the linear limit the Eq.6.21 transforms to,

$$\dot{p}_{\mathbf{k}\xi} = -i\tilde{\omega}_{\mathbf{k}\xi}p_{\mathbf{k}\xi} - i(1 - f_{\mathbf{k}\xi}^h - f_{\mathbf{k}\xi}^e)\tilde{\Omega}_{\mathbf{k}\xi} \quad (7.1)$$

$$\dot{f}_{\mathbf{k}\xi}^\lambda = 0. \quad (7.2)$$

We can now separate the different valley contributions. And find the valley dependent renormalization of the band gap,

$$\hbar\tilde{\omega}_{\mathbf{k},\xi} = \Delta\varepsilon_{\mathbf{k},\xi} - \sum_{\mathbf{k}'\xi'} \left[f_{\mathbf{k}\xi'}^e V_{\mathbf{k},\mathbf{k}',\xi,\xi'}^{cc} + f_{\mathbf{k}\xi'}^h V_{\mathbf{k},\mathbf{k}',\xi,\xi'}^{vv} \right] \quad (7.3)$$

and to the renormalization of the Rabi frequency $\Omega_{\mathbf{k}\xi} = \mathbf{M}_{\mathbf{k}\xi}^{vc} \cdot \mathbf{A}$ resulting in

$$\hbar\tilde{\Omega}_{\mathbf{k}\xi} = \Omega_{\mathbf{k}} - \sum_{\mathbf{k}'\xi'} V_{\mathbf{k},\mathbf{k}',\xi,\xi'}^{cv} p_{\mathbf{k}'\xi'}. \quad (7.4)$$

In contrast to conventional semiconductors the TMD monolayers have two optically active regions within the Brillouin zone, the K and K' valleys. All terms where $\xi' \neq \xi$ induce a coupling between these two regions.

We will first investigate Eq.7.1 within the uncoupled regime and only include terms with $\xi' = \xi$. Considering only one of the two valleys we will discuss the excitonic properties of TMDs including both spins, e.g. discuss the A and B excitons. Furthermore, we will discuss higher excitonic states and the radiative coupling of TMDs. We will then include the Coulomb-induced intervalley coupling and show its effect on the linear absorption spectrum.

7.1.2 ABSORPTION SPECTRUM OF MoS_2

To get insights into the intrinsic properties of the system, we first investigate the valley uncoupled homogeneous solution of Eq. (7.1), which defines the eigenvalue problem,

$$\tilde{\epsilon}_{\mathbf{k},\xi}^s \theta_{\nu_s\xi}^R(\mathbf{k}) - \sum_{\mathbf{k}'} V_{\mathbf{k},\mathbf{k}',\mathbf{q}}^{exc} \theta_{\nu_s\xi}^R(\mathbf{k}') = E_{\nu_s\xi}^R \theta_{\nu_s\xi}^R(\mathbf{k}) \quad (7.5)$$

corresponding to the well-known Wannier equation.[33, 44]. Here we have now included the spin index s which accounts for the different spins split valance and conduction band. In the limit of linear optics it is convenient to define left and right handed eigenfunctions and include all carrier contributions in the excitonic -wavefunctions and -eigenvalues. The right ($\theta_{\nu_s\xi}^R(\mathbf{k})$) and left ($\theta_{\nu_s\xi}^L(\mathbf{k}) = \theta_{\nu_s\xi}^R(\mathbf{k}) / (1 - f_{\mathbf{k}\xi}^{e_s} - f_{\mathbf{k}\xi}^{h_s})$) handed excitonic eigen functions as well as the excitonic eigenvalues $E_{\xi}^{\nu_s}$ are given by the homogeneous solution of the Bloch equations. The excitonic wave functions $\theta_{\nu_s\xi}^R(\mathbf{k})$ determine the oscillator strength of the excitonic transitions appearing in the absorption spectrum. The absorption coefficient $\alpha(\omega)$ is proportional to the imaginary part of the susceptibility $\chi(\omega)$, which can be expressed via the macroscopic current density $j(\omega)$. [58] The latter is directly determined by the microscopic polarization $p_{\mathbf{k}\xi}$. With the solution of Eq. (7.5), we can express the microscopic polarization by transforming Eq.(7.1) using the relations[44]

$$p_{\mathbf{k}\xi}^s = \sum_{\nu_s} p_{\nu_s\xi} \theta_{\nu_s\xi}^L(\mathbf{k}) \quad (7.6)$$

and

$$p_{\nu_s\xi} = \sum_{\mathbf{k}} p_{\mathbf{k}\xi}^s \theta_{\nu_s\xi}^R(\mathbf{k}). \quad (7.7)$$

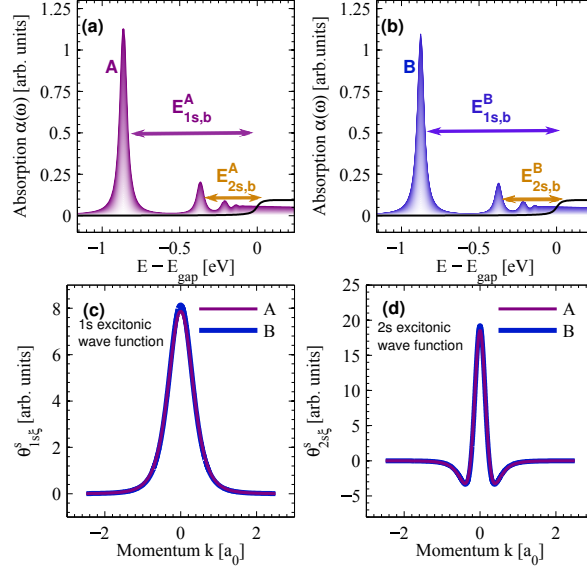


Figure 7.1: Absorption spectrum of the free-standing MoS₂ focusing on the well-pronounced (a) A and (b) B exciton arising from the transition from the two energetically highest spin-split valence bands to the energetically lowest conduction band, respectively. The corresponding excitonic binding energies $E_{1s,b}^{A/B}$ can be directly read off from the difference to the free-particle transitions, cf. the black lines. Note that we have doubled the free-particle absorption intensity for better visibility throughout the paper. Higher excitonic transitions with binding energies $E_{2s,b}^{A/B}$ and $E_{3s,b}^{A/B}$ can also be observed. The excitonic binding energies of higher states do not follow a Rydberg-series, this is discussed in detail in section 7.1.4. The corresponding eigenfunctions $\theta_{\nu_s\xi}^s(\mathbf{k})$ of 1s and 2s excitons are shown in (c) and (d), respectively. They determine the oscillator strength of the excitonic transitions.[5]

The new quantity $p_{\nu_s\xi}$ depends on the excitonic eigenvalues and can be expressed analytically in the frequency domain yielding

$$p_{\nu_s\xi}(\omega) = \frac{\sum_{\mathbf{k}} M_{\sigma\pm}^{\nu_s c_s \xi}(\mathbf{k}) A(\omega) \theta_{\nu_s\xi}^R(\mathbf{k})}{E_{\nu_s\xi} - \hbar\omega - i\gamma}. \quad (7.8)$$

Finally, we obtain for the absorption coefficient the analytical expression [33, 44]

$$\alpha(\omega) = \frac{1}{\epsilon_0 \epsilon_r \omega} \Im \left[\sum_{\nu_s \xi, s} \frac{\Theta_{\nu_s \xi}^s}{E_{\nu_s \xi}^s - \hbar\omega - i\gamma} \right]. \quad (7.9)$$

This equation corresponds to the Elliot formula, which describes the macroscopic answer of the system to an external optical perturbation.[33, 44] Note that, we have for now introduced a phenomenological dephasing rate $\gamma = 25$ meV to account for higher correlation terms neglected

on the Hartree Fock level. In section 7.2, we will discuss the homogeneous and inhomogeneous line width more detailed. For this section, where we focus on the excitonic binding energies we use the phenomenological dephasing rate, it determines the width of transition peaks appearing in the absorption spectrum, however, it does not have any influence on their position or the excitonic binding energy. We find that the oscillator strength of the peaks in the absorption spectrum is determined by the square of the optical matrix element $M_{\sigma\pm}^{v_s c_s \xi}(\mathbf{k})$ and the sum over excitonic wave functions,

$$\Theta_{\nu_s \xi}^s = \sum_{\mathbf{k}} \theta_{\nu_s \xi}(\mathbf{k}, \sigma) M_{\sigma\pm}^{v_s c_s \xi}(\mathbf{k}) \sum_{\mathbf{k}'} [\theta_{\nu_s \xi}^s(\mathbf{k}') M_{\sigma\pm}^{v_s c_s \xi}(\mathbf{k}')]^* \quad (7.10)$$

The eigenvalues $E_{\nu_s \xi}$ of Eq.(7.5) appearing in the denominator of the Elliot formula determine the position of the excitonic peaks as well as their binding energy.

The absorption spectrum of MoS₂ features pronounced peaks clearly arising from excitonic transitions, as free-particle band-to-band transitions in a two-dimensional material give steps in absorption, cf. Figs. 7.1(a) and (b). The appearing two peaks stem from transitions between the two energetically highest spin-split valence bands to the energetically lowest conduction band, cf. Fig. 6.1(a). The energetically lower (higher) transition is denoted as the A (B) exciton in literature.[56] In the case of free-standing MoS₂, i.e. without considering a substrate-induced dielectric background screening of the Coulomb potential, the A exciton is located at 1.9 eV and the B exciton at 2.04 eV. We also calculate the Coulomb-renormalized band-to-band transitions in the absorption spectrum to be able to determine the excitonic binding energies $E_{1s,b}^A = 860$ meV and $E_{1s,b}^B = 870$ meV, cf. the arrows in Figs. 7.1(a) and (b). The difference of 10 meV can be traced back to the unequal effective masses of the spin-split valence bands. Our results are in good agreement with recent first-principle calculations by A. Ramasubramaniam et al.[78] and D. Y. Qiu et al.[76] predicting values in the range of 1 eV. The relatively smaller value obtained in an effective-mass approach by T. C. Berkelbach et al.[7] can be traced back to a stronger screening in their model.

Besides the two main A and B peaks, we also observe further higher excitonic resonances with a much smaller intensity. In qualitative analogy to the Rydberg series in the hydrogen atom, we find a series of optically active exciton states. Quantitatively our calculations show that the the exciton series in TMDs do not follow the Rydberg series, which we will come back to in Section 7.1.4. In the absorption spectrum of MoS₂, we observe the 2s excitonic resonances that are located at 0.5 eV above the A and B excitons (corresponding to the 1s transitions), respectively. They show a weak intensity that is by one magnitude smaller than the corresponding 1s transitions. Their excitonic binding energy $E_{2s,b}^{A/B}$ is in the range of 400 meV. To investigate the

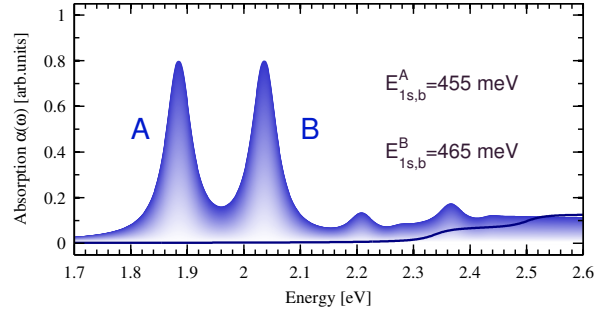


Figure 7.2: Excitonic absorption spectrum of MoS₂ on a silicon substrate. Compared to free-standing molybdenum disulphide shown in Fig. 7.1, the excitonic binding energy is strongly reduced to $E_{1s,b}^A = 455$ and $E_{1s,b}^B = 465$ meV due to the substrate-induced screening of the Coulomb interaction.[5]

relative oscillator strength of the observed peaks, we plot the excitonic eigenfunctions $\theta_{\nu_s\xi}(\mathbf{k})$ found as solution of Eq. (7.5). Figure 7.1(c) reveals that the eigenfunction of the B exciton is slightly higher. We can trace this behaviour back to the difference in the effective mass $m_{\lambda_s}^*$ of the involved electronic bands λ_s . Our calculations show that the oscillator strength is enhanced for increasing $m_{\lambda_s}^*$. Due to the spin-orbit coupling, the effective mass of the energetically higher valence band is larger giving rise to a larger oscillator strength of the B exciton. However, this effect is almost completely cancelled due to the $1/\omega$ -dependence of the absorption coefficient (cf. Eq. (7.9)), which suppresses energetically higher transitions. As a result, the absorption spectrum shows that both peaks have nearly the same oscillator strength.

To compare our results with the recent experimental data,[54] we study the absorption spectrum of MoS₂ on the silicon dioxide substrate. The latter gives rise to an efficient screening of the Coulomb potential affecting the position and the binding energy of excitonic transitions. The corresponding absorption spectrum is shown in Fig.7.2. Compared to free-standing MoS₂, the excitonic binding energies are reduced to $E_{1s,b}^A = 455$ and $E_{1s,b}^B = 465$ meV. Our calculations could not reproduce the measured relative oscillator strength of the A and B excitons. While in the experiment, the A exciton is higher in intensity, our theoretical spectra show nearly the same oscillator strength for both excitons. This might be due to the higher-order effects beyond the considered Hartree-Fock approximation and will be studied in future work.

7.1.3 EFFECT OF SCREENING ON EXCITONIC BINDING ENERGIES

Here we show our results on the excitonic binding energies of different TMDs under the influence of doping and the dielectric environment. Since over 40 TMDs exist all with different intrinsic parameters it is necessary to know which one to choose for a certain application. The

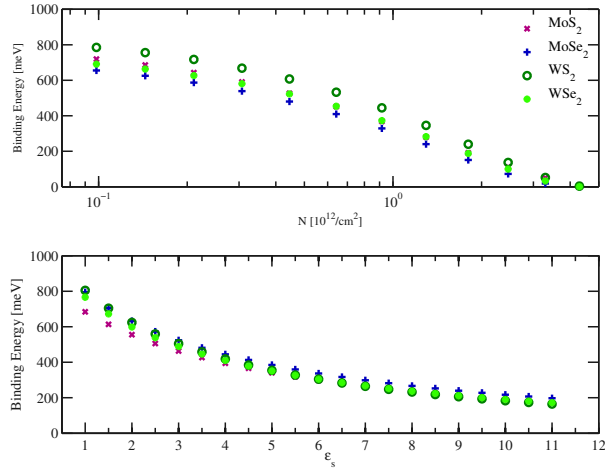


Figure 7.3: Excitonic binding energies of MoS₂, MoSe₂, WS₂ and WSe₂ as a function of (a) the dielectric environment and (b) doping. The excitonic binding energy is strongly effected by both screening effects and shows a reduction of hundreds of meV. Nevertheless, the renormalization of the binding energy is largely compensated by the renormalization of the bandgap and the spectral position of the excitonic resonances is only effected in the range of a tens of meV.

excitonic binding energy is predominantly determined by the coulomb potential and the effective electron and hole mass. While the electron hole mass is a purely intrinsic system parameter the coulomb potential can be screened externally via the dielectric environment or plasma screening (p or n type doping).

In Fig.7.3 we show the excitonic binding energies of the four most prominent TMDs (MoS₂, MoSe₂, WS₂ and WSe₂) in dependence of doping (a) and plasma screening (b). In Agreement with doping study of Steinhoff at al. [89] we find shifts of the excitonic binding energy in the range of hundreds of meV. However, in an absorption spectrum only small shifts of about 50 meV were observed experimentally.[54] Though the screening leads to a strong reduction of the binding energy it also reduces the renormalization of the bandgap (see Fig.7.4), which is given by the repulsive carrier-carrier interaction in Eq.7.1. The attractive electron hole and the repulsive carrier-carrier interaction have opposite sign and consequently shift the excitonic resonance in opposite directions. In total both effects cancel each other out to large extent, which results in a moderate spectral shifts of the excitonic transitions in the range of tens of meV. Though the screening leads to a tremendous reduction of the carrier correlation, reducing the binding energy by hundreds of meV, this has (apart from absorption bleaching in the case of plasma screening via the phase space filling) only a minor effect on the optical properties of the TMD.

These theoretical insights show how sensitive the coulomb interaction is to screening effects. Still the optical properties of the TMDs are comparably stable. As we will discuss later this

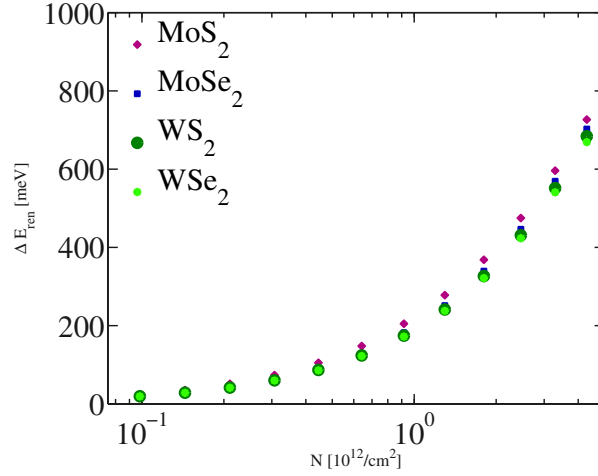


Figure 7.4: Reduction of the Coulomb-induced band gap renormalization for MoS₂, MoSe₂, WS₂ and WSe₂ as a function of doping. The band gap renormalization due to the repulsive carrier-carrier interaction is reduced via plasma screening. Here included via the Lindhard formula. The band gap renormalization is reduced by hundreds of meV which leads to a red shift of the resonances and cancels the blue shift of the reduced binding energies to a large extend.

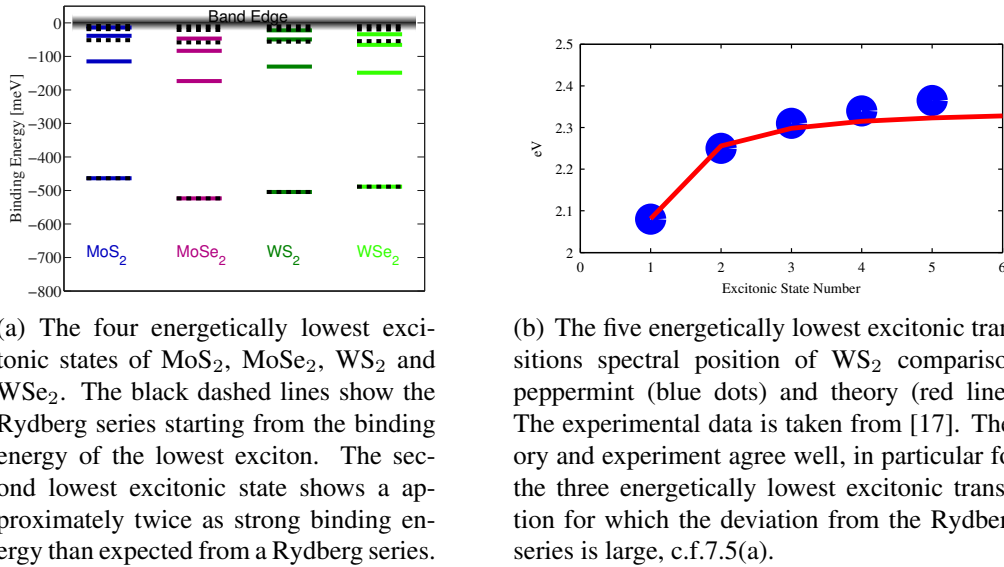
is a crucial point in terms of valley coherence and might lead the road to valleytronics and the exploitation of the valley quantum number in the valley decoupled regime.

7.1.4 HIGHER EXCITONIC TRANSITION

The solution of the Wannier equation gives all excitonic states and eigen values. This can be used in combination with experimental results to find the actual band gap of a TMD on a substrate under different experimental parameters. In order to find the band gap of a semiconductor, it is possible to measure the spectral position of the first excitonic states experimentally and estimate the band gap via the Rydberg series,

$$E^n = \frac{\mu e^4}{2\hbar^2 \epsilon_0^2 \epsilon^2 (n - 0.5)^2}. \quad (7.11)$$

here μ is the effective mass, n the state number, e the electron charge number and ϵ the dielectric constant. [17] As Chernikov et al [17] could show, this is not true for TMD materials in which the coulomb interaction follows the Keldysh formula.[35] The deviation from a hydrogen like coulomb interaction leads to a different series of excitonic states. In agreement with our theory, Chernikov et al came to the conclusion (experimentally and theoretically) that the excitonic states do not follow a Rydberg series.



(a) The four energetically lowest excitonic states of MoS₂, MoSe₂, WS₂ and WSe₂. The black dashed lines show the Rydberg series starting from the binding energy of the lowest exciton. The second lowest excitonic state shows a approximately twice as strong binding energy than expected from a Rydberg series.

(b) The five energetically lowest excitonic transitions spectral position of WS₂ comparison peppermint (blue dots) and theory (red line). The experimental data is taken from [17]. Theory and experiment agree well, in particular for the three energetically lowest excitonic transition for which the deviation from the Rydberg series is large, c.f.7.5(a).

Figure 7.5: Non-Rydberg series in transition metal dichalcogenides

In figure 7.5(b) we plotted our theoretical results in comparison to there experimental data taken from [17]. Our theory (red line) shows a good quantitative agreement with the experimental results (blue points).

In figure 7.5(a) we show the solution of the Wannier equation 7.5 for the lowest four excitonic states of the most prominent TMDs. The calculations are for monolayers on on a SiO₂ substrate. The results are shown with respect to the band gap. All TMDs show a strong deviation from Rydberg series calculated form Eq.7.11 (dashed black lines). Most prominently the second excitonic state shows double the binding energy than expected from the Rydberg series.

7.1.5 CONCLUSIONS

In this section we have presented an analytical description of the excitonic absorption spectrum of the MoS₂ monolayer. We investigate the formation of bound electron-hole pairs and their influence on the absorption spectrum of MoS₂. In agreement with experimental data, our calculations show the possibility of valley-selective polarization as well as the appearance of strongly pronounced A and B excitons with binding energies in the range of few hundreds of meV. Furthermore, we calculated the higher excitonic transitions characterized by much lower intensities. Moreover, we investigated the impact of the excitonic eigenfunctions on the relative oscillator strength of the excitonic peaks as well as the influence of substrate- and carrier-induced screening on the excitonic binding energies. Our theoretical model allows to study the impact of experimentally accessible parameters on excitonic properties of TMDs. The advan-

tage of our approach over ab initio calculations is that we can easily address experimentally accessible parameters like the substrate and plasma screening and study their impact on important system properties. This approach will be extended in the next section to investigate the radiative dephasing and the intervalley coupling.

7.2 RADIATIVE COUPLING

So far we have included higher correlations on a phenomenological level using a large homogeneous broadening $\gamma = 25\text{meV}$ orientated on the inhomogeneous line width found in absorption experiments. This was sufficient since, we focused on the spectral position of the excitonic resonance, given by the excitonic binding energy and the renormalized band gap. Nevertheless, we will now show that our previous assumption is very far from the truth, since we will find that the inhomogeneous and homogeneous line width differ by one order of magnitude. Which is a very important insight for the later sections where we discuss the Coulomb-induced intervalley coupling and non-linear effects, for both a clear separation of homogeneously induced broadening and inhomogeneously induced broadening is of crucial importance. In this section we will present our analyses on the radiative coupling in TMD monolayers and calculate the homogeneous and inhomogeneous broadened absorption spectrum of TMDs[69].

In optical experiments the studied two dimensional monolayer is usually sandwiched between two materials exhibiting different dielectric constants, e.g. substrate (commonly used are SiO_2 or Sapphire) below and vacuum or air above. For this situation one can solve Maxwell's wave equation with the boundary conditions for the electrical field travelling perpendicular to the monolayer, see Appendix C for more details. For the absorbance of a monolayer between two media characterized by the refractive indices n_1 and n_2 , we obtain the following analytic expression,

$$\alpha(\omega) = \frac{\frac{\omega}{c_0 n_1} \Im[\chi_{2D}(\omega)]}{\left| \frac{1}{2} \left(1 + \frac{n_2}{n_1} \right) - i \frac{\omega}{2c_0 n_1} \chi_{2D}(\omega) \right|^2}. \quad (7.12)$$

with the speed of light c_0 in vacuum and the two-dimensional optical susceptibility $\chi_{2D}(\omega)$ discussed in the previous section which describing the linear response of the TMD monolayer to an optical pulse, c.f.7.9.

We can now solve Eq.7.12 and calculate the homogeneous absorption spectrum from which we can directly read of the radiative dephasing in form of the FWHM of the excitonic absorption peak. Not that, the in Eq.7.12 introduce phenomenological scattering constant γ can now be

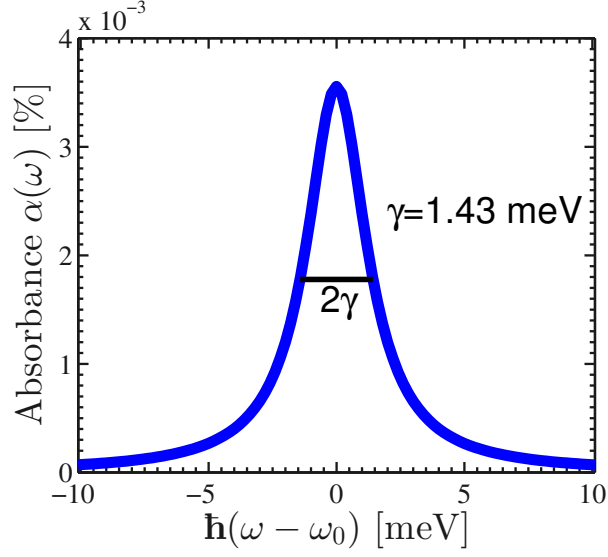


Figure 7.6: Excitonic frequency-dependent homogeneous absorbance of WSe₂ exhibiting the delocalized A exciton. Our calculation reveal a lower limit for the homogeneous linewidth of γ 1.48 meV (0.23 ps) due to a strong radiative coupling.

reduced to a small value, where it does not influence the result of Eq.7.12. We find that the results converge and have no influence on the calculated radiative life time with $\gamma < 10^{-4}$ meV. As discussed in the previous sections the optical susceptibility is determined by the excitonic eigenfunctions and the optical matrix element and the eigenvalues determined by the Wannier equation.

Figure 7.6 shows the absorbance $\alpha(\omega)$ focusing on the A exciton. Our calculations reveal a homogeneous linewidth of 1.43 meV corresponding to a radiative lifetime of 230 fs. This value is consistent with the measurements and provides a lower bound on the exciton radiative lifetime [69, 93].

The calculated radiative coupling depends on the refractive index of the surrounding n_s , the strength of the excitonic absorption, and the intrinsic material parameters, such as the effective mass. The calculation has been performed for monolayer MoSe₂ grown on sapphire substrate ($n_1 = 1.75$, $n_2=1$ corresponding to air). We find that the higher the refractive index n_1 resulting in a more efficient screening of the Coulomb interaction, the longer is the radiative lifetime. In figure 7.7, the radiative linewidth of the four most prominent TMDs materials including WSe₂, WS₂, MoS₂, and MoSe₂ is shown as a function of the dielectric environment. The strongest Coulomb interaction can be found for the free standing TMDs. In this case, we find a linewidth of 3.6 meV for WSe₂ corresponding to a radiative lifetime of about 160 fs. Fur-

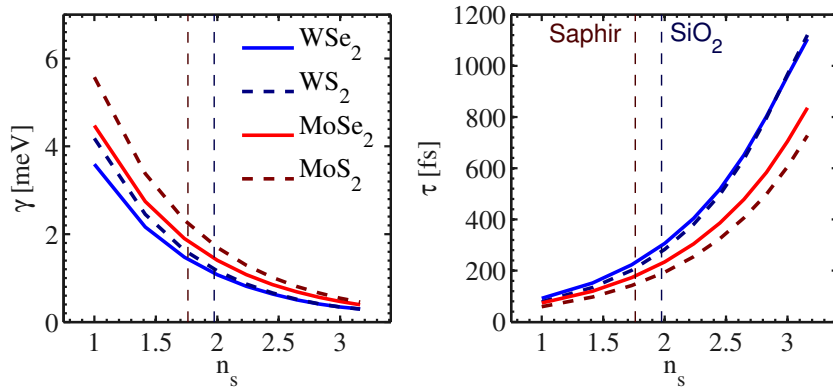


Figure 7.7: Homogeneous broadening left and radiative lifetime right of WSe₂, WS₂, MoS₂, and MoSe₂ in dependence of the dielectric environment. n_s gives the substrates refractive index. The larger n_s the smaller is the coulomb interaction and the larger is the homogeneous broadening and the shorter the radiative life time. The fastest TMD is MoS₂, the slowest WSe₂.

thermore, the excitonic oscillator strength is given by $\theta_{\nu_s\xi}$ that contains both the optical matrix element and the excitonic wave function, c.f.7.10. The strength of the carrier-light interaction has been adjusted to the experimentally measured absorption of 10% at the A exciton for all TMDs. Assuming double absorption intensity of 20%, we obtain a radiative linewidth of 2.85 meV, i.e. the more efficient the absorption, the larger is the radiative broadening and the shorter is the radiative life time. Finally, our calculations show that TMD monolayers with a higher effective mass (entering the excitonic wave function) exhibit a stronger radiative coupling. This can be seen in figure 7.7, where the members of the molybdenum family having a higher effective mass [78], exhibit a stronger coupling. This can be traced back to an enhanced excitonic wave function for heavier holes and electrons. Another important factor is the spectral position of the excitonic resonance, which enters into the equation via the excitation frequency ω . The higher ω , the shorter is the radiative lifetime. Considering all mentioned dependencies, our calculations reveal the shortest radiative lifetime of approximately 100 fs for MoS₂ in the free-standing case, cf. figure 7.7.

We can now also discuss higher excitonic transitions, where in particular the excitonic wave function leads to a smaller coupling to the light field. As can be seen in Fig.7.8 the radiative life time of higher excitonic transition is longer due to the smaller occupation probability of higher energy states. Nevertheless, we again see the difference to quantum well systems, in analogy to the earlier section where we found a non-Rydberg series of the excitonic state, we again find that the difference between the radiative life time of the lowest to the second lowest excitonic state is smaller in TMDs than in the conventional systems, e.g in ref. [44] the homogeneous line

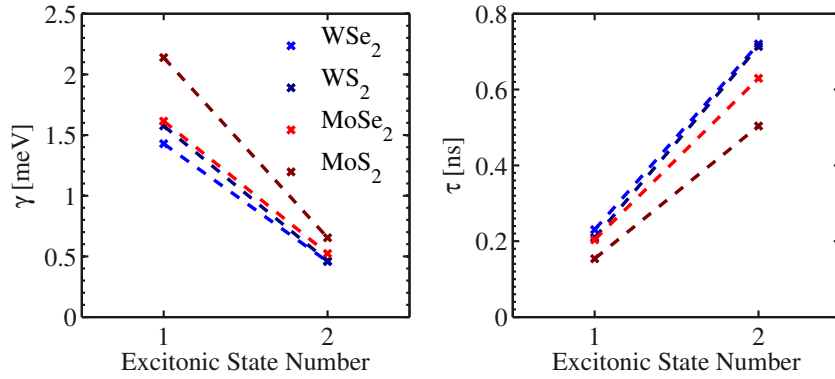


Figure 7.8: Homogeneous branding left and radiative lifetime right of WSe₂, WS₂, MoSe₂, and MoS₂ for the lowest and second lowest excitonic state. The larger radiative life time reflects the smaller coupling of higher excitonic transitions to the light field. This can be traced back to the excitonic wave function. Which is a measure for the occupation probability of the exciton in an higher state.

width of the second excitonic transition is about 10% of the first, here we find approximately 40%. The coupling of higher excitonic states to the lightfield is considerably stronger in TMD materials than in quantum wells or quantum wires.

While the inhomogeneous line width is in the range of tens of meV the homogeneous linewidth is considerably narrower and promises a much longer life time of coherent quantities like the microscopic polarization, c.f. 7.1. This is a very important point for the next section where we discuss intervalley coupling of the microscopic and macroscopic polarization.

CHAPTER 8

COULOMB-INDUCED INTERVALLEY COUPLING

In the previous section 7.1.2 we have introduced the Wannier Equation (Eq.7.5) for uncoupled systems. The solution for this equation can also be used within the valley coupled regime. The idea is to treat the valley coupling terms, all terms with $\xi \neq \xi'$ in Eq.7.1, as inhomogeneities and solve the Wannier equation for both valleys K and K' separately. With the gained eigen values and eigen functions one can than transform Eq.7.1 into the excitonic basis.

The valley coherence is meaningful for resonant states, e.g. energetically degenerated states in K and K'. On the Hatree Fock level without momentum of the exciton there is no coupling between different spin bands. We can there for reduce our notation to ξ only, the analyses are valid within one spin band.

The following calculations are valid for two-dimensional semiconductors with a hexagonal lattice structure and with a small spin-orbit coupling. Principally, the investigations are also applicable to TMDs, however due to the large spectral separation of A and B excitons (with the same spin orientation), the discussed coupling effects are very small. In the following section, we first assume a vanishingly small spin-orbit coupling, as found e.g. in silicene or germanene [zitat]. Then, we discuss the impact of the spin-orbit coupling on the intrinsic Coulomb-induced inter-valley coupling that is crucial in TMDs.

We now restrict our analysis to one excitonic transition ν . This is possible due to the spectrally well separated transitions in strongly coupled two dimensional materials, c.f. section 7.1.4. In the excitonic basis the equation of motion 7.1 for one excitonic transition ν reads,

$$i\dot{p}_\xi^\nu = (\omega_\xi^\nu - i\gamma)p_\xi^\nu - p_{\xi'}^\nu C_{\xi\xi'} - L_\xi^\nu(t). \quad (8.1)$$

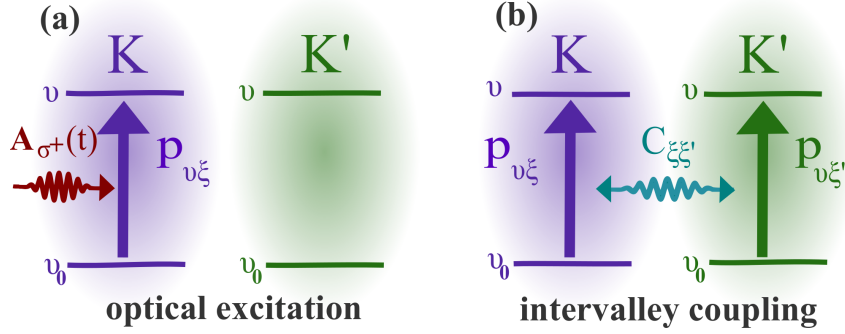


Figure 8.1: (a) Schematic illustration of the valley-selective optical excitation with circularly polarized light $A_{\sigma_+}(t)$ introducing a microscopic polarization $p_{\nu\xi}$ and between the excitonic ground state ν_0 and the excited state ν in the K-valley denoted by ξ . (b) Coulomb-induced intervalley coupling described by $C_{\xi\xi'}$ induces a microscopic polarization $p_{\nu\xi'}$ also in the unexcited K' valley.

Here $\omega_\xi^\nu = E_\xi^\nu/\hbar$ is the frequency of the excitonic state ν . It is given by the renormalized band gap and the excitonic binding energies. The rabi frequency of the excitonic transition reads,

$$L_\xi^\nu(t) = \frac{1}{\hbar} \sum_{\mathbf{k}} \theta_{\nu,\xi}^L(\mathbf{k}) \mathbf{M}_{\mathbf{k}\xi}^{\lambda\lambda'} \cdot \mathbf{A}(t) \quad (8.2)$$

it is the scalar product of optical matrix element $\mathbf{M}_{\mathbf{k}\xi}^{\lambda\lambda'}$ and the vector potential of the incident light $\mathbf{A}(t)$ which include the optical selection rules of circularly polarized light for hexagonal semiconductors with broken inversion symmetry, e.g. right (left) handed polarized light is absorbed by carriers occupying the $\mathbf{K}^{(\prime)}$ point [12, 5], weighted by the excitonic wave functions. Furthermore, we use the recently calculated homogeneous broadening $\hbar\gamma \approx 1.45$ meV, see section 7.2. The coupling to the other valley appears through the second term on the right hand side of the equation, a product of the excitonic transition of the other valley and the coupling constant,

$$\hbar C_{\xi\xi'}^{\nu\nu'} = \sum_{\mathbf{k}, \mathbf{k}'} \theta_{\nu\xi}^R(\mathbf{k}) \theta_{\nu'\xi'}^L(\mathbf{k}') V_{\mathbf{k}\mathbf{k}', \xi\xi'}^{eh}. \quad (8.3)$$

This constant stems from the excitonic term in the semiconductor Bloch equation and accounts for the intervalley correlation between excitonic states in K and K'. It is a measure for the scattering possibility of two carriers in opposite valleys.

Though the distance between K and K' valley is large in k space the intervalley coulomb matrix

element,

$$V_{\mathbf{k}\mathbf{k}',\xi\xi'}^{eh} = \frac{\Gamma_{\mathbf{k},\mathbf{k}',\xi\xi'}^{eh}}{\epsilon_0\epsilon_s} \frac{1}{|\mathbf{q} + \Delta_{\xi\xi'}|(1 + r_0|\mathbf{q} + \Delta_{\xi\xi'}|)}, \quad (8.4)$$

is non vanishing. The quantity $\Delta_{\xi\xi'} = \mathbf{K}^\xi - \mathbf{K}^{\xi'}$ is the valley distance and $\Gamma_{\mathbf{k},\mathbf{k}',\xi\xi'}^{eh}$ the tight binding coefficient functions[5]. Furthermore, ϵ_0 is the vacuum permittivity, and ϵ_s the dielectric constant of the surrounding media and $r_0 = d\epsilon_\perp/\epsilon_s$ the screening length.[39, 19, 7, 5]

Transforming Eq.8.1 into Fourier space we find analytic solutions for the excitonic polarizations of the excited valley ($L_\xi^\nu(\omega) \neq 0$)

$$p_{\xi'}^\nu(\omega) = \frac{p_{\xi'}^\nu(\omega)C_{\xi\xi'}^{\nu\nu} + L_{\xi s}^\lambda(\omega)}{E_{\nu\xi} - \hbar\omega - i\gamma} \quad (8.5)$$

and consequently the indirectly excited valley ($L_{\xi'}^\nu(\omega) = 0$) as,

$$p_{\xi'}^\nu = \frac{L_\xi^\nu(\omega)C_{\xi\xi'}^{\nu\nu}}{(E_{\nu\xi} - \hbar\omega - i\gamma)(E_{\nu\xi'} - \hbar\omega - i\gamma) - C_{\xi\xi'}^2}. \quad (8.6)$$

Not that, the difference between equation 8.5 and 8.6 solely can be traced back to the circular dichroism. If both valleys would be excited via the external light field we would derive equations 8.5 for both valleys.

We now analyse the effect on the current which can be written as the sum over the different valleys $j^{\sigma\pm}(\omega) =_{\xi \neq \xi'} j_\xi^{\sigma\pm}(\omega) + j_{\xi'}^{\sigma\pm}(\omega)$ these contributions are given by,

$$j_{\xi^{(\nu)\sigma\pm}}(\omega) = \sum_{\mathbf{k}\nu} M_{\xi^{(\nu)\sigma\pm}}^{c\nu} \theta_{\nu\xi^{(\nu)}}(\mathbf{k}) p_{\xi^{(\nu)}}^\nu(\omega) \quad (8.7)$$

Note that we select the right and left handed contributions of the polarization. For right (left) handed polarized light and for ξ at the K and ξ' at the K' point we find since $M_{\xi^{(\nu)\sigma_{(+)-}}}^{c\nu} = 0$ (see Fig. 6.4) that $j_{\xi^{(\nu)\sigma_{(+)-}}(\omega)} = 0$. Though the microscopic polarizations are coupled, the excitation with polarized light leads to a build up of the current in only one of the two valleys.

Using the results of both equations (Eq.8.5 and Eq. 8.6) we can now formulate the Elliot formula using the relation

$$\chi^{\sigma\pm}(\omega) = \frac{c}{\omega^2} \frac{j_{\sigma\pm}(\omega)}{A_{\sigma\pm}(\omega)} \quad (8.8)$$

for we find the susceptibility for right handed polarized light (A_{σ_+}) of excitonic state ν in valley

coupled system as,

$$\begin{aligned}\chi_{\sigma_+}^{\nu}(\omega) &= \frac{j_{\xi}^{\sigma_+}(\omega) + j_{\xi'}^{\sigma_+}(\omega)}{A_{\sigma_+}(\omega)} \\ &\stackrel{j_{\xi'}^{\sigma_+}(\omega)=0}{=} \frac{1}{\epsilon\epsilon_0} \frac{\Theta_{\nu\xi}}{E_{\nu\xi} - \hbar\omega - i\gamma - \frac{[C_{\xi\xi'}^{\nu\nu}]^2}{E_{\nu\xi'} - \hbar\omega - i\gamma}},\end{aligned}\quad (8.9)$$

that explicitly includes the Coulomb-induced intervalley coupling entering via $C_{\xi\xi'}^{\nu\nu}$ and the excitonic wave function weighted by the optical matrix element Eq.7.10. We consider the general case taking into account off-resonant states in the K and K' valley, i.e. $E_{\nu\xi'} \neq E_{\nu\xi}$. This will be important for the discussion on the impact of detuning of the valleys on the intervalley coupling. Note however, that for resonant excitation of one valley $\hbar\omega = E_{\nu\xi}$, the coupling term $\frac{[C_{\xi\xi'}^{\nu\nu}]^2}{E_{\nu\xi'} - \hbar\omega - i\gamma}$ is anti proportional to the energy difference $E_{\nu\xi} - E_{\nu\xi'}$ between the states. For growing difference of the states $E_{\nu\xi} - E_{\nu\xi'} \rightarrow \infty$ we find

$$\frac{[C_{\xi\xi'}^{\nu\nu}]^2}{E_{\nu\xi'} - \hbar\omega - i\gamma} \rightarrow 0,$$

resulting in the uncoupled equation 7.9 of section 7.1.2. This shows that the intervalley coupling is not meaningful for strongly off-resonant states in K and K' valley and gives in contrast to resent experiments hope for Spin-Valleytronics in TMDs. Where the states of different valleys are highly of resonant due to the strong spin orbit coupling.

We now use $E_{\nu\xi'} \rightarrow E_{\nu\xi^{(l)}}$ the index l and l' to account for the defects in the system, e.g. the inhomogeneous broadening of the absorption spectrum. The inhomogeneous broadening of the absorption [69] indicates a Gaussian distribution of defects in a TMD sample, which consequently leads to a Gaussian distribution of excitonic eigenstates. For each of these state l in one valley and l' in the other we find the susceptibility $\chi^{\nu}(\omega) = \chi_{l,l'}^{\nu}(\omega)$. Weighted by the Gaussian distribution the integral over $\chi_{l,l'}^{\nu}(\omega)$ over the states l and l' gives us $\bar{\chi}(\omega)$ and we find the inhomogeneously broadened absorption $\alpha(\omega) \propto \omega \text{Im}[\bar{\chi}(\omega)]$.

Now, we have all ingredients to study the direct impact of Coulomb-induced intervalley coupling on the excitonic absorption. The excitonic resonances are given by the denominator of the imaginary part of the susceptibility in Eq. (8.9). For $\gamma \rightarrow 0$, we find the resonances for the state ν at

$$\hbar\omega_{\pm} = \frac{1}{2}(E_{\xi}^{\nu,l} + E_{\xi'}^{\nu,l'} \pm \sqrt{[2\hbar C_{\xi\xi'}^{\nu\nu}]^2 + (E_{\xi}^{\nu,l} - E_{\xi'}^{\nu,l'})^2}).\quad (8.10)$$

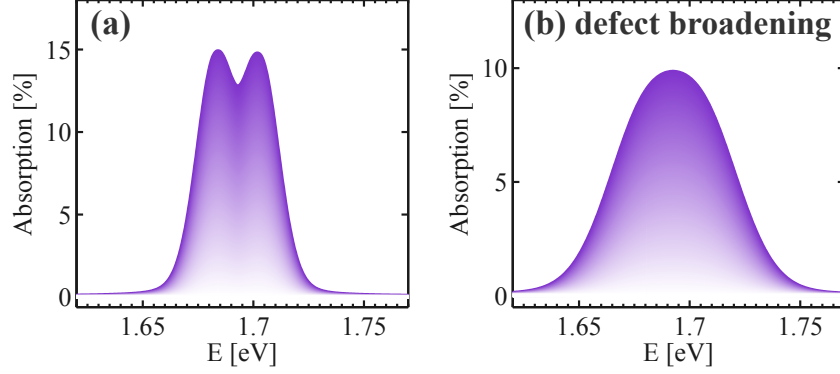


Figure 8.2: (a) The excitonic absorption spectrum of a valley coupled two dimensional semiconductor exhibits a pronounced splitting due to the intervalley interaction coupling the resonant states in K and K' valleys. (b) Assuming a defect-induced inhomogeneous broadening of 20 meV (that is twice large than in (a)) the splitting of the excitonic transition cannot be resolved any more, however, the intervalley coupling is reflected by the broadened peak.

The intervalley coupling gives rise to two solutions ω^\pm resulting in an peak splitting of excitonic transitions. In the case of degenerated states at the K and the K' valley, i.e. $E_{\nu\xi'}^l = E_{\nu\xi}^l$, the splitting reads $\Delta E = \hbar(\omega^+ - \omega^-) = 2C_{\xi\xi'}$. Note that a detuning of the degenerate valley states can be introduced in an electric or magnetic field or even after an optical excitation [49, 52, 83]. We first discuss energetically degenerate states and then include the effect of detuning on the linear absorption spectrum.

8.1 ABSORPTION COEFFICIENT OF VALLEY COUPLED TWO DIMENSIONAL SEMICONDUCTORS

In the previous section we could show that the intervalley coupling leads to a splitting of the excitonic resonances in the absorption spectrum. Whether or not it is visible in experiments or has a considerable influence on intrinsic system properties which are meaning full especially in terms of valleytronics will be discussed in this section. With a screening length of $r_0 = 1$ nm, we obtain a peak splitting of $\Delta E = 17$ meV, cf. Fig. 8.2(c).

Note that although the optical excitation of one valley via circularly polarized light also induces a microscopic polarization at the other unexcited valley, its optical response remains zero, since the optical matrix element is zero resulting in $L_{\nu\xi}(\omega) = 0$. The macroscopic polarization of one valley is the sum over all microscopic polarizations weighted by the $L_{\nu\xi}(\omega)$. Therefore

only terms with $L_{\nu\xi}(\omega) \neq 0$ contribute to $\chi_{\nu}(\omega) = 0$, cf. Eq. (8.9). However, the indirectly induced microscopic polarization leads to a pronounced peak splitting in optical spectra. This is measurable in experiments as long as the inhomogeneous broadening does not surpass the splitting. Assuming a larger defect-induced broadening of 20 meV, the effect of intervalley coupling is not reflected any more by a peak splitting, however it is visible by a broadened excitonic transition, cf. Fig. 8.2(b).

The coherent coupling of the two valleys can be seen as an obstacle in terms of valleytronic devices, where one aims to exploit the valley degree of freedom. It is important to control or suppress the intervalley coupling in order to exploit the valley quantum number for valleytronic devices. Note however that this is not an obstacle for TMD based valleytronics where the spin orbit coupling is large enough to suppress the coupling.

8.2 DETUNED VALLEYS AND THE TRANSITION TO TMDs INCLUDING SPIN ORBIT COUPLING

So far we have considered energetically resonant states in K and K' valley. For the large group of TMDs this is not a realistic situation, where a large spin orbit coupling detunes the excitonic states of the same spin in K and K' valleys. We will here show that the spin orbit coupling in analogy to the detuning strongly suppresses the coupling such that it is not meaning full within linear optics for TMDs. In an experiment where one valley is selectively excited via circularly polarized light this might not be the case. For the arbitrary two dimensional semiconductor without spin orbit coupling this study is also meaning full. A valley polarized state, where carriers are not homogeneously distributed between the valleys, lead to a asymmetric renormalization of the bandstructure as well as the excitonic binding energy and consequently detune the valleys. One could argue that every spectral experiment using circularly polarized light leads to a detuning of the valleys Another example is the lifting of valley degeneracy in a magnetic (Zeeman effect) or an electric field (Stark effect)

In Fig.8.3, we show the excitonic absorption spectra for a detuning of ± 5 meV in an arbitrary semiconductor. We investigate the impact of the Coulomb-induced intervalley coupling after optical excitation with right and left circularly polarized light at a low and a high initial doping, respectively. We observe a splitting of the excitonic transition only in the case of small doping, where the screening is still weak enough. Generally, the detuning gives rise to a pronounced asymmetry of the two peaks and to an overall red- or blue-shift of the spectrum that directly reflects the detuning of the excited valley, cf. Fig. 8.3.

In the high doping regime, the splitting of the excitonic transition cannot be resolved due

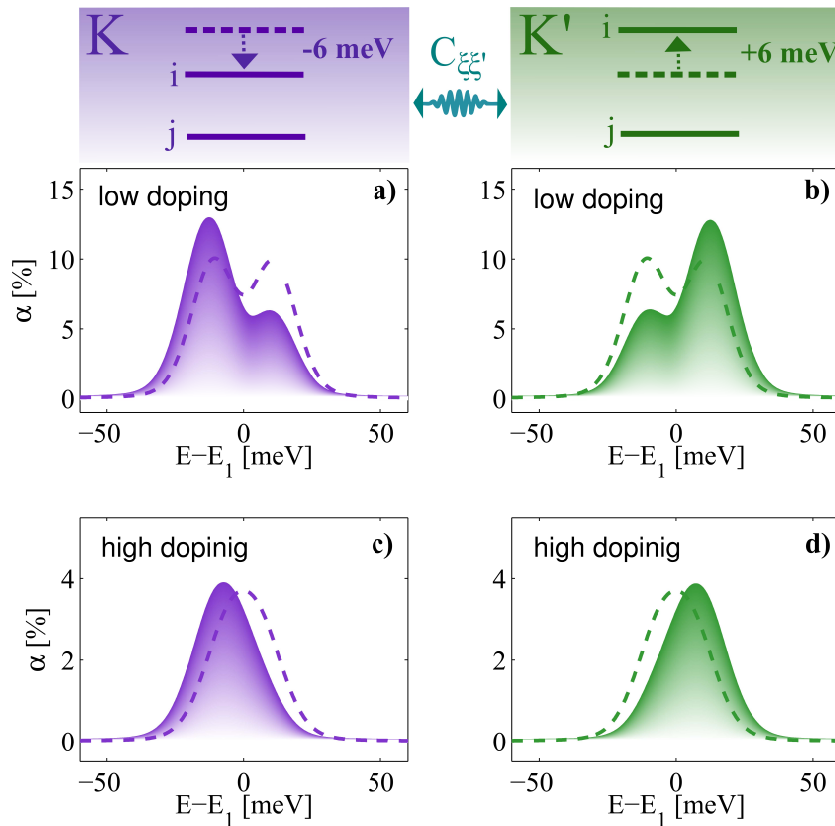


Figure 8.3: Absorption Spectra of an arbitrary two dimensional semiconductor without spin-orbit coupling for detuned valleys ($K^{(l)}$ -valley detuned by $(-)$ 5 meV). a)+b) Low doping regime: A detuning of the eigenvalues of the valleys leads to a asymmetric splitting of the absorption peak. c)+d) High doping regime: The detuning of the eigenvalues leads to a shift of the absorption spectrum. The strong plasma-screening reduces the intervalley coupling such that one only observe a shift of the absorption spectrum in agreement with the detuning.

to the strong screening. Here, we mainly find a shift of the broadened resonance and a slight asymmetry of the absorption peak at the energetically lower or higher side. The asymmetry in both cases can be traced back to the effect of homogeneous and inhomogeneous broadening on the detuned valley absorption. For the homogeneously broadened solutions ω^\pm of Eq.8.10 the solutions closer to the $E_{\nu\xi}$ state of the excited valley are wider. In combination with the inhomogeneous broadening, which favours resonant transition, this leads to a overall shift of the absorption intensity in direction of the detuning of the excited valley.

The discussed intervalley coupling is only present within bands with the same spin, since the coupling occurs due to the Hartree Fock terms which do not couple electrons of different spins in a homogeneous system. With detuning of the states of different valleys (e.g. due to strong spin orbit coupling as is the case in TMDs) the discussed intervalley coherence is strongly

suppressed.

8.3 COULOMB INDUCED INTERVALLEY COUPLING IN NON-LINEAR OPTICS

In this section we discuss non linear effects in valley coupled two dimensional materials. We consider the coupling within one spin system. We will first consider an arbitrary two dimensional semiconductor without spin orbit coupling and then calculate the intervalley coupling between A and B exciton of for real TMD structures in the next chapter.

We discuss the optical excitation of carriers in the valley coupled regime and do not discuss the relaxation mechanism by including higher order scattering terms in the equations.

8.4 MICROSCOPIC APPROACH

In this section we will include the full set of semiconductor Bloch equations introduced in Section 6.2, which in particular includes a coupling between the time dependent carrier dynamics ($\dot{f}_\xi^{e,h}$) and the microscopic polarization (\dot{p}_ξ) dynamics. We will further show the transformation of the full set of equation into the excitonic basis and compare the full electron hole picture and the excitonic picture.

8.4.1 ELECTRON-HOLE-PICTURE

So far we have restricted our analyses to linear optics, where we have assumed that the external perturbation via the potential $\mathbf{A}(t)$ is small such that we can use $\dot{f}_\xi^{e,h} = 0$. In this section we will show how the microscopic quantities interact within the TMD materials in the non linear regime where $\dot{f}_\xi^{e,h} \neq 0$, and Eq.8.11 and Eq.8.12 form a set of coupled equations.

We will again focus on the low energy regime of the TMDs. Within the non-linear regime Eq.6.21 and Eq. 6.22 transform to,

$$\dot{p}_{\mathbf{k}\xi} = -i\tilde{\omega}_{\mathbf{k}\xi}p_{\mathbf{k}\xi} - i(1 - f_{\mathbf{k}\xi}^h - f_{\mathbf{k}\xi}^e)\tilde{\Omega}_{\mathbf{k}\xi} \quad (8.11)$$

$$\dot{f}_{\mathbf{k}\xi}^\lambda = 2\text{Im} \left[p_{\mathbf{k}\xi}\tilde{\Omega}_{\mathbf{k}\xi}^* \right]. \quad (8.12)$$

We can now separate the different valley contributions. And find the valley dependent renor-

malization of the band gap,

$$\hbar\tilde{\omega}_{\mathbf{k},\xi} = \Delta\varepsilon_{\mathbf{k},\xi} - \sum_{\mathbf{k}'\xi'} \left[f_{\mathbf{k}\xi'}^e V_{\mathbf{k},\mathbf{k}',\xi,\xi'}^{cc} + f_{\mathbf{k}\xi'}^h V_{\mathbf{k},\mathbf{k}',\xi,\xi'}^{vv} \right] \quad (8.13)$$

and to the renormalization of the Rabi frequency $\Omega_{\mathbf{k}\xi} = \mathbf{M}_{\mathbf{k}\xi}^{vc} \cdot \mathbf{A}$ resulting in

$$\hbar\tilde{\Omega}_{\mathbf{k}\xi} = \Omega_{\mathbf{k}} - \sum_{\mathbf{k}'\xi'} V_{\mathbf{k},\mathbf{k}',\xi,\xi'}^{cv} p_{\mathbf{k}'\xi'}. \quad (8.14)$$

In contrast to conventional semiconductors where the optically active region is to be found at the Γ -point the equations above show a coupling between two optically active regions in the Brillouin zone, the K and K' valleys.

The total amount of optically excited carriers is given by,

$$\begin{aligned} N &= \sum_{\mathbf{k},\xi} f_{\mathbf{k},\xi}^{e,h} = 2\text{Im} \left[\sum_{\mathbf{k},\xi} p_{\mathbf{k}\xi} \tilde{\Omega}_{\mathbf{k}\xi}^* \right] \\ &= 2\text{Im} \left[\sum_{\mathbf{k},\xi} p_{\mathbf{k}\xi} \Omega_{\mathbf{k}}^* - \underbrace{\sum_{\mathbf{k}'\xi',\mathbf{k},\xi} V_{\mathbf{k},\mathbf{k}',\xi,\xi'}^{cv} p_{\mathbf{k}\xi} p_{\mathbf{k}'\xi'}^*}_{\in \Re} \right] \end{aligned} \quad (8.15)$$

Since $\text{Im}[\sum_{\mathbf{k}'\xi',\mathbf{k},\xi} V_{\mathbf{k},\mathbf{k}',\xi,\xi'}^{cv} p_{\mathbf{k}\xi} p_{\mathbf{k}'\xi'}^*] = 0$ the total amount of excited carriers is solely given by the first term ($\sum_{\mathbf{k},\xi} p_{\mathbf{k}\xi} \Omega_{\mathbf{k}}^*$) in Eq.8.15. The carriers are optically excited by the external potential $\mathbf{A}(t)$. The second term does not contribute to the amount of carriers excited. However, it leads to a redistribution of carriers as one can see if we split N into the different valley contributions $N = \sum_{\xi \neq \xi'} N_{\xi} + N_{\xi'}$. The Carriers of the excited valley reads,

$$N_{\xi} = \sum_{\mathbf{k}} f_{\mathbf{k},\xi}^{e,h} = 2\text{Im} \left[\sum_{\mathbf{k}} p_{\mathbf{k}\xi} \Omega_{\mathbf{k},\xi}^* - \underbrace{\sum_{\mathbf{k}'\xi'=\xi,\mathbf{k},\xi} V_{\mathbf{k},\mathbf{k}',\xi,\xi'}^{cv} p_{\mathbf{k}\xi} p_{\mathbf{k}'\xi'}^*}_{\in \Re} + \underbrace{\sum_{\mathbf{k}'\xi' \neq \xi,\mathbf{k},\xi} V_{\mathbf{k},\mathbf{k}',\xi,\xi'}^{cv} p_{\mathbf{k}\xi} p_{\mathbf{k}'\xi'}^*}_{\in \mathbb{C}} \right]. \quad (8.16)$$

The last term leads to a redistribution of carriers via the indirectly induced microscopic polarization $p_{\mathbf{k}'\xi'}^*$. The different coupling to the circularly polarized light leads to different phases and time evolutions of the microscopic quantity and hence we find that $p_{\mathbf{k}\xi} \neq_{\xi' \neq \xi} p_{\mathbf{k}'\xi'}$. Therefore, the term leads to a coherent redistribution of carriers between the valleys, however it does not

influence the total amount of optically excited carriers. For the unexcited valley where $\Omega_{\mathbf{k},\xi}^* = 0$, this is the only contribution which reads,

$$N_{\xi'} = \sum_{\mathbf{k}} f_{\mathbf{k},\xi}^{e,h} = 2\text{Im} \left[\underbrace{\sum_{\mathbf{k}' \neq \xi, \mathbf{k}, \xi} V_{\mathbf{k},\mathbf{k}',\xi,\xi'}^{cv} p_{\mathbf{k}\xi} p_{\mathbf{k}'\xi'}^*}_{\in \mathbb{C}} \right]. \quad (8.17)$$

Here, we could show that, the Coulomb-induced intervalley coupling leads a redistribution of carriers during the lifetime of the microscopic polarization. In the next section we will discuss the formulation of the equations within the excitonic basis and calculate the optically induced valley-polarization.

8.4.2 EXCITONIC BASIS

Here we will discuss the carrier excitation process within the excitonic basis. In the non-linear regime where we want to include the time evolution of the carrier distributions (Eq.7.2) we can not use in the previous chapter introduced left and right handed eigenfunctions. For they are defined via the phase space filling factor $(1 - f_{\xi,\mathbf{k}}^h - f_{\xi,\mathbf{k}}^e)$ which is now coupled to the polarization. In order to include the dynamics of all carrier contributions we formulate the Wannier equation by firstly treating all carrier contributions as inhomogeneities,

$$\epsilon_{\mathbf{k},\xi} \theta_{\nu\xi}(\mathbf{k}) - \sum_{\mathbf{k}'} V_{\mathbf{k},\mathbf{k}',\mathbf{q}}^{exc} \theta_{\nu\xi}(\mathbf{k}') = E_{\nu\xi} \theta_{\nu\xi}(\mathbf{k}). \quad (8.18)$$

After solving this equation we can transform Eq.8.11 into the excitonic basis using,

$$p_{\mathbf{k}\xi} = \sum_{\nu} p_{\nu\xi} \theta_{\nu\xi}(\mathbf{k}) \quad (8.19)$$

and

$$p_{\nu\xi} = \sum_{\mathbf{k}} p_{\mathbf{k}\xi} \theta_{\nu\xi}^*(\mathbf{k}). \quad (8.20)$$

Due to the coupling of coherent and incoherent quantities we also transform the carrier densities into the new basis via,

$$f_{\mathbf{k}\xi}^{\lambda} = \sum_{\nu} f_{\nu\xi}^{\lambda} \theta_{\nu\xi}(\mathbf{k}) \quad (8.21)$$

and

$$f_{\nu\xi}^\lambda = \sum_{\mathbf{k}} f_{\mathbf{k}\xi}^\lambda \theta_{\nu\xi}^*(\mathbf{k}). \quad (8.22)$$

Using Eq.8.18-8.22 we can formulate the Bloch equations (Eq.8.12 and Eq.8.11) in the excitonic basis and find,

$$\begin{aligned} i\hbar\dot{p}_\xi^\nu &= \left(E_{\nu\xi} - \sum_{\xi'} \left(f_{\xi'}^{e,\nu} \Gamma_{\xi\xi'}^{\nu,e} + f_{\xi'}^{h,\nu} \Gamma_{\xi\xi'}^{\nu,h} \right) \right) p_\xi^\nu - L_\xi^\nu(t) \\ &- \left(f_\xi^{e,\nu} + f_\xi^{h,\nu} \right) \left(\bar{L}_\xi^\nu(t) + \sum_{\xi'} p_{\xi'}^\nu \bar{C}_{\xi\xi'}^{\nu\nu} \right) - p_{\xi' \neq \xi}^\nu C_{\xi\xi' \neq \xi}^{\nu\nu}. \end{aligned} \quad (8.23)$$

and

$$f_{\nu\xi}^{h/e} = \frac{2}{\hbar} \text{Im} \left[p_\xi^\nu \left(L_\xi^{\nu*}(t) - \sum_{\xi} p_{\xi'}^{\nu*} \bar{C}_{\xi\xi'}^{\nu\nu} \right) \right]. \quad (8.24)$$

Here we have restricted our set of basis functions to one excitonic state ν . The quantity $C_{\xi\xi'}^{\nu\nu}$ accounts for the coulomb induced intervalley coupling and has been introduced in the previous chapter Eq.8.3. Furthermore, we have introduced the following abbreviations,

$$\bar{C}_{\xi\xi'}^{\nu\nu} = \sum_{\mathbf{k}, \mathbf{k}'} |\theta_{\nu\xi}(\mathbf{k})|^2 \theta_{\nu\xi'}(\mathbf{k}') V_{\mathbf{k}\mathbf{k}', \xi\xi'}^{eh} \quad (8.25)$$

which accounts for the renormalization of the rabi frequency via the attractive electron-hole interaction and includes a third wave excitonic wave function stemming from the carrier phase space filling factor. Note that, the quantity $C_{\xi\xi'}^{\nu\nu}$ contains two wave functions. Also included is the carrier induced band gap renormalization via,

$$\Gamma_{\xi\xi'}^{\nu,e/h} = \sum_{\mathbf{k}, \mathbf{k}'} |\theta_{\nu\xi}(\mathbf{k})|^2 \theta_{\nu\xi'}(\mathbf{k}') V_{\mathbf{k}\mathbf{k}', \xi\xi'}^{hh/ee}. \quad (8.26)$$

It accounts for inter ($\xi' \neq \xi$) and intra ($\xi' = \xi$) valley band gap renormalizations. Furthermore, the light matter interaction is reduced via the Pauli blocking term weighted by the carrier light

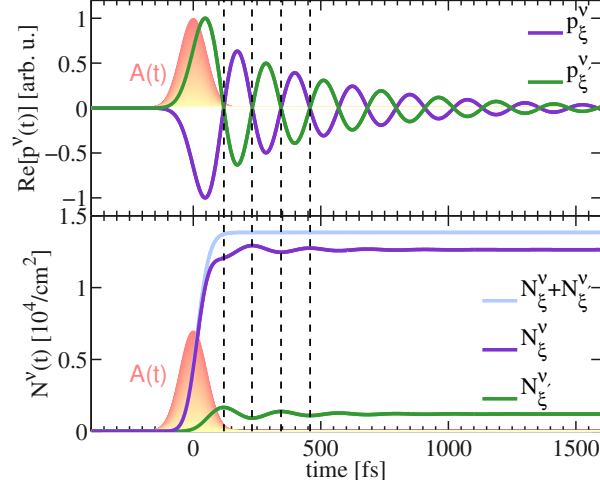


Figure 8.4: Carrier excitation in valley coupled two dimensional semiconductor for resonant states in opposite valleys. (a) Microscopic polarization of the optically excited valley (purple line) and the Coulomb induced polarization in the unexcited valley (green line). The oscillation between the two polarizations is given by the intervalley Coulomb-coupling element $C_{\xi\xi'}^{\nu\nu}$. (b) Total amount of optically excited carriers (blue line) and the single valley contributions of the optically excited valley (purple with 91.3% of excited carriers) and the indirectly excited carriers (green 8.7% of excited carriers). The optically excited carriers are redistributed via the coherent microscopic polarization. The oscillation between the carriers and the polarizations of opposite valleys are in phase.

interaction,

$$\bar{L}_\xi^\nu(t) = \sum_{\mathbf{k}} |\theta_{\nu\xi}(\mathbf{k})|^2 \mathbf{M}_{\mathbf{k}\xi}^{\lambda\lambda'} \cdot \mathbf{A}(t). \quad (8.27)$$

The great advantage of this solution is that it is numerically not demanding and gives a more intuitive solution. However, as we have reduced the analyses to one excitonic state it does not include all carrier contributions and is therefore only valid in the lower excitation regime, where one can reduce the analyse to one excitonic state. The total carriers generated by a weak ($1\mu\text{J}/\text{cm}^2$) and short pulse (FWHM=50fs) are plotted in Fig.8.4 (b).

Above in Fig.8.4 (a) the microscopic polarizations of the two valleys within the excitonic basis are plotted.

Here the oscillations of $\cos(t * E^\nu / \hbar)$ have been eliminated from the plot. The still present oscillations of the real part of the microscopic polarization reflect the oscillations between the valleys and are proportional to $C_{\xi\xi' \neq \xi}^{\nu\nu}$. The oscillation between the valleys is also present in the total carriers of one valley. While the total amount of carriers excited (the sum over total carriers excited in both valleys) by the light pulse shows no oscillation, the contribution of each

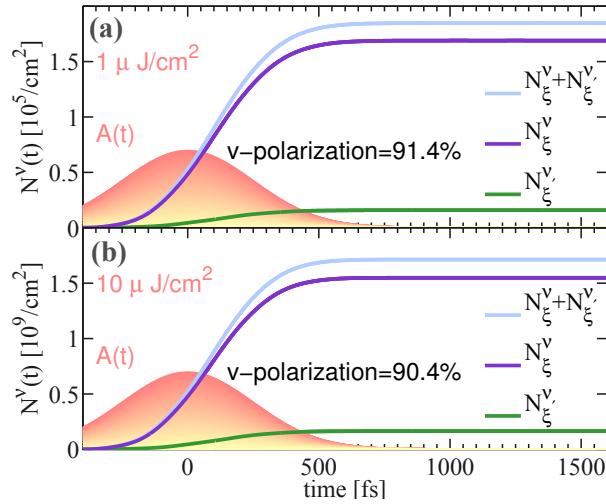


Figure 8.5: Excitation of an exemplary two dimensional semiconductor with different intensities and a long pulse of a FWHM=250fs. The in Fig.8.4 found oscillations due to the coherent quantities is not visible. (a) a pulse of $1 \mu\text{J}/\text{cm}^2$ leads to a valley polarization of 91.4%. In (b) more carriers are excited into the system, resulting in slightly less valley polarized state with 90.4% of valley polarization.

valley oscillates with the real part of the microscopic polarization. These oscillations vanish in time due to the radiative decay of the polarization.

During the pulse the oscillations in the carrier contributions are not present, since the polarizations are still driven by the optical field. As plotted in Fig.8.5 (a) and (b) the oscillations are for longer pulses (here 250 fs) not present at all since the polarizations have greatly decayed. In figure (a) and (b) a pulse of $1 \mu\text{J}/\text{cm}^2$ and $10 \mu\text{J}/\text{cm}^2$ has been used in the calculations. In both cases we find that it is possible to generate a 90% valley polarized state.

After having understood the main aspects of the equations we can now analyse the valley polarization after the optical excitation. The first attempt in achieving a highly valley polarized state is to reduce the Coulomb potentials strength and with that the inter valley coupling. In figure 8.6 the level of valley polarization is plotted as a function of screening, (a) via the dielectric environment and (b) via doping. In both cases the level of valley polarization can be enhanced. However, due to the long life time of the microscopic polarization this effect is rather small.

As discussed in the previous Chapter 8 the intervalley coupling vanishes for strongly off-resonant states. For detuned valleys we therefore, find a higher valley polarization after the optical excitation. This is shown in Fig.8.7 (a) where the valley polarization is plotted as a function of detuning. Our calculations show that with the enhancement of the detuning we can optically excite a 100% valley polarized state.

In Figure 8.7 we have plotted the valley polarization as a function of the homogeneous line

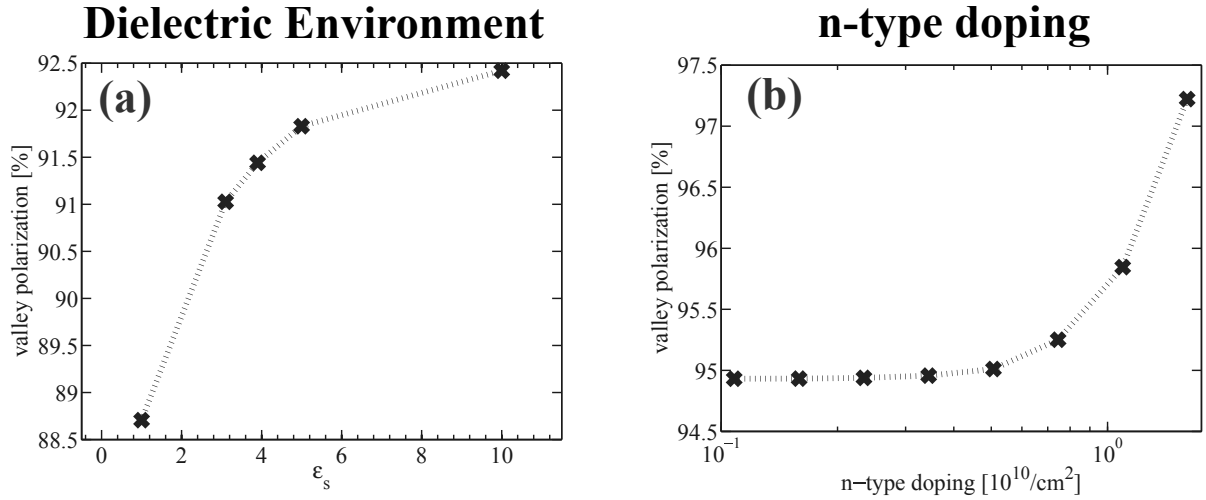


Figure 8.6: Optically induced valley polarization as function, (a) the dielectric environment characterized by ϵ_s and (b) n-type doping. The increase in doping or the dielectric constant ϵ_s leads to a higher screening of the coulomb potential. Consequently the Coulomb-induced intervalley coupling element is reduced, which leads to an enhancement of the optically generated valley polarization. The percentage of valley polarization is calculated with respect to the optically induced carriers. Note that in the doping calculations the total amount of carriers is dominated by the doping.

width. We find that with the decay of the polarization also the carrier intervalley redistribution vanishes. This can be understood from Eq.8.15, where one can see that the redistribution term is driven by the coherent quantity of the opposite valley.

Here we have discussed the principle mechanisms of the optical excitation of carriers under the influence of Coulomb-induced intervalley coupling. The coupling leads to a redistribution of optically excited carriers between the valleys. In the presence of the intrinsic intervalley coupling it is therefore not possible to optically generate fully valley polarized states. Our calculations predict a 90% valley polarization directly after the pump pulse. We have also discussed plausible ways to overcome this problem by decoupling the valleys. Here we have found three main aspects, the coulomb strength, the resonance between the states and the life time of the microscopic polarization. Since the life time of the microscopic polarization is an intrinsic parameter it can not be changed in experiments. This also leads to a limited effect of the screening of the coulomb potential.

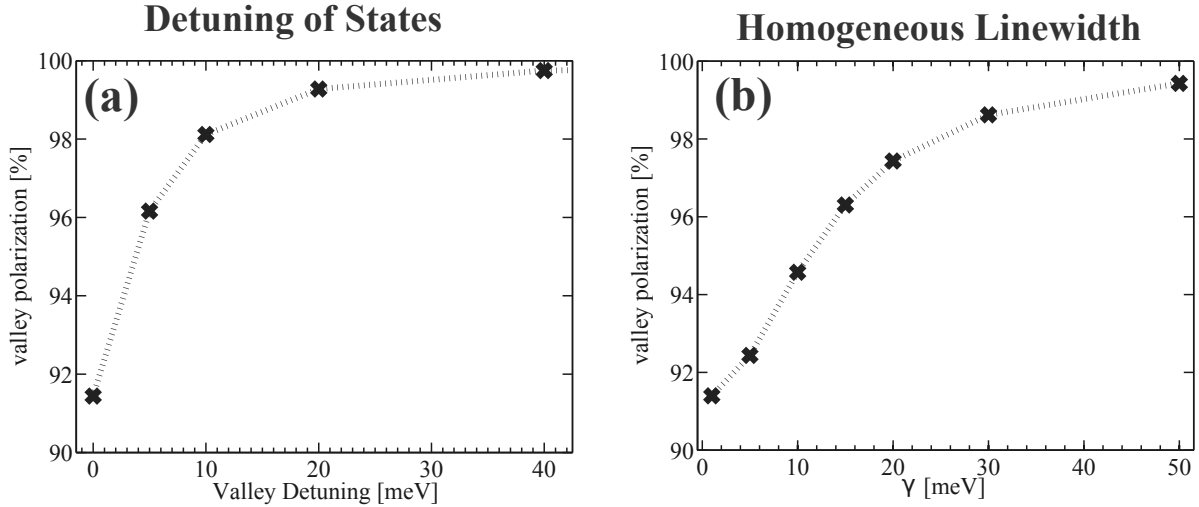


Figure 8.7: Optically induced valley polarization as function of, (a) detuning of resonant states in the K and K' valleys and (b) the homogeneous broadening γ . (a) The coupling between states of different valleys vanishes with the energy difference between these states. Therefore, the valley polarization enhances with the detuning of the states. (b) The wider the homogeneous line width the better is the valley polarization. The polarization lifetime is shorter for wider homogeneous line widths. With the decay of the coherent quantity also the redistribution term in equation Eq.8.15 vanishes.

8.5 VALLEY COUPLING IN TMDs

In the previous chapter we have discussed the impact of intervalley coupling on an two dimensional semiconductor with vanishing spin orbit coupling. We found that the detuning of the states with the spin but in opposite valleys decouples the valleys to a large extent as A and B excitons are separated by a few hundred meV. However as we will show in this section the intervalley bandgap renormalization is still meaning full in systems with largely detuned states. We will show that our calculations in agreement with the experimental results of Mai et al [53] where a OCP signal was found suggesting a red shift of the off resonant B exciton.

8.5.1 DIFFERENTIAL TRANSMISSION SPECTROSCOPY

In order to measure carrier dynamics in a solid one can use the pump-probe technique, which gives the temporal evolution of the transmission signal. For this technique at least three pulses are needed. First using a weak test pulse (such weak that one might safely say to be within the limit of linear optics) one measures the transmission spectrum and finds the systems response from e.g. the equilibrium state. Secondly the system is excited into a non-equilibrium state via

a so called pump pulse, e.g. carriers are excited from the valence into the conduction band or into excitonic states. Than again a test pulse is used to test the excited state of the system. One can now compare the transmission signal of the system before and after the pump pulse, this is the name giving step for differential transmission spectroscopy. This technique indirectly gives information about time evolution of carrier distributions in the system. However, data from such experiments have to be carefully interpreted, since they only give insights into spectral intensity shifts of the transmission spectrum.

For TMDs this technique can also be used to test the valley polarization after the optical generation of a spin-valley polarized state. Here the system ist tested via different circular polarization directions co and cross polarized with the pump pulse. Due to the circular dichroism one would here expect a considerable difference between the co and cross test-pulse answer.

8.5.2 DIFFERENTIAL TRANSMISSION SPECTROSCOPE IN VALLEY COUPLED WS₂

In this section we go back to the full electron-hole picture, which in contrast to the excitonic picture includes all states contributions and is also valid in a higher excitation regime. Note however that the stronger the optical excitation and the more carriers are generated the more important are also higher order correlation terms which are neglected in the present analyses, where we focus on the impact of the coherent quantity, the microscopic polarization.

As previously discussed optical properties of WS₂, MoS₂ and other transition metal dichalcogenides (TMDs) are characterized by pronounced excitonic transitions stemming from K and K' valleys [17, 47, 74, 92, 37, 105, 54]. We focus on microscopic modelling of the optical response of WS₂ after pumping of the energetically lowest A exciton in one of the two valleys.

We now solve the set of coupled equations Eq.8.11 and Eq.8.12. While the energy renormalization (Eq.8.13) shifts the entire spectrum to red, the renormalization of the Rabi frequency (Eq.8.14) gives rise to a significant reshape of the optical transition due to the formation of excitons characterized by binding energies in the range of one eV [16].

Furthermore, the phase space filling factor $(1 - f_{\mathbf{k}_s\xi}^h - f_{\mathbf{k}_s\xi}^e)$ appearing in the Bloch equation (8.11) in front of the renormalized Rabi frequency takes into account Pauli-blocking effects.

The strong Coulomb interaction in WS₂ also gives rise to a coupling of the K and K' valley. This contribution appears both in the renormalization of the energy and the Rabi frequency via the Coulomb matrix elements with $\xi' \neq \xi$. Due to the large spin orbit coupling the here studied A and B states of opposite valleys are highly of resonant and the intervalley renormalization of the Rabi-frequency is negligible.

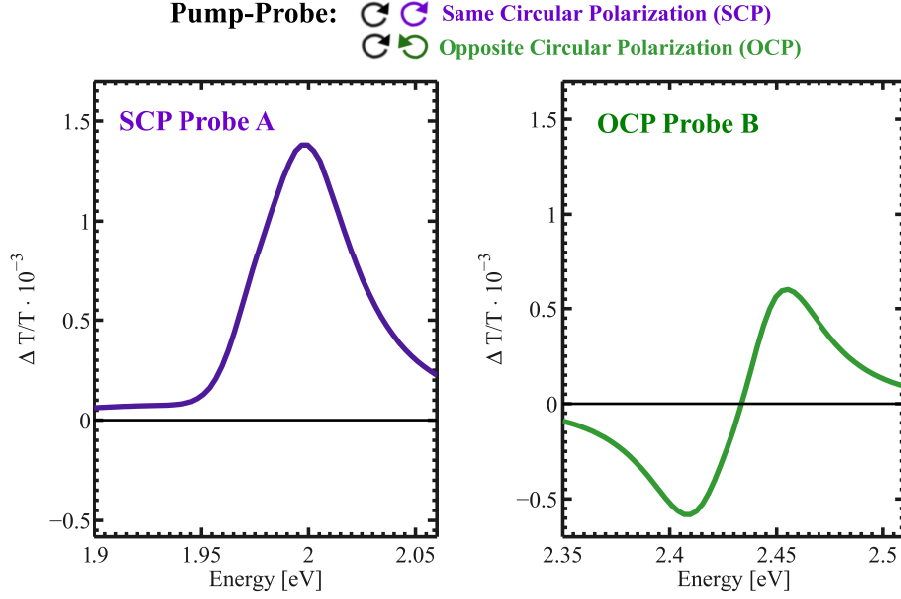


Figure 8.8: Differential transmission spectra for different pump fluences. (a) Pumping and probing the same valley (SCP) causes a pronounced absorption bleaching resulting in a positive signal. (b) In contrast, probing the other valley (OCP) leads to a dispersive signal including negative contributions due to the Coulomb-induced intervalley coupling.

The numerical solution of the TMD Bloch equations (8.11)-(8.12) gives us access to the microscopic polarization allowing us to calculate the frequency-dependent optical absorption $\alpha(\omega)$. Since the reflection in TMDs is known to be negligible [83], we assume for the transmission $T(\omega) = 1 - \alpha(\omega)$. Then, the experimentally observed differential transmission spectra (DTS) can be expressed as

$$\frac{T(\omega, \tau) - T_0(\omega)}{T_0(\omega)} = \frac{\alpha_0(\omega) - \alpha(\omega, \tau)}{1 - \alpha_0(\omega)} \quad (8.28)$$

with τ denoting the time delay between the pump and the probe pulse and $T_0(\alpha_0)$ describing the transmission (absorption) before the optical excitation.

In this work, we focus on the dynamics right after the optical excitation. We do not include scattering processes or coupling with impurities, which are assumed to give rise to a population decay on a time scale of hundreds of ps. The focus lies on the interplay between the valley-selective optical excitation and Coulomb interaction on the Hartree-Fock level including excitonic effects and intervalley coupling. The used pump fluence of $6.5 \mu\text{J}$ optically induces a carrier density of $2 \times 10^{11}/\text{cm}^2$, which corresponds to the performed experiments.

Pumping and probing the transition at the same state at the same valley (SCP), we observe

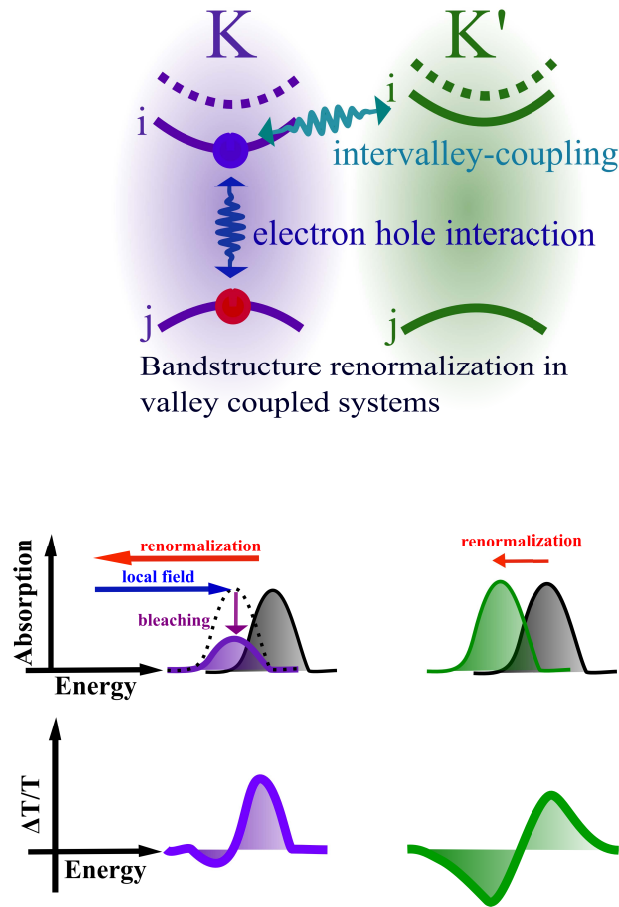


Figure 8.9: Coulomb-induced intervalley coupling of K and K' valleys. (a) Schematic drawing of the band structure of the K and K' valley. Due to optical pumping, the band gap and the Rabi frequency renormalized in the pumped K valley. The Coulomb interaction couples the K and K' valley, which also leads to a (smaller) band gap renormalization of the unpumped K' valley. (b) Origin of the dispersive profiles in the differential transmission spectra for same circular polarization of the resonantly pumped A-exciton (SCP) and opposite circular polarization (OCP) of the off-resonant B-exciton. Due to the band gap renormalization in the valleys, the absorption of the pumped system shifts to lower photon energies. In addition, strong bleaching in the pumped K valley occurs due to phase space filling.

an overall positive DTS due to the absorption bleaching of the probe pulse. The underlying Pauli blocking is expressed via the phase space filling factor appearing in Eq.8.11. In contrast, the DTS signals behaviour is much more complex, when we pump the A-exciton in one valley and probe the B-exciton in the opposite valleys (OCP). We find positive and negative DTS depending on the probe energy, cf. Fig. 8.8. This sign change in the DTS comes from a red shift of the excitonic transition in the unexcited valley.

The DTS behaviour can be understood as follows: First, the optically excited carriers at valley

ξ give rise to a change of the energy renormalization at both optically excited A-excitons in ξ and the undisturbed B-excitons in valley ξ' . The efficiency of the intervalley coupling is given by the corresponding Coulomb matrix element $V_{\mathbf{k}_s, \mathbf{k}'_s, \xi, \xi'}^{\lambda\lambda}$ with $\xi \neq \xi'$, cf. Eq. (8.13).

The resulting red-shift is much smaller than at the optically excited valley. Second, the phase space filling factor appearing in Eq. (8.11) and determining the absorption bleaching only changes for the transition at the optically excited valley ξ . The renormalization of the Rabi frequency is also not affected at the undisturbed valley ξ' . As a result, the excitonic binding energy and the oscillator strength of the excitonic transition at the valley ξ' remain unchanged, while there is a strong bleaching at the optically excited valley ξ . This process is illustrated in the right column of Figure 8.9 and explains, why the DTS is overall positive in the case of pumping and probing the same valley (SCP), cf. the purple line in Fig.8.8. See in contrast the right column of figure 8.9, for the OCP case, there is only a red shift due to the indirect change of the bandgap renormalization that influences the absorption of the probe pulse. This gives rise to a S-like DT curve (cf. the green line in Fig.8.8): For energies at the initial resonance, DTS is positive, while for energies at the red-shifted new resonance, DTS is negative reflecting an enhancement of the probe pulse absorption.

The Coulomb-induced valley coupling is expected to be strong for all TMD materials. We have focussed our investigation on WS_2 due to its large spin-orbit coupling allowing us to separate the dynamics of A and B excitons. The Coulomb-induced valley coupling requires a large momentum transfer q , where the Keldish Coulomb potential is dominated by the q^2 term [39, 19, 8, 5]. The screening of the potential is determined by the characteristic screening length $r_0 = d\epsilon_{\perp}/\epsilon_s$ with ϵ_s as the average dielectric constant of the surrounding medium, and the intrinsic material parameters d denoting its effective thickness and ϵ_{\perp} the dielectric tensor component [39, 19, 8]. The screening length determines the efficiency of the Coulomb-induced intervalley coupling for different TMD materials. Assuming the same surrounding medium, it only slightly varies for TMDs (WS_2 : $\epsilon_s r_0 \approx 3.7$ nm, MoS_2 : $\epsilon_s r_0 \approx 4.2$ nm, WSe_2 : $\epsilon_s r_0 \approx 4.5$ nm, and MoSe_2 : $\epsilon_s r_0 \approx 5.1$ nm.[8] Since the strength of the Coulomb-induced inter-valley coupling is approximately inversely proportional to the screening length r_0 , we expect the observed DTS behaviour to be the most prominent in the studied WS_2 .

CHAPTER 9

DISCUSSION

In this thesis, I applied the density matrix formalism to two novel nanostructures, the transition metal dichalcogenides and carbon hybrid nanostructures. In both cases the density matrix approach led to new insights on the intrinsic properties of the materials, which are of fundamental interest for the scientific community.

In the first part of this thesis, I showed how optical properties of graphene can be tailored. I have investigated the molecule-substrate coupling in nanoribbons of different widths up to graphene. In particular, I addressed the role of dimensionality and electronic bandstructure for the molecule-induced changes of optical properties of the carbon substrate. The dipole fields induced by the adsorbed photo-active molecules give rise to indirect optical transitions within the substrate resulting in a splitting of the pristine spectral resonances into multiple peaks combined with a considerable spectral shift. Both effects do not only depend on the molecular properties, such as the dipole moment, dipole orientation, and molecular coverage, but they are also strongly influenced by the electronic bandstructure of the substrate. To gain fundamental insights into the molecule-substrate coupling, I have also derived analytical solutions for the limiting case of a simplified parabolic system addressing the importance of the band curvature. Furthermore, my calculations reveal the significant role of the dimensionality of the substrate. The increased number of involved states of the two-dimensional graphene increases the impact of the adsorbed molecules. At the same time, the molecular interference within the graphene surface becomes more important leading to a spectrally narrow molecule-substrate coupling. As a result, the predicted peak splitting and the spectral shift vanish within the graphene continuum. However, at the high-symmetry Dirac point and the saddle-point, I observe clear changes in the absorption spectrum of graphene: I predicted an enhanced absorption in the vicinity of the Dirac-point, which is induced by the superposition of the red-shifted spectral resonances.

Furthermore, the absorption peak at the saddle-point is broadened due to the appearance of a high-energy shoulder.

In summary, my results shed light on the molecule-substrate coupling in nanoribbons and graphene functionalized by photo-active molecules. The gained insights can guide future experiments in this growing research field and can be applied to other one- and two-dimensional substrates under the influence of a molecular dipole field.

In the second part, I investigated the excitonic and optical properties of transition metal dichalcogenides. I found an analytical treatment of the excitonic properties. The presented results, on the excitonic binding energies of the first and energetically higher excitonic states are in very good agreement with experiments [17] and the ab initio calculations [78, 50, 7, 76, 89, 17, 54, 85, 5]. The great advantage of this analytic approach is that it gives a intuitive solution to the problem and also allows to include and understand the the impact of important experimental parameters, like screening effects via the dielectric environment or the plasma screening induced by n- or p-type doping. Furthermore, I calculated the radiative dephasing and the inhomogeneously broadened absorption spectrum which again is in good agreement with experimental results [69]. The strong coupling of carriers to an electric field leads to extremely long lifetimes of coherent quantities. This is of crucial importance in the study of the material properties.

Overall this thesis on the optical and electronic properties of new material systems provide new insights in the field of material research. The theoretical predictions can guide future experiments on the way to exploit material properties for technological applications.

Appendices

APPENDIX A

LINDHARD SCREENING

In a charge carrier plasma the coulomb force of one carrier is screened by the surrounding carriers. This is one of the most important effects in many-body carrier interactions. The plasma screening can be derived selfconsistently within the density matrix approach, via the solution of the heisenbergs equation of motion and the poisson equation for the induced coulomb potential,[33]

$$\nabla^2 V_{ind} = \frac{|e|\rho}{4\pi\epsilon_0}. \quad (\text{A.1})$$

For our system we find the dynamic dielectric function as,

$$\epsilon(\xi\mathbf{q}) = 1 - V_{\xi\mathbf{q}} \sum_{\xi'\mathbf{k}} \Gamma_{\mathbf{k},\mathbf{k}-\mathbf{q}}^{\lambda\lambda\xi} \frac{f_{\xi'\mathbf{k}-\mathbf{q}}^\lambda - f_{\xi'\mathbf{k}}^\lambda}{\hbar\omega - i\delta - \epsilon_{\xi'\mathbf{k}-\mathbf{q}}^\lambda - \epsilon_{\xi'\mathbf{k}}^\lambda} \quad (\text{A.2})$$

this screening has been evaluated numerically within the static limit where $\hbar\omega - i\delta \rightarrow 0$. And the screened coulomb potential is given by,

$$V_{\mathbf{q}}^{\lambda\lambda\xi} \rightarrow V_{\mathbf{q}}^{\lambda\lambda\xi} = \frac{V_{\mathbf{q}}^{\lambda\lambda\xi}}{\epsilon(\xi\mathbf{q})} \quad (\text{A.3})$$

APPENDIX B

TMD PARAMETERS

The following parameters have been used in the calculations, taken from [78]

	m_e	m_h	ϵ_{gap} [eV]	ϵ_{SOC} [meV]
MoS ₂	0.62	0.54	2.82	164
MoSe ₂	0.7	0.55	2.41	212
WS ₂	0.44	0.45	2.88	456
WSe ₂	0.53	0.52	2.42	501

and from [8],

	a_0 [Å]	d_{M-X} [Å]	ϵ_{\perp}	$\epsilon_s r_0$ [nm]
MoS ₂	3.16	1.59	13.36	4.2
MoSe ₂	3.3	1.67	15.27	5.1
WS ₂	3.16	1.59	11.75	3.7
WSe ₂	3.26	1.67	13.63	4.5

APPENDIX B. TMD PARAMETERS

APPENDIX C

RADIATIVE COUPLING; HOMOGENEOUS AND INHOMOGENEOUS LINEWIDTH

For normal incidence of the optical field on a two-dimensional material, the field is assumed to travel as a plane wave varying only in the propagation direction (z -axis) with a polarization orthogonal to z -axis. The divergence of such a field vanishes, since the current and the field have no dependence on the x, y coordinates. Without loss of generality, y denotes a single polarization component and the one-dimensional wave equation takes the form:

$$\nabla^2 E^y - \frac{1}{c^2} \frac{\partial^2}{\partial t^2} E^y = \mu_0 \frac{\partial}{\partial t} j^y, \quad (\text{C.1})$$

with c being the velocity of light. j^y is the optically excited current localized in the 2dim material, which is transversal since it depends only on t and z , i.e. $\nabla \cdot \mathbf{j}(z, t) = 0$ and can only have a y component. Before we use this property of the electron current in the 2dim material, C.1 can be solved formally without a detailed knowledge of the current by writing the solution of the wave equation as:

$$E^y = -\frac{\mu_0}{4\pi} \frac{\partial}{\partial t} \int d^3 r' \frac{j^y(\mathbf{r}', t - \frac{|\mathbf{r}-\mathbf{r}'|}{c})}{|\mathbf{r}-\mathbf{r}'|} + E_0(t - z/c). \quad (\text{C.2})$$

Here, the first term on the right-hand side is the solution of the inhomogeneous wave equation and the second term constitutes the homogeneous solution, given by the externally incident field E_0 , which only depends on the wave coordinate $t - \frac{z}{c}$.

To further apply this very formal solution, the space dependence of the current j^y must be determined. Treating the material as 2dim electron systems on the length scale of the wave-

APPENDIX C. RADIATIVE COUPLING; HOMOGENEOUS AND INHOMOGENEOUS LINEWIDTH

length of the incident light, we approximate the space dependence of the current using delta-like contributions as:

$$j^y(z) = \delta(z - z_0)j(t, x, y). \quad (\text{C.3})$$

For plane wave propagation, the current should not depend on a specific x, y value:

$$j^y(z) = \delta(z - z_0)j(t). \quad (\text{C.4})$$

The knowledge of the explicit z -dependence and the independence of the current on x and y in C.3 allows us to carry out the angle integration in the plane of the sample (cylinder coordinates) yielding for the inhomogeneous solution:

$$E_{inh}^y = -\frac{\mu_0}{2} \int_{-\infty}^{+\infty} dz' \delta(z' - z_0) \int_0^{\infty} d\rho' \rho' \frac{\partial}{\partial t} \left(\frac{j(t - \frac{\sqrt{(z-z')^2 + \rho'^2}}{c})}{\sqrt{(z-z')^2 + \rho'^2}} \right). \quad (\text{C.5})$$

We have restricted the analysis to the in-plane position $\rho = 0$ which is possible due to the invariance of the problem with respect to in-plane motion in the 2dim material. If the variable $x = \frac{\sqrt{(z-z')^2 + \rho'^2}}{c}$ is introduced and $dx = \frac{1}{x} \frac{\rho' d\rho'}{c^2}$, the resulting expression can be written as:

$$\begin{aligned} E_{inh}^y &= \frac{c\mu_0}{2} \int_{-\infty}^{+\infty} dz' \delta(z' - z_0) \int_{\frac{|z-z'|}{c}}^{\infty} dx \frac{\partial}{\partial x} (j^y(t - x)), \\ &= -\frac{c\mu_0}{2} \int_{-\infty}^{+\infty} dz' \delta(z' - z_0) j^y \left(t - \frac{|z - z'|}{c} \right), \end{aligned} \quad (\text{C.6})$$

where we have assumed that the current is vanishing for $x \rightarrow \infty$. Evaluating the δ -function and adding the incident field provides the full solution in the following form:

$$E^y = -\frac{c\mu_0}{2} j^y \left(t - \frac{|z - z_0|}{c} \right) + E_0 \left(t - \frac{z}{c} \right). \quad (\text{C.7})$$

Obviously, the propagated field is given by the incident field E_0 plus a renormalization contribution determined by the currents emitted with retarded time argument $t - \frac{|z-z_0|}{c}$. The field E can be decomposed in the incoming E_0 , reflected E_R , and the transmitted contribution E_T , cf. Fig. C.1. Then, the transmission coefficient $T(\omega)$ is given by:

$$T(\omega) = \left| \frac{E_T(\omega, z)}{E_0(\omega, z)} \right|^2. \quad (\text{C.8})$$

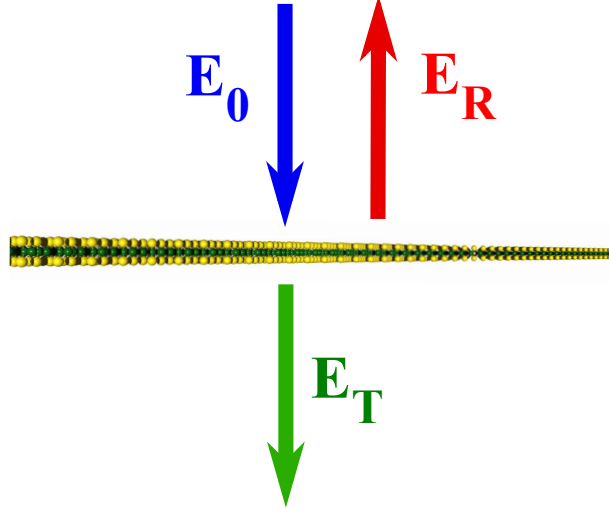


Figure C.1: Transmitted (E_T), reflected (E_R) and incident (E_0) electrical field.

Within the linear optics, the current depends linearly on the field, i.e. $j(\omega) = \sigma_{2D}(\omega)E(\omega) = -i\omega\varepsilon_0\chi_{2D}(\omega)E(\omega)$, where χ_{2D} is the susceptibility and

$$\sigma_{2D}(\omega) = -i\omega\varepsilon_0\chi_{2D}(\omega) \quad (\text{C.9})$$

is the conductivity in the 2dim material. The transmitted field can be expressed as:

$$E_T(\omega) = E_0(\omega) + \frac{\mu_0\varepsilon_0c}{2}i\omega\chi_{2D}(\omega)E_{2D}(\omega), \quad (\text{C.10})$$

where $E_{2D}(\omega)$ is the field directly at the position of the 2dim material. Using $E_{2D}(\omega) = E_T(\omega)$ at $z = 0$ (continuity of field) and $c = \frac{c_0}{n_B}$ with n_B as the background refraction index, it follows:

$$\frac{E_T(\omega)}{E_0(\omega)} = \frac{1}{1 - i\frac{\omega}{2c_0n_B}\chi_{2D}(\omega)}. \quad (\text{C.11})$$

As a result, we obtain for the transmission coefficient:

$$T(\omega) = \frac{1}{\left|1 - i\frac{\omega}{2c_0n_B}\chi_{2D}(\omega)\right|^2}. \quad (\text{C.12})$$

Similarly, we obtain for the reflected field $E_R(t + \frac{z}{c})$:

$$E_R(\omega) = i\frac{\omega}{2n_Bc_0}\chi_{2D}(\omega)E_{2D}(\omega)e^{-i\frac{z}{c}\omega} = \frac{i\frac{\omega}{2n_Bc_0}\chi_{2D}(\omega)}{1 - i\frac{\omega}{2c_0}\chi_{2D}(\omega)}E_0(\omega)e^{-i\frac{z}{c}\omega}. \quad (\text{C.13})$$

Therefore the reflection coefficient reads:

$$R(\omega) = \left| \frac{E_R(\omega, z)}{E_0(\omega, z)} \right|^2 = \frac{\frac{\omega^2}{4c_0^2 n_B^2} |\chi_{2D}(\omega)|^2}{\left| 1 - i \frac{\omega}{2c_0 n_B} \chi_{2D}(\omega) \right|^2}. \quad (\text{C.14})$$

Combining our results, we find for the true absorption $\alpha(\omega)$ in 2dim materials: The absorption is given by the imaginary part of the susceptibility $Im[\chi_{2D}(\omega)]$ and a denominator which contains the radiative coupling within the 2d material. The latter contributes to a homogeneous width of the excitonic transitions.

So far, we have considered the case of a TMD monolayer surrounded from both sides by a medium with the dielectric constant ε_B (and a refractive index n_B). Extending the calculation to the more general case of two different substrates with ε_1 and ε_2 that are located above and below the TMD layer, we have to generalize the boundary conditions when solving the wave equation. Here, we obtain for the absorption coefficient

$$\alpha(\omega) = \frac{\frac{\omega}{c_0 n_1} \Im[\chi_{2D}(\omega)]}{\left| \frac{1}{2} \left(1 + \frac{n_2}{n_1} \right) - i \frac{\omega}{2c_0 n_1} \chi_{2D}(\omega) \right|^2}.$$

The light matter coupling has been fitted to experimental value of 10% absorption. Since the measured absorption stems from an inhomogeneously widened peak. We have calculated use a Gaussian Ansatz in the form,

$$\alpha(\omega)_{inhom} = \frac{1}{\epsilon_0 \omega N} \int \lim_{\gamma \rightarrow 0} \frac{1}{\epsilon_0 \omega} \sum_{\nu\xi, s} \frac{\Theta_{\nu\xi}^{si}}{\underbrace{E_{\nu\xi}^{si} - \hbar\omega - i\gamma}_{\Delta E_i}} \exp\left[-\frac{\Delta E_i^2}{2\sigma^2}\right] di$$

where the FWHM of the gaussian spectra has been chosen 50 meV (or $\sigma = 21$) has been used and $N = \int \exp[-\Delta E_i^2/\sigma^2] di$ the normalization factor, this formula can be used for vanishing γ . This procedure gives a total of overlap integrals of 1.5 nm^{-1} and results in a homogeneous peak width of 1.4 meV or 0.5 ps.

BIBLIOGRAPHY

- [1] Xiaohong An, Thomas W. Butler, Morris Washington, Saroj K. Nayak, and Swastik Kar. Optical and sensing properties of 1-pyrenecarboxylic acid-functionalized graphene films laminated on polydimethylsiloxane membranes. *ACS Nano*, 5(2):1003–1011, 2011.
- [2] Phaedon Avouris and Christos Dimitrakopoulos. Graphene: synthesis and applications. *Mat. Today*, 15(3):86–97, March 2012.
- [3] Balog Richard, Jorgensen Bjarke, Nilsson Louis, Andersen Mie, Rienks Emile, Bianchi Marco, Fanetti Mattia, Laegsgaard Erik, Baraldi Alessandro, Lizzit Silvano, Sljivancanin Zeljko, Besenbacher Flemming, Hammer Bjork, Pedersen Thomas G., Hofmann Philip, and Hornekaer Liv. Bandgap opening in graphene induced by patterned hydrogen adsorption. *Nat Mater*, 9(4):315–319, apr 2010.
- [4] Cristina Bena and Gilles Montambaux. Remarks on the tight-binding model of graphene. *New Journal of Physics*, 11(9):095003, 2009.
- [5] Gunnar Berghäuser and Ermin Malic. Analytical approach to excitonic properties of mos_2 . *Phys. Rev. B*, 89:125309, Mar 2014.
- [6] Berghäuser Gunnar and Malić Ermin. Molecule–substrate interaction in functionalized graphene. *Carbon*, 69(0):536–542, apr 2014.
- [7] Timothy C. Berkelbach, Mark S. Hybertsen, and David R. Reichman. Theory of neutral and charged excitons in monolayer transition metal dichalcogenides. *Phys. Rev. B*, 88:045318, Jul 2013.
- [8] Timothy C. Berkelbach, Mark S. Hybertsen, and David R. Reichman. Theory of neutral and charged excitons in monolayer transition metal dichalcogenides. *Phys. Rev. B*, 88:045318, Jul 2013.

BIBLIOGRAPHY

- [9] Niels Bode, Eros Mariani, and Felix von Oppen. Transport properties of graphene functionalized with molecular switches. Journal of Physics: Condensed Matter, 24(39):394017, 2012.
- [10] F. Bonaccorso, Z. Sun, T. Hasan, and A. C. Ferrari. Graphene photonics and optoelectronics. Nature Photonics, 4(9):611, 2010.
- [11] Brar Victor W., Decker Regis, Solowan Hans-Michael, Wang Yang, Maserati Lorenzo, Chan Kevin T., Lee Hoonkyung, Girit Caglar O., Zettl Alex, Louie Steven G., Cohen Marvin L., and Crommie Michael F. Gate-controlled ionization and screening of cobalt adatoms on a graphene surface. Nat Phys, 7(1):43–47, jan 2011. 10.1038/nphys1807.
- [12] Ting Cao, Gang Wang, Wenpeng Han, Huiqi Ye, Chuanrui Zhu, Junren Shi, Qian Niu, Pingheng Tan, Enge Wang, Baoli Liu, and Ji Feng. Valley-selective circular dichroism of monolayer molybdenum disulphide. Nat Commun, 3:887, jun 2012.
- [13] E. Cappelluti, R. Roldán, J. A. Silva-Guillén, P. Ordejón, and F. Guinea. Tight-binding model and direct-gap/indirect-gap transition in single-layer and multilayer mos_2 . Phys. Rev. B, 88:075409, Aug 2013.
- [14] A. H. Castro Neto, F. Guinea, N. M. R. Peres, K. S. Novoselov, and A. K. Geim. The electronic properties of graphene. Rev. Mod. Phys., 81(1):109–162, Jan 2009.
- [15] D. Chae, T. Utikal, S. Weisenburger, H. Giessen, and v. Klitzing K. Excitonic fano resonance in free-standing graphene. Nano Lett., 11:1379, 2011.
- [16] Tawinan Cheiwchanchamnangij and Walter R. L. Lambrecht. Quasiparticle band structure calculation of monolayer, bilayer, and bulk mos_2 . Phys. Rev. B, 85:205302, May 2012.
- [17] Alexey Chernikov, Timothy C. Berkelbach, Heather M. Hill, Albert Rigosi, Yilei Li, Ozgur Burak Aslan, David R. Reichman, Mark S. Hybertsen, and Tony F. Heinz. Exciton binding energy and nonhydrogenic rydberg series in monolayer ws_2 . Phys. Rev. Lett., 113:076802, Aug 2014.
- [18] C. Cohen-Tannoudji and G. Grynberg J. Dupont-Roc. Photons & Atoms. Wiley, 3 edition, 1989.
- [19] Pierluigi Cudazzo, Ilya V. Tokatly, and Angel Rubio. Dielectric screening in two-dimensional insulators: Implications for excitonic and impurity states in graphene. Phys. Rev. B, 84:085406, Aug 2011.

BIBLIOGRAPHY

- [20] D. C. Elias, R. R. Nair, T. M. G. Mohiuddin, S. V. Morozov, P. Blake, M. P. Halsall, A. C. Ferrari, D. W. Boukhvalov, M. I. Katsnelson, A. K. Geim, and K. S. Novoselov. Control of graphene's properties by reversible hydrogenation: Evidence for graphane. Science, 323(5914):610–613, 2009.
- [21] Englert Jan M., Dotzer Christoph, Yang Guang, Schmid Martin, Papp Christian, Gottfried J. Michael, Steinrück Hans-Peter, Spiecker Erdmann, Hauke Frank, and Hirsch Andreas. Covalent bulk functionalization of graphene. Nat Chem, 3(4):279–286, apr 2011.
- [22] Motohiko Ezawa. Peculiar width dependence of the electronic properties of carbon nanoribbons. Phys. Rev. B, 73:045432, Jan 2006.
- [23] U. Fano. Description of states in quantum mechanics by density matrix and operator techniques. Rev. Mod. Phys., 29:74–93, Jan 1957.
- [24] Ugo Fano. Density matrices as polarization vectors. Rendiconti Lincei, 6(2):123–130, 1995.
- [25] S. Garaj, W. Hubbard, A. Reina, J. Kong, D. Branton, and J.A. Golovchenko. Graphene as a subnanometre trans-electrode membrane. Nature, 467(7312):190–193, September 2010.
- [26] Geim A. K. and Novoselov K. S. The rise of graphene. Nat Mater, 6(3):183–191, mar 2007. 10.1038/nmat1849.
- [27] A. Grüneis, R. Saito, G. G. Samsonidze, T. Kimura, M. A. Pimenta, A. Jorio, A. G. SouzaFilho, G. Dresselhaus, and M. S. Dresselhaus. Inhomogeneous optical absorption around the K point in graphite and carbon nanotubes. Phys. Rev. B, 67:165402, 2003.
- [28] Alexander Grüneis. Synthesis and electronic properties of chemically functionalized graphene on metal surfaces. Journal of Physics: Condensed Matter, 25(4):043001, 2013.
- [29] XF Guo, LM Huang, S O'Brien, P Kim, and C Nuckolls. Directing and sensing changes in molecular conformation on individual carbon nanotube field effect transistors. J. Am. Chem. Soc., 127(43):15045, 2005.
- [30] Tahir Cagin Haldun Sevincli, Cem Sevik and Gianaurelio Cuniberti. A bottom-up route to enhance thermoelectric figures of merit graphene nanoribbons. Sci. Rep., 3(10.1038/s-rep01228):2013/02/06/online, Feb 2013.

BIBLIOGRAPHY

- [31] Melinda Y. Han, Barbaros Özyilmaz, Yuanbo Zhang, and Philip Kim. Energy band-gap engineering of graphene nanoribbons. Phys. Rev. Lett., 98:206805, May 2007.
- [32] S. J. M. F. E. Harris and D.L. Freeman. Algebraic and diagrammatic methods in many-fermion theory. Oxford Press, New York, first edition edition, 1992.
- [33] H. Haug and Stephan W. Koch. Quantum Theory of the Optical and Electronic Properties of Semiconductors. World Scientific Publishing Co. Pre. Ltd., fifth edition edition, 2004.
- [34] A Hirsch and O Vostrowsky. Functionalization of carbon nanotubes. In Functional Molecular Nanostructures, volume 245 of Top. Curr. Chem., page 193. 2005.
- [35] Yu. A. Il'inskii and L. V. Keldysh. Electromagnetic Response of Material Media. Springer, 2007.
- [36] Mark J. Low and High Dielectric Constant Materials: Materials Science, Processing, and Reliability Issues Proceedings of the Fifth International Symposium. Electrochemical Society Lododa, 2000.
- [37] Wencan Jin, Po-Chun Yeh, Nader Zaki, Datong Zhang, Jerzy T. Sadowski, Abdullah Al-Mahboob, Arend M. van der Zande, Daniel A. Chenet, Jerry I. Dadap, Irving P. Herman, Peter Sutter, James Hone, and Richard M. Osgood. Direct measurement of the thickness-dependent electronic band structure of mos_2 using angle-resolved photoemission spectroscopy. Phys. Rev. Lett., 111:106801, Sep 2013.
- [38] Ado Jorio, Mildred S. Dresselhaus, Riichiro Saito, and Gene Dresselhaus. Raman spectroscopy in graphene related systems. Wiley-VCH, January 2011.
- [39] L. V. Keldysh. Coulomb interaction in thin semiconductor and semimetal films. JETP Lett., 29:658, 1979.
- [40] M. Kira, W. Hoyer, T. Stroucken, and S. W. Koch. Exciton formation in semiconductors and the influence of a photonic environment. Phys. Rev. Lett., 87(17):176401, Oct 2001.
- [41] M. Kira and S. W. Koch. Exciton-population inversion and terahertz gain in semiconductors excited to resonance. Phys. Rev. Lett., 93(7):076402, Aug 2004.
- [42] M. Kira and S. W. Koch. Quantum-optical spectroscopy of semiconductors. Phys. Rev. A, 73(1):013813, Jan 2006.
- [43] M. Kira and S. W. Koch. Semiconductor Quantum Optics. Cambridge University Press, first edition edition, 2011.

BIBLIOGRAPHY

- [44] M. Kira and S.W. Koch. Many-body correlations and excitonic effects in semiconductor spectroscopy, volume 30. IEEE Journal of Quantum Electronics, 2006.
- [45] Gerasimos Konstantatos, Michela Badioli, Louis Gaudreau, Johann Osmond, Maria Bernechea, de Arquer F. Pelayo Garcia, Fabio Gatti, and Frank H. L. Koppens. Hybrid graphene-quantum dot phototransistors with ultrahigh gain. Nat Nano, 7(6):363–368, jun 2012. 10.1038/nnano.2012.60.
- [46] Andor Kormányos, Viktor Zólyomi, Neil D. Drummond, Péter Rakyta, Guido Burkard, and Vladimir I. Fal’ko. Monolayer mos_2 : Trigonal warping, the γ valley, and spin-orbit coupling effects. Phys. Rev. B, 88:045416, Jul 2013.
- [47] T. Korn, S. Heydrich, M. Hirmer, J. Schmutzler, and C. SchÄijller. Low-temperature photocarrier dynamics in monolayer mos_2 . Appl. Phys. Lett., 99(10):–, 2011.
- [48] Dmitry V. Kosynkin, Amanda L. Higginbotham, Alexander Sinitskii, Jay R. Lomeda, Ayrat Dimiev, B. Katherine Price, and James M. Tour. Longitudinal unzipping of carbon nanotubes to form graphene nanoribbons. Nature, 458(7240):872–876, April 2009.
- [49] Yilei Li, Jonathan Ludwig, Tony Low, Alexey Chernikov, Xu Cui, Ghidewon Arefe, Young Duck Kim, Arend M. van der Zande, Albert Rigosi, Heather M. Hill, Suk Hyun Kim, James Hone, Zhiqiang Li, Dmitry Smirnov, and Tony F. Heinz. Valley splitting and polarization by the zeeman effect in monolayer mose_2 . Phys. Rev. Lett., 113:266804, Dec 2014.
- [50] Yuxuan Lin, Xi Ling, Lili Yu, Shengxi Huang, Allen L. Hsu, Yi-Hsien Lee, Jing Kong, Mildred S. Dresselhaus, and TomÅas Palacios. Dielectric screening of excitons and trions in single-layer mos_2 . Nano Letters, 14(10):5569–5576, 2014.
- [51] Gui-Bin Liu, Wen-Yu Shan, Yugui Yao, Wang Yao, and Di Xiao. Three-band tight-binding model for monolayers of group-vib transition metal dichalcogenides. Phys. Rev. B, 88:085433, Aug 2013.
- [52] David MacNeill, Colin Heikes, Kin Fai Mak, Zachary Anderson, Andor KormÅanyos, Viktor ZÅslyomi, Jiwoong Park, and Daniel C. Ralph. Breaking of valley degeneracy by magnetic field in monolayer mose_2 . arXiv:1407.0686, 2014.
- [53] Cong Mai, Yuriy G. Semenov, Andrew Barrette, Yifei Yu, Zhenghe Jin, Linyou Cao, Ki Wook Kim, and Kenan Gundogdu. Exciton valley relaxation in a single layer of ws_2 measured by ultrafast spectroscopy. Phys. Rev. B, 90:041414, Jul 2014.

BIBLIOGRAPHY

- [54] Kin Fai Mak, Keliang He, Changgu Lee, Gwan Hyoung Lee, James Hone, Tony F. Heinz, and Jie Shan. Tightly bound trions in monolayer MoS₂. Nat Mater, 12(3):207–211, mar 2013.
- [55] Kin Fai Mak, Keliang He, Jie Shan, and Tony F. Heinz. Control of valley polarization in monolayer MoS₂ by optical helicity. Nat Nano, 7(8):494–498, aug 2012.
- [56] Kin Fai Mak, Changgu Lee, James Hone, Jie Shan, and Tony F. Heinz. Atomically thin mos₂: A new direct-gap semiconductor. Phys. Rev. Lett., 105:136805, Sep 2010.
- [57] Kin Fai Mak, Matthew Y. Sfeir, Yang Wu, Chun Hung Lui, James A. Misewich, and Tony F. Heinz. Measurement of the optical conductivity of graphene. Phys. Rev. Lett., 101(19):196405, 2008.
- [58] E. Malic and A. Knorr. Graphene and Carbon Nanotubes: Ultrafast Relaxation Dynamics and Optics. Wiley-VCH, Berlin, first edition, 2013.
- [59] E. Malić, C. Weber, M. Richter, V. Atalla, T. Klamroth, P. Saalfrank, S. Reich, and A. Knorr. Microscopic model of the optical absorption of carbon nanotubes functionalized with molecular spiropyran photoswitches. Phys. Rev. Lett., 106(9):097401, 2011.
- [60] Ermin Malic, Heiko Appel, Oliver T. Hofmann, and Angel Rubio. Energy-transfer in porphyrin- functionalized graphene. physica status solidi (b), 251(12):2495–2498, 2014.
- [61] Ermin Malic, Heiko Appel, Oliver T. Hofmann, and Angel Rubio. Förster-induced energy transfer in functionalized graphene. The Journal of Physical Chemistry C, 118(17):9283–9289, 2014.
- [62] Ermin Malić, Matthias Hirtshulz, Frank Milde, Andreas Knorr, and Stephanie Reich. Analytical approach to optical absorption in carbon nanotubes. Phys. Rev. B, 74(19):195431, 2006.
- [63] Ermin Malić, Matthias Hirtshulz, Frank Milde, Janina Maultzsch, Stephanie Reich, and Andreas Knorr. Coulomb effects in single-walled carbon nanotubes. Phys. Stat. Solidi (B), 245:2155, 2008.
- [64] Ermin Malić, Matthias Hirtshulz, Frank Milde, Yang Wu, Janina Maultzsch, Tony F. Heinz, Andreas Knorr, and Stephanie Reich. Theory of rayleigh scattering from metallic carbon nanotubes. Phys. Rev. B, 77(4):045432, 2008.

BIBLIOGRAPHY

- [65] Ermin Malić, Antonio Setaro, Pascal Bluemmel, Carlos F. Sanz-Navarro, Pablo Ordejon, Stephanie Reich, and Andreas Knorr. Carbon nanotubes as substrates for molecular spiropyran-based switches. *J. Phys. Condens. Matter*, 24:394006, 2012.
- [66] Ermin Malić, Torben Winzer, Evgeny Bobkin, and Andreas Knorr. Microscopic theory of absorption and ultrafast many-particle kinetics in graphene. *Phys. Rev. B*, 84(20):205406, November 2011.
- [67] M. Mittendorff, F. Wendler, E. Malic, A. Knorr, M. Orlita, M. Potemski, C. Berger, W. A. de Heer, H. Schneider, M. Helm, and S. Winnerl. Carrier dynamics in Landau-quantized graphene featuring strong Auger scattering. *Nature Phys.*, 11:75–81, 2015.
- [68] Alejandro Molina-Sánchez, Davide Sangalli, Kerstin Hummer, Andrea Marini, and Ludger Wirtz. Effect of spin-orbit interaction on the optical spectra of single-layer, double-layer, and bulk mos_2 . *Phys. Rev. B*, 88:045412, Jul 2013.
- [69] Galan Moody, Chandriker Kavir, Dass, Kai Hao, Chang-Hsiao Chen, Lain-Jong Li, Akshay Singh, Kha Tran, Genevieve Clark, Xiaodong Xu, Gunnar Berghäuser, Ermin Malic, Andreas Knorr, and Xiaoqin Li. Intrinsic exciton linewidth in monolayer transition metal dichalcogenides. [arXiv:1410.3143](https://arxiv.org/abs/1410.3143), 2014.
- [70] K.S. Novoselov, A.K. Geim, S.V. Morozov, D. Jiang, Y. Zhang, S.V. Dubonos, I.V. Grigorieva, and Frisov A.A. Electric field effect in atomically thin carbon films. *Science*, 306:666–669, 2004.
- [71] Novoselov K. S., Fal’ko V. I., Colombo L., Gellert P. R., Schwab M. G., and Kim K. A roadmap for graphene. *Nature*, 490(7419):192–200, oct 2012.
- [72] H. Ochoa and R. Roldán. Spin-orbit-mediated spin relaxation in monolayer mos_2 . *Phys. Rev. B*, 87:245421, Jun 2013.
- [73] F. Parhizgar, H. Rostami, and Reza Asgari. Indirect exchange interaction between magnetic adatoms in monolayer mos_2 . *Phys. Rev. B*, 87:125401, Mar 2013.
- [74] G. Plechinger, S. Heydrich, J. Eroms, D. Weiss, C. SchÄijller, and T. Korn. Raman spectroscopy of the interlayer shear mode in few-layer mos_2 flakes. *Appl. Phys. Lett.*, 101(10):–, 2012.
- [75] Deborah Prezzi, Daniele Varsano, Alice Ruini, Andrea Marini, and Elisa Molinari. Optical properties of graphene nanoribbons: The role of many-body effects. *Phys. Rev. B*, 77(4):041404, 2008.

BIBLIOGRAPHY

- [76] Diana Y. Qiu, Felipe H. da Jornada, and Steven G. Louie. Optical spectrum of mos_2 : Many-body effects and diversity of exciton states. Phys. Rev. Lett., 111:216805, Nov 2013.
- [77] B Radisavljevic, A Radenovic, J Brivio, V Giacometti, and A Kis. Single-layer MoS2 transistors. Nat Nano, 6(3):147–150, mar 2011.
- [78] Ashwin Ramasubramaniam. Large excitonic effects in monolayers of molybdenum and tungsten dichalcogenides. Phys. Rev. B, 86:115409, Sep 2012.
- [79] Stephanie Reich, Christian Thomsen, and Janina Maultzsch. Carbon Nanotubes: Basic Concepts and Physical Properties. Wiley-VCH, Berlin, 2004.
- [80] Alex W. Robertson, Barbara Montanari, Kuang He, Judy Kim, Christopher S. Allen, Yimin A. Wu, Jaco Olivier, Jan Neethling, Nicholas Harrison, Angus I. Kirkland, and Jamie H. Warner. Dynamics of single fe atoms in graphene vacancies. Nano Lett. Web: March 21, 2013.
- [81] Michael Rohlfing. Redshift of excitons in carbon nanotubes caused by the environment polarizability. Phys. Rev. Lett., 108:087402, Feb 2012.
- [82] G. Sallen, L. Bouet, X. Marie, G. Wang, C. R. Zhu, W. P. Han, Y. Lu, P. H. Tan, T. Amand, B. L. Liu, and B. Urbaszek. Robust optical emission polarization in mos_2 monolayers through selective valley excitation. Phys. Rev. B, 86:081301, Aug 2012.
- [83] R Schmidt, G Berghäuser, E. Malic, A Knorr, R Schneider, P Tonndorf, S Michaelis de Vasconcellos, and R Bratschitsch. Ultrafast coulomb intervalley coupling in atomically thin ws_2 . submitted for publication, 2014.
- [84] Antonio Setaro, Pascal Bluemmel, Chandan Maity, Stefan Hecht, and Stephanie Reich. Non-Covalent Functionalization of Individual Nanotubes with Spiropyran-Based Molecular Switches. Advanced Functional Materials, 22(11):2425–2431, 2012.
- [85] Hongyan Shi, Rusen Yan, Simone Bertolazzi, Jacopo Brivio, Bo Gao, Andras Kis, Debdeep Jena, Huili Grace Xing, and Libai Huang. Exciton Dynamics in Suspended Monolayer and Few-Layer MoS2 2D Crystals. ACS Nano, 7(2):1072–1080, 2013.

BIBLIOGRAPHY

- [86] J. M. Simmons, I. In, V. E. Campbell, T. J. Mark, F. Léonard, P. Gopalan, and M. A. Eriksson. Optically modulated conduction in chromophore-functionalized single-wall carbon nanotubes. *Phys. Rev. Lett.*, 98(8):086802, Feb 2007.
- [87] N. Singh, G. Jabbour, and U. Schwingenschlögl. Optical and photocatalytic properties of two-dimensional mos₂. *The European Physical Journal B*, 85(11):1–4, 2012.
- [88] Andrea Splendiani, Liang Sun, Yuanbo Zhang, Tianshu Li, Jonghwan Kim, Chi-Yung Chim, Giulia Galli, and Feng Wang. Emerging photoluminescence in monolayer mos₂. *Nano Lett.*, 10(4):1271–1275, 2010.
- [89] A. Steinhoff, M. Rösner, F. Jahnke, T. O. Wehling, and C. Gies. Influence of excited carriers on the optical and electronic properties of mos₂. *Nano Letters*, 14(7):3743–3748, 2014.
- [90] Michael S. Strano. Probing chiral selective reactions using a revised katura plot for the interpretation of single-walled carbon nanotube spectroscopy. *J. Am. Chem. Soc.*, 125(51):16148–16153, December 2003.
- [91] Qi C. Sun, Lena Yadgarov, Rita Rosentsveig, Gotthard Seifert, Reshef Tenne, and Janice L. Musfeldt. Observation of a burstein-moss shift in rhenium-doped mos₂ nanoparticles. *ACS Nano*, 7(4):3506–3511, 2013.
- [92] Philipp Tonndorf, Robert Schmidt, Philipp Böttger, Xiao Zhang, Janna Börner, Andreas Liebig, Manfred Albrecht, Christian Kloc, Ovidiu Gordan, Dietrich R. T. Zahn, Stefan Michaelis de Vasconcellos, and Rudolf Bratschitsch. Photoluminescence emission and raman response of monolayer mos₂, mose₂, and wse₂. *Opt. Express*, 21(4):4908–4916, Feb 2013.
- [93] Haining Wang, Changjian Zhang, Weimin Chan, Christina Manolatu, Sandip Tiwari, and Farhan Rana. Radiative lifetimes of excitons and trions in monolayers of metal dichalcogenide mos₂. *arXiv:1402.0263*, 2014.
- [94] Ying Wang, Zhaohui Li, Jun Wang, Jinghong Li, and Yuehe Lin. Graphene and graphene oxide: biofunctionalization and applications in biotechnology. *Trends in Biotechnology*, 29(5):205 – 212, 2011.
- [95] F. Wendler and E. Malic. Carrier-phonon scattering in Landau-quantized graphene. *Phys. Status Solidi B*, 251:2541–2544, 2014.

BIBLIOGRAPHY

- [96] F. Wendler and E. Malic. Population inversion in Landau-quantized graphene. [arXiv:1410.2080](https://arxiv.org/abs/1410.2080), 2014.
- [97] Florian Wendler, Andreas Knorr, and Ermin Malic. Carrier multiplication in graphene under Landau quantization. *Nature Commun.*, 5:3703, 2014.
- [98] Torben Winzer, Andreas Knorr, and Ermin Malić. Carrier multiplication in graphene. *Nano Lett.*, 10(12):4839, 2010.
- [99] Torben Winzer and Ermin Malić. Impact of auger processes on carrier dynamics in graphene. *Phys. Rev. B*, 85:241404(R), 2012.
- [100] Torben Winzer, Ermin Malić, and Andreas Knorr. Microscopic mechanism for transient population inversion and optical gain in graphene. *Phys. Rev. B*, 87:165413, Apr 2013.
- [101] Di Xiao, Gui-Bin Liu, Wanxiang Feng, Xiaodong Xu, and Wang Yao. Coupled spin and valley physics in monolayers of mos_2 and other group-vi dichalcogenides. *Phys. Rev. Lett.*, 108:196802, May 2012.
- [102] Yuxi Xu, Hua Bai, Gewu Lu, Chun Li, and Gaoquan Shi. Flexible graphene films via the filtration of water-soluble noncovalent functionalized graphene sheets. *Journal of the American Chemical Society*, 130(18):5856–5857, 2008.
- [103] Li Yang, Jack Deslippe, Cheol-Hwan Park, Marvin L. Cohen, and Steven G. Louie. Excitonic effects on the optical response of graphene and bilayer graphene. *Phys. Rev. Lett.*, 103(18):186802, 2009.
- [104] Ferdows Zahid, Lei Liu, Yu Zhu, Jian Wang, and Hong Guo. A generic tight-binding model for monolayer, bilayer and bulk mos_2 . *AIP Advances*, 3(5):–, 2013.
- [105] Yanyuan Zhao, Xin Luo, Hai Li, Jun Zhang, Paulo T. Araujo, Chee Kwan Gan, Jumiati Wu, Hua Zhang, Su Ying Quek, Mildred S. Dresselhaus, and Qihua Xiong. Interlayer breathing and shear modes in few-trilayer mos_2 and wse_2 . *Nano Lett.*, 13(3):1007–1015, 2013.
- [106] Huaixiu Zheng, Z. F. Wang, Tao Luo, Q. W. Shi, and Jie Chen. Analytical study of electronic structure in armchair graphene nanoribbons. *Phys. Rev. B*, 75:165414, Apr 2007.

BIBLIOGRAPHY

- [107] Xinjian Zhou, Thomas Zifer, Bryan M. Wong, Karen L. Krafcik, Francois Leonard, and Andrew L. Vance. Color detection using chromophore-nanotube hybrid devices. Nano Lett., 9(3):1028, 2009.